Surface Accuracy and Pointing Error Prediction of a 32 m Diameter Class Radio Astronomy Telescope

by

Severin Azankpo

Thesis presented in partial fulfilment of the requirements for the degree of Master of Engineering (Mechanical) in the Faculty of Engineering at Stellenbosch University

Supervisor: Prof. Gerhard Venter

March 2017

Declaration

By submitting this thesis electronically, I declare that the entirety of the work contained therein is my own, original work, that I am the sole author thereof (save to the extent explicitly otherwise stated), that reproduction and publication thereof by Stellenbosch University will not infringe any third party rights and that I have not previously in its entirety or in part submitted it for obtaining any qualification.

Date: March 2017

Abstract

Surface Accuracy and Pointing Error Prediction of a 32 m Diameter Class Radio Astronomy Telescope

S. Azankpo

Department of Mechanical and Mechatronics Engineering,
University of Stellenbosch,
Private Bag X1, Matieland 7602, South Africa.

Thesis: MEng (Mech)

March 2017

The African Very-long-baseline interferometry Network (AVN) is a joint project between South Africa and eight partner African countries aimed at establishing a VLBI (Very-Long-Baseline Interferometry) capable network of radio telescopes across the African continent. An existing structure that is earmarked for this project, is a 32 m diameter antenna located in Ghana that has become obsolete due to advances in telecommunication. The first phase of the conversion of this Ghana antenna into a radio astronomy telescope is to upgrade the antenna to observe at 5 GHz to 6.7 GHz frequency and then later to 18 GHz within a required performing tolerance. The surface and pointing accuracies for a radio telescope are much more stringent than that of a telecommunication antenna. The mechanical pointing accuracy of such telescopes is influenced by factors such as mechanical alignment, structural deformation, and servo drive train errors. The current research investigates the numerical simulation of the surface and pointing accuracies of the Ghana 32 m diameter radio astronomy telescope due to its structural deformation mainly influenced by gravity, wind and thermal loads.

Uittreksel

Oppervlak Akkuraatheid en Wysings-fout Voorspelling van 'n 32 m Diameter Klas Radio-Astronomie Teleskoop

("Surface Accuracy and Pointing Error Prediction of a 32 m Diameter Class Radio Astronomy Telescope")

S. Azankpo

Departement Meganiese en Megatroniese Ingenieurswese,
Universiteit van Stellenbosch,
Privaatsak X1, Matieland 7602, Suid Afrika.

Tesis: MIng (Meg)

Maart 2017

Die Afrika Baie-lang-basislyn interferometrie Netwerk (ABN) is 'n gesamentlike projek tussen Suid Afrika en agt ander Afrika lande. Die doel van die projek is om 'n netwerk van radio teleskope oor die Afrika kontinent te plaas wat gesamentlik oor VLBI vermoëns beskik. 'n Bestaande 32 m antenna in Ghana, wat nie meer gebruik word nie as gevolg van nuwe ontwikkelinge in telekommunikasie, is onder andere geïdentifiseer vir die projek. Die antenna sal na 'n radio teleskoop omgeskakel word waarvan die eerste fase opgraderings van die bestaande antenna is. Hierdie opgraderings sal die teleskoop in staat stel om waarnemings, binne toelaatbare toleransies, by 5 GHz en 6.7 GHz en later 18 GHz, te kan maak. Die toelaatbare oppervlak- en wysings-foute van 'n radio teleskoop is baie strenger as die van 'n telekommunikasie antenna. Die meganiese wysings-fout van sulke teleskope word beïnvloed deur faktore soos meganiese belyning, strukturele vervorming en foute in die aandryfstelsel. Die navorsing in hierdie tesis ondersoek die numeriese simulasie van die oppervlak en wysings-foute van die Ghana 32 m diameter radio teleskoop as gevolg van die strukturele vervorming soos beïnvloed deur gravitasie, wind en termiese vragte.

Acknowledgements

My foremost thanks go to the almighty God for His sufficient grace and successfully seeing me through this journey. I owe a special depth of gratitude to my supervisor, Prof. Gerhard Venter for his advice, guidance and patience throughout my entire studies. I am truly grateful and privileged to work under your supervision. I also would like to express my deepest thanks and sincere appreciation to Mr Japie Ludick, the team leader for the Structural Mechanical Work Group of the AVN for suggesting the topic and making this study possible through his unwavering support and mentorship. I appreciate your help, Mr William Walbrugh and thank you for putting smiles on our faces from your corner office. Thank you, Mrs. Kathryn Rosie for your assistance and attention to detail. To all my colleagues from the SKA-SA office, Stellenbosch campus and all my friends, I am very grateful to you for making my stay very enjoyable. Special thanks go to my sponsors, SKA-SA; without your help this research would have not been possible and also to GAEC for giving me the opportunity to embark on this study. Thank you, Mr Francis Oppong, for hosting me and keeping me company whenever I visit campus. My final thanks go to my beloved family for their support and encouragement in keeping me going.

Dedications

This thesis is dedicated to my mother, Mrs Comfort Azankpo and to all loved ones for your warmest affection and committed support for making this journey an amazing drive.

Contents

List of Figures

List of Tables

Nomenclature

Constants

g	=	9.81 m/s^2
ν	=	3.0×10^8 m/s
π	=	3.141592653590

Variables

A	Area	[m^2]
C	Cosine angle	[ ]
C_d	Drag coefficient	[ ]
C_j	Zernike coefficient	[ ]
d	depth	[m]
D	Diameter	[m]
E	Least square fit error	[ ]
f	Frequency	[Hz]
F	Force or Load	[N]
f_l	Focal length	[m]
$\mathrm{ff_d}$	Fitted paraboloid nodal focal distance	[m]
$HPBW$	Half-Power Beam Width	[rad]
HT	Homogeneous transformation matrix	[ ]
N	Number of grid nodes	[ ]
P	Pressure	[Pa]
q	Dynamic pressure	[Pa]
R	Rotation transformation matrix	[ ]
S	Sine angle	[ ]
T	Translation vector	[m]
$\mathrm{uf_d}$	Undeformed nodal focal distance	[m]
U	Nodal displacement	[m]
v	Velocity	[m/s^2]
W	Weighing factor	[m^2]

x, y, z	Coordinate values	[ ]
X, Y, Z	Coordinate axes	[ ]
Z_p	Zernike polynomial	[ ]
η_{sf}	Surface efficiency	[ ]
σ	Surface error	[m]
λ	Wavelength	[m]
ρ	Density	[kg/m^3]
ϕ	Zernike term	[ ]
φ	Yaw angle about Z-axis	[°]
θ	Pitch angle about Y-axis	[°]
ψ	Roll angle about X-axis	[°]
γ	Pointing or tracking error	[°]
γ_{rms}	Pointing accuracy	[°]

Superscripts

e	Element
i	Grid node
m	Number of Zernike terms
n	Number of grid nodes
T	Transpose

Subscripts

p	polynomial
pda	projected dish area
rms	root mean square
sw	static wind

Vectors and Tensors

$\overleftarrow{\text{fB}}$	Fitted Paraboloid Beam Axis Vector
$\overleftarrow{\text{uB}}$	Undeformed Beam Axis Vector

Acronyms

0D	Zero Dimensional
1D	One Dimensional
2D	Two Dimensional
AISI	American Iron and Steel Institute
ASCS	Antenna Steering Control System

ASTM	American Society for Testing and Materials
AT-LBA	Australia Telescope Long Baseline Array
AVN	African VLBI Network
BC	Boundary Conditions
BWG	Beam Waveguide
CAD	Computer-Aided Design
CHS	Circular Hollow Section
CMWG	Control and Monitoring Work Group
DOF	Degree of Freedom
DSIF	Deep Space Instrumentation Facility
DSN	Deep Space Network
EAVN	East-Asia VLBI Network
EVN	European VLBI Network
FAST	Five hundred meter Aperture Spherical Telescope
FE	Finite Element
GAEC	Ghana Atomic Energy Commission
GBT	Green Bank Telescope
GD SATCOM	General Dynamics Satellite Communication Systems
GSSTI	Ghana Space Science and Technology Institute
HartRAO	Hartebeeshoek Radio Astronomy Observatory
HPBW	Half-Power Beam Width
ICRF	International Celestial Reference Frame
ITRF	International Terrestrial Reference Frame
IVS	International VLBI Service for Geodesy and Astrometry
JPL	Jet Propulsion Laboratory
KAT	Karoo Array Telescope
MPC	Multi Point Constraints
MSC	MacNeal-Schwendler Corporation
NASA	National Aeronautics and Space Administration
NEC	Nippon Electric Company
PID	Proportional Integral Derivative
PMWG	Project Management Work Group
RBE2	Rigid Body Element(type=2)
RBM	Rigid Body Motion
RF	Radio Frequency
RMS	Root Mean Square

RSS	Root Sum Square
ROACH	Reconfigurable Open Architecture Computing Hardware
SCWG	Signal Chain Work Group
SHS	Square Hollow Section
SKA	Square Kilometre Array
SKA-SA	Square Kilometre Array South Africa
SPWG	Science Processing Work Group
SMWG	Structural Mechanical Work Group
SWWG	Software Work Group
TIW	Telesystem International Wireless System Inc.
US VLBA	America's Very Long Baseline Array
VLBI	Very Long Baseline Interferometry

Symbols

Al	Aluminium

Chapter 1

Introduction

The discovery of a redundant range of 25 m to 32 m diameter class satellite communications antennas by the former director of Hartebeesthoek Radio Astronomy Observatory (HartRAO), the late Dr Mike Gaylard, ignited interest from the radio astronomy fraternity. Most of these antennas were used in the Intelsat telecommunication project across the continent during the 1980s. Advances in the telecommunication industry rendered some of these telescopes unused as fibre optic communications proved faster and more reliable. The cost of converting these obsolete telecommunication structures into radio telescopes is less than half the cost of building new telescopes, attracting the interest of international stakeholders in radio astronomy to put them to good use.

This research presents the qualitative means of capturing the mechanical pointing performance of such radio astronomy telescopes. The allowable surface error tolerances for a radio telescope are much more stringent than those of a telecommunication antenna. The conversion thus requires the radio astronomy telescope to fall within some required performance tolerances. In this chapter, the research problem is presented and the objective for the study defined.

1.1 Background

The inception of Very Long Baseline Interferometry (VLBI) since the 1960s plays an important role in the establishment of the International Celestial Reference Frame (ICRF), the International Terrestrial Reference Frame (ITRF), as well as many useful insights into space exploration, astrometric and geodetic research such as predicting the orientation and rotation of the Earth and direct observation of nutation parameters and of the time difference UT1-UTC [see 1, 2]. VLBI is a technique whereby telescopes with a large distance between them are used to observe the same source, providing a much better resolution than a single dish observation. The 26 m and 15 m diameter radio telescopes located at HartRAO, in the province of Gauteng, South Africa are currently

the only radio telescopes from the African continent participating in the International VLBI Service (IVS) activities [3].

One of the mandates of the Square Kilometre Array (SKA)-Africa is to identify and convert a selected number of unused telecommunication satellite tracking dishes across the African continent into radio telescopes as well as to build new ones. These activities aim at forming an African VLBI Network (AVN) to enhance human capacity development and also partake in global VLBI experiments. Selected countries like Ghana, Mozambique, Kenya, Zambia, Namibia, Madagascar, Botswana, and Mauritius joined South Africa in the bid to establish the AVN and also to contribute to this transformational science research across the globe [4, 5].

Ghana's 32 m diameter satellite earth station with position coordinates of $05°45'01.5''N$ and $00°18'18.4''W$ situated at Kuntunse, in the Greater Accra region, is earmarked for this project [6]. The conversion from a satellite tracking station to a radio telescope requires high precision pointing at astronomical sources by scientists as they explore the universe. Figure 1.1 shows the Ghana 32 m diameter antenna, located 4,637 km from the South Africa HartRAO 26 m diameter radio telescope.

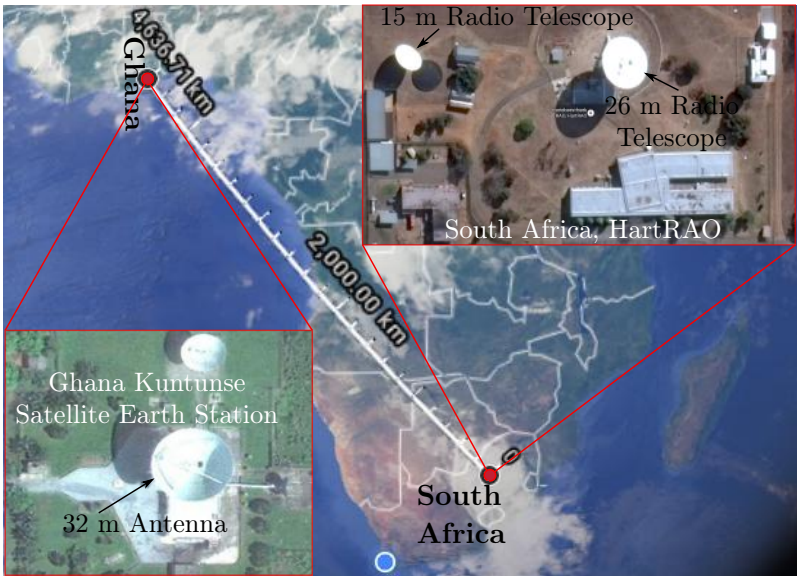

Figure 1.1: Ghana Antenna Earth Station and South Africa HartRAO [Google Maps]

Generally, the mechanical[1] pointing accuracy of such radio telescopes is influ-

[1]Other factors, which are not directly related to structural deflection, exist such as atmospheric radio frequency (RF) refraction and control system errors affecting the pointing accuracy but not contributed directly to the telescope structure.

enced by several factors that can be classified as mechanical alignment, structural deformation, and servo drive train errors. The requirement for pointing accuracy is less than 10% of the antenna's half-power beam width (HPBW). For the Ghana antenna, the beam width at 6.7 GHz is 0.096°, therefore the pointing accuracy requirement is 9.6 millidegrees (35")[see section 2.5.1].

A key factor related to the pointing accuracy is the surface accuracy of the reflector system. This is mainly influenced by gravity, the wind, and thermal loading during operation of the telescope. The distortion of the surface due to these effects results in a transposed pointing vector which directly impacts pointing accuracy. These natural influences that induce pointing errors are often extremely difficult to eliminate, particularly gravity which is impossible to avoid. However, it is possible to forecast and numerically quantify these pointing errors to be factored into a pointing error model usually used by the radio telescope's proportional integral derivative (PID) controller feedback loop to provide corrections between the telescope's commanded and actual position.

A preliminary pointing error budget allocation for the Ghana 32 m telescope at the structure level exist at the SKA-SA [7] based on similarity and calculated values as shown in table 1.1. The error budget captures the pointing error under two main categories, namely correlated and random errors.

Table 1.1: The Ghana 32 m Antenna Structure Pointing Error Budget [7]

Error Definition	**S**	**C**	**[arcsec]**	**Elevation Error [°]**		**Cross-Elevation Error [°]**	
Correlated Errors			**W/O**	**W/O**	**W**	**W/O**	**W**
RF Axis Collimation	RSS	C	5	0.0014	0.0001	0.0014	0.0001
Orthogonality Reflector/Elevation Axis	RSS	C	5			0.0014	0.0001
Orthogonality Elevation/Azimuth Axis	RSS	C	10			0.0028	0.0003
Orthogonality Azimuth/Track Plane	RSS	C	7	0.0019	0.0002	0.0019	0.0002
Gravity (60° Elevation Angle)	RSS	C	13	0.0037	0.0004	0.0037	0.0004
Thermal (8 K Gradient)	RSS	C	5	0.0014		0.0014	
Sum of Correlated Errors				0.0046	0.0004	0.0056	0.0005
Total Correlated Pointing Error/Axis	Total (W/O)			0.0072			
	Total (W)			0.0007			
Random Errors			**W/O**	**W/O**	**W**	**W/O**	**W**
Drive Train Backlash	RMS	C	30	0.0083		0.0083	
Encoder Shaft Deflection	RMS		1.3	0.0004	0.0004	0.0004	0.0004
Encoder Accuracy	RMS		10	0.0028	0.0028	0.0028	0.0028
Control Loop	RMS		5	0.0014	0.0014	0.0014	0.0014
				0.0045	0.0016	0.0045	0.0016
Wind (at site median 19.5 km/h)	A		1.8	0.0005	0.0005	0.0005	0.0005
Sum of Random Errors				0.0050	0.0021	0.0050	0.0021
Total Random Pointing Error/Axis	Total (W/O)			0.0070			
	Total (W)			0.0029			
Total Error (W/O)			51	0.0142			
Total Error (W)			13	0.0036			

C = Compensation
S = Summation Method (RMS =Root Mean Square, RSS =Root Sum Square, A =Algebraically Added)
W/O = Without Compensation
W = With Compensation

The correlated errors such as the RF axis collimation, non-orthogonality of the reflector (or beam) axis to the elevation axis, orthogonality of the elevation and azimuth axes, unevenness of the azimuth track, and gravity, and thermal load deformations are repetitive and easily quantifiable. The correlated errors are typically expressed as a function of the elevation and azimuth angle of the radio telescope to provide error compensation for the antenna steering control system. The cross-elevation error is defined as the azimuth angle error times the cosine of the elevation angle [7]. The correlated errors are summed using root-sum-square (RSS) summation.

The random errors are stochastic in nature and can only be predicted over a certain range of values without any meaningful correlation to elevation and azimuth angles. Examples include the encoder accuracy, encoder shaft deflection, drive train backlash, control system errors, and wind gusts. The correlated errors are summed using root-mean-square (RMS) summation.

This thesis seeks to investigate the research questions:

1. Can the numerically quantified distortions of the antenna structure due to gravity be used to minimise the pointing error contribution of gravity loading over the entire elevation operational range of the telescope?
2. Can the combination of numerically quantified distortions of the antenna structure due to gravity, wind, thermal loading and initial assembly tolerances be used to validate the apportionment of pointing error budget to the antenna structure in the system's engineering process employed during the conversion of a telecommunication antenna to radio telescope?
3. Can the error contribution due to the combined effects be further significantly reduced by means of economically viable and practical selective addition of structural stiffening members addressing specific distortion modes of the structure?

To probe this, the Ghana 32 m satellite antenna is chosen for this study for two reasons, (a) it is the first and current antenna under the AVN radio telescope conversion project and, (b) the author has access to the manufacturing drawing data pack and other documentation relating to the Ghana 32 m antenna.

The strategy to be followed is to capture the Ghana 32 m telescope's structural deformations by creating a finite element (FE) model. The FE model's output deformation fields include the dish rigid body motion. An external program is developed to eliminate the rigid body motion and then best fit a paraboloid through the resulting deformed data to compute the root-mean-square (RMS) surface and pointing errors. These errors are not directly captured by the FE simulation software package and are thus calculated as a post-processing step. Furthermore, this study explores and proposes ways of reducing the primary (or main) reflector's surface deformations of the Ghana 32 m radio astronomy telescope.

1.2 Research Objectives

The primary objectives of the research are:

(i) To produce an accurate FE model of the Ghana 32 m telescope using the original drawings and engineering data. The FE model's accuracy will be determined by how close it correlates with results from published data and dish surface measurements.

(ii) To analyse the structural deformation due to the effects of gravity, the wind and thermal loading of the Ghana 32 m radio telescope under different operating load cases.

(iii) To quantify the surface accuracy and the pointing errors of the Ghana 32 m radio telescope by means of analytical/numerical techniques.

The secondary objectives of this research are to (a) generate a computer-aided design(CAD) model of the Ghana 32 m telescope from the drafted manufacturing data pack to ascertain the mass balance around the elevation axis, and (b) suggest practical ways of improving the pointing accuracy.

1.2.1 Scope of Work

The scope of work for this study includes;

(i) A literature survey of available techniques and validation tests to detect the 32 m radio telescope's primary reflector deformations.

(ii) Create a CAD Model of the Ghana 32 m telescope structure from the existing drafted manufacturing drawing data pack.

(iii) Develop an FE model of the 32 m radio telescope with key structural members contributing to the overall stiffness.

(iv) Record the deformation of the telescope dish through a range of elevation and azimuth angles under gravity, the wind, and thermal loadings.

(v) Perform a numerical test simulation to compute the radio telescope's surface and pointing errors by using a best fit least squares method to fit a paraboloid surface to the deformed nodal data obtained from the FE model.

(vi) Propose practical modifications for reducing the dish surface deformation.

1.2.2 Exclusions/Limitations

The following are excluded from this research;

(i) The research does not account for the contribution of damaged and corroded structural members on the Ghana 32 m telescope. This is not the main focus for the study.

(ii) The displacements of the dish surface nodes tangent to the parabolic surface will not affect the RMS surface and pointing error and therefore are excluded from the pointing error calculation.

1.2.3 Assumptions

To simplify the boundary conditions in the FE model, the following assumptions were made;

(i) The deformation of the concrete structure upon which the telescope is mounted is approximated as a rigid body.

(ii) The azimuth track of the Ghana 32 m telescope is assumed flat and rigid.

1.3 Significance of the Research

Structural deformation of radio telescopes greatly influences their pointing performance as scientists steer them across the sky. A good repeatable pointing model prediction is therefore critical to their operation in acquiring more accurate data from cosmic sources.

This research uses numerical simulations by exploiting strategies of applying different operational load cases that capture the pointing errors. Once validated, this can serve as a working model which can be replicated for similar defunct antennas across the continent for the AVN project.

Furthermore, the FE model may be used to predict the tracking performance and to optimise the structure for decreasing the overall dish surface deformation by strategically placed stiffening members in the backing structure as well as the counter weight attachment structure

1.4 Definitions of Key Terminology

Surface Accuracy is described as the error related to the difference between a nominal paraboloid surface describing the antenna dish and the best fit dish surface.

Pointing Error is the space angle between the commanded vector and the beam vector of the antenna [7].

Paraboloid is a surface generated by rotating a parabola about its axis of symmetry.

Numerical Simulation is the use of numerical methods to solve a problem.

Pointing Model is a mathematical model including terms which accounts for errors in radio telescopes when pointing or tracking sources.

Structural Deformation is the term used to describe the distortion, warping, bending, and twisting in structures usually influenced by combined factors such as gravity, the wind, thermal or external loads.

Operational Load Cases describe the prevailing environmental conditions and the telescope's movement during operation, which influence its structural deformation.

Zenith is the pointing direction of the radio telescope's focal axis directly above it at 90° elevation angle to the horizon.

1.5 Brief Chapter Overview

Chapter 2 presents a literature survey on other similar converted radio astronomy telescopes as well as newly built ones. The Ghana 32 m radio telescope as part of the AVN project driven agenda is covered. The FE analysis of the Ghana 32 m telescope is detailed in chapter 3, while the algorithm developed to compute the surface accuracy and the pointing error are discussed in chapter 4. Chapters 3 and 4 describe the research design and methodology employed. Chapter 5 presents a means of validating the numerical results presented in the research design and methodology. Chapter 6 suggests possible areas of the telescope that may be optimized to reduce dish surface deformation. Finally, the research is concluded in Chapter 7, where findings are discussed, and recommendations and possible future research areas, are identified.

Chapter 2

Literature Survey

Typically, radio astronomy telescopes operate in one of the two modes; single dish science observations (such as pulsar observations, maser studies, spectroscopy, and radiometry), and VLBI network observations. The VLBI science requires a collaboration between at least four radio astronomy telescopes from different geographical locations viewing celestial source(s) within the same time frame. The VLBI theory is well developed within the radio astronomy science community. The individual telescope's output data is correlated to form a clearer image of the source. The type of telescopes selected for a VLBI observation depends on their observing frequency. The observing frequency places a lower accuracy limit on the telescope's surface roughness and pointing deviation, and the telescopes are therefore required to perform within some accuracy margin.

This chapter describes the various types of radio astronomy telescopes with particular attention to the class of the Ghana 32 m radio telescope. The evolution of the Ghana 32 m radio telescope as part of the AVN, and ultimately the SKA project is presented with its current conversion activities. Finally, similar converted antennas as well as newly built telescopes such as the Medicina Telescope, the Karoo Array Telescope (KAT), MeerKAT, and the Green Bank Telescope (GBT) are reviewed, and their surface and pointing error summarised.

2.1 Types of Radio Astronomy Telescopes

Radio astronomy telescopes are available in various configurations, and can be broadly classified based on: (a) how they focus radio waves, (b) the type of mount, (c) the primary reflector type, (d) the secondary reflector (or sub-reflector) type, (e) whether the secondary reflector is fixed or moving, (f) whether single or in arrays, and (g) dish size and observing frequencies.

The radio telescopes with a prime focus have their receiver feed mounted at the focus of the primary reflector, while the Cassegrain focus refocuses the radio waves from a secondary reflector after bouncing off from the primary reflector as illustrated in figure 2.1.

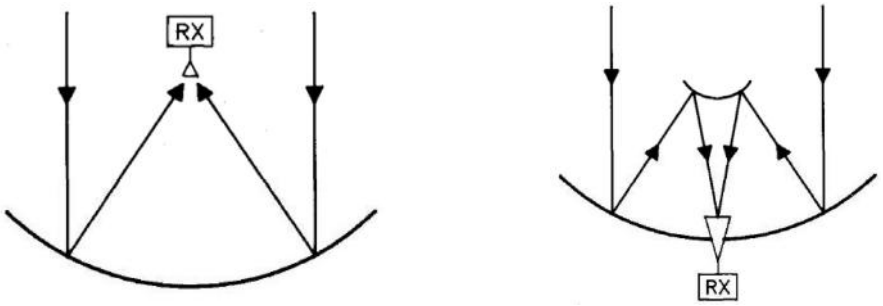

(a) Prime Focus (b) Cassegrain Focus

Figure 2.1: Prime and Cassegrain Focus Radio Telescopes [8]

There are other special types of Cassegrain focus or non-prime focus radio telescopes such as the Offset Cassegrain focus, Dual offset focus, Nasmyth focus, and Beam Waveguide as shown in figure 2.2.

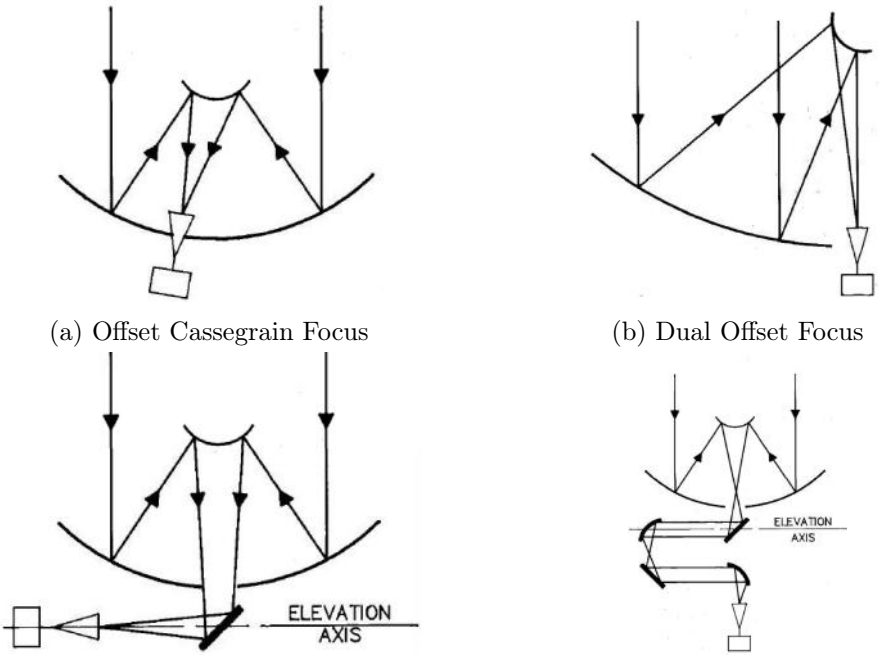

(a) Offset Cassegrain Focus (b) Dual Offset Focus

(c) Naysmith Focus (d) Beam Waveguide

Figure 2.2: Non-Prime Focus Radio Telescopes [8]

Radio telescopes can either be mounted to rotate about one axis, in which case they are called equatorial or polar mount radio telescopes, or to rotate about

two axes, which are called altitude-azimuth or elevation-azimuth mount radio telescopes. Figure 2.3 shows the two main types of mounting designs for radio telescopes.

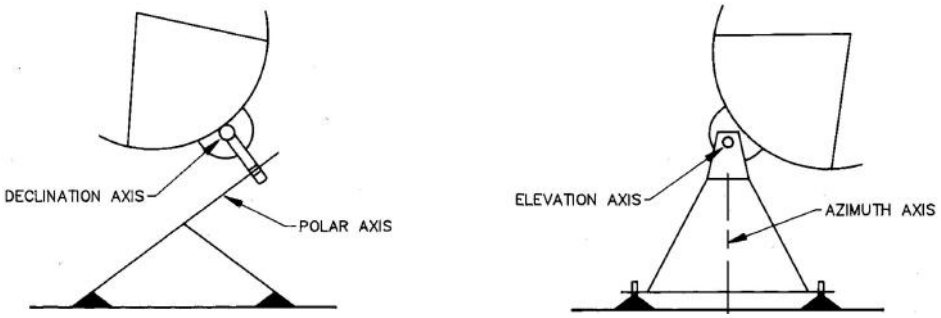

(a) Equitorial Mount Telescope (b) Altitude-Azimuth Mount Telescope

Figure 2.3: Telescope Mount Types [8]

The elevation-azimuth telescopes often have symmetric designs which make them less costly, and are often used for large heavy telescopes. The polar mount permits tracking sources in diurnal motion about an axis parallel to the rotation axis of the Earth and often needs heavy counterweights. The polar mount is suitable for lighter telescopes and for radio source tracking. The elevation-azimuth telescope designs can be wheel and track or yoke and tower design. The yoke and tower design is ideal for keeping the perpendicularity between the azimuth and the elevation axis, as is critical for VLBI experiments, but cost and mechanical limitations make the wheel and track design more preferable for very large radio telescopes.

The paraboloidal primary reflector telescope designs are the most commonly used telescope in radio astronomy across the globe. Only a few radio telescopes use the spherical primary reflectors such as the 305 m Arecibo radio telescope in Puerto Rico, and the 500 m aperture spherical telescope (FAST) in China which are the second largest and largest single-dish filled-aperture radio telescopes respectively. Only a fraction of their total collecting area is used at a time in tracking sources. The RATAN-600 telescope in Russia uses a cylindrical paraboloid design for its primary reflector.

Classification based on secondary reflectors are either hyperboloidal convex surfaces, as commonly used in Cassegrain telescope designs, or ellipsoidal concave surfaces as in Gregorian telescope designs. Also, the secondary reflectors can be configured to be either fixed or movable with a sliding mechanism to control its focal position.

In application, radio telescopes can be used in single-dish observations or in collaboration with other telescopes in an array such as in VLBI. They can also be classified based on the dish size, or the observing source/frequency.

2.2 Reflector Geometry

The application of parabolic reflectors in radio astronomy telescope design is popular because of their reflective properties. In principle, rays that enter a parabola travelling parallel to its axis of symmetry are reflected to its focus, regardless of the position on the parabola at which the incidence occurs. Conversely, rays that originate from a point source at the focus are reflected (collimated) into a parallel beam, exiting the parabola parallel to the axis of symmetry. The reflection angles of the rays are equal to the incidence angles at the points of incidence on the parabolic dish.

Figure 2.4 shows a sketch of a vertical plane section through a Cassegrain focus reflector system with a paraboloid primary reflector and hyperboloid secondary reflector.

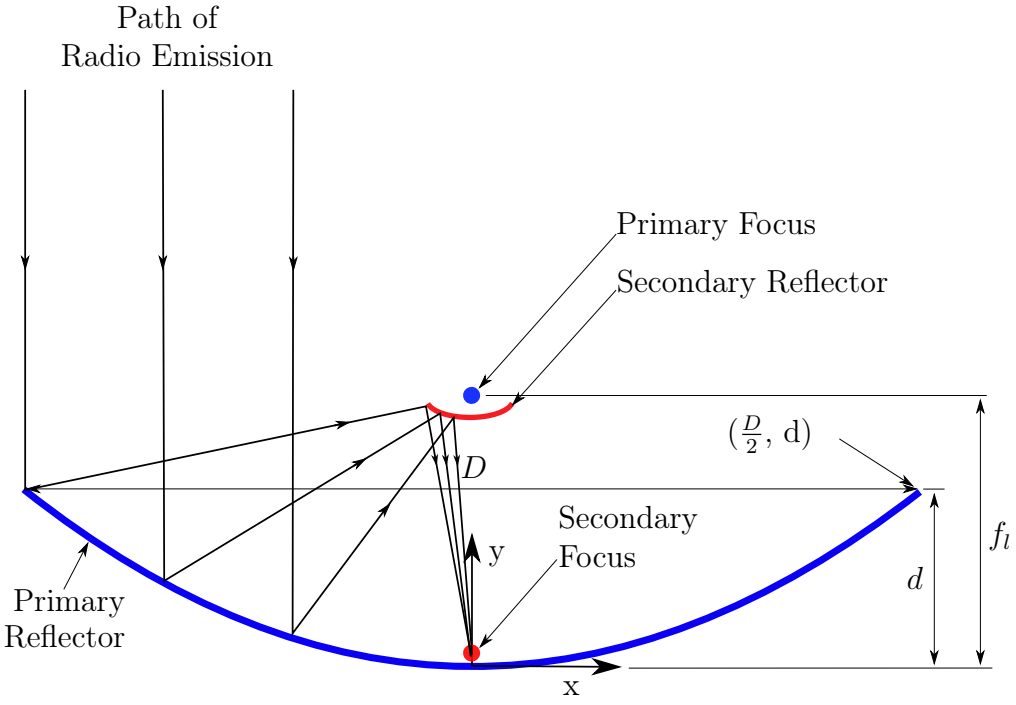

Figure 2.4: Dish Section

The parabolic equation of the primary reflector curve can be written as equation 2.2.1.

$$y = ax^2 \tag{2.2.1}$$

where $a = \frac{1}{4f_l}$, and substituting a point$(\frac{D}{2}, d)$ on the curve into equation 2.2.1, the focal length, f_l can be expressed as equation 2.2.2.

$$f_l = \frac{D^2}{16d} \tag{2.2.2}$$

where D and d are the dish diameter and depth respectively.

This provides an estimate of the focal length for the Ghana 32 m dish not explicitly documented but useful in the primary reflector's surface error calculations. Figure 2.5 shows the theoretical panel data points defining the paraboloid surface equation of the Ghana 32 m diameter dish.

The focal length computed from the given data points using equation 2.2.2 with $D = 32.02676$ m and $d = 6.22671$ m is $f_l = 10.29549$ m . However, the resulting equation ($y = 0.02428\ x^2$) does not perfectly fit the remaining data points. A second order polynomial which fitted through the nodal data points as shown in figure 2.6 provided a slightly improved fit. An optimized parabola fitted through the data points using a least squares process yielded the most accurate parabolic equation as shown in equation 2.2.3.

$$y = 0.0243805223\ x^2 \tag{2.2.3}$$

In a similar approach to deriving equation 2.2.3 in three dimensions, a more generic equation for the paraboloid surface with vertex point (0, 0, 0) and a focal point on the Z-axis can be reproduced as equation 2.2.4.

$$z = \frac{x^2 + y^2}{4f_l} \tag{2.2.4}$$

where the focal length, $f_l = 10.254$ m for the Ghana 32 m diameter radio telescope's dish.

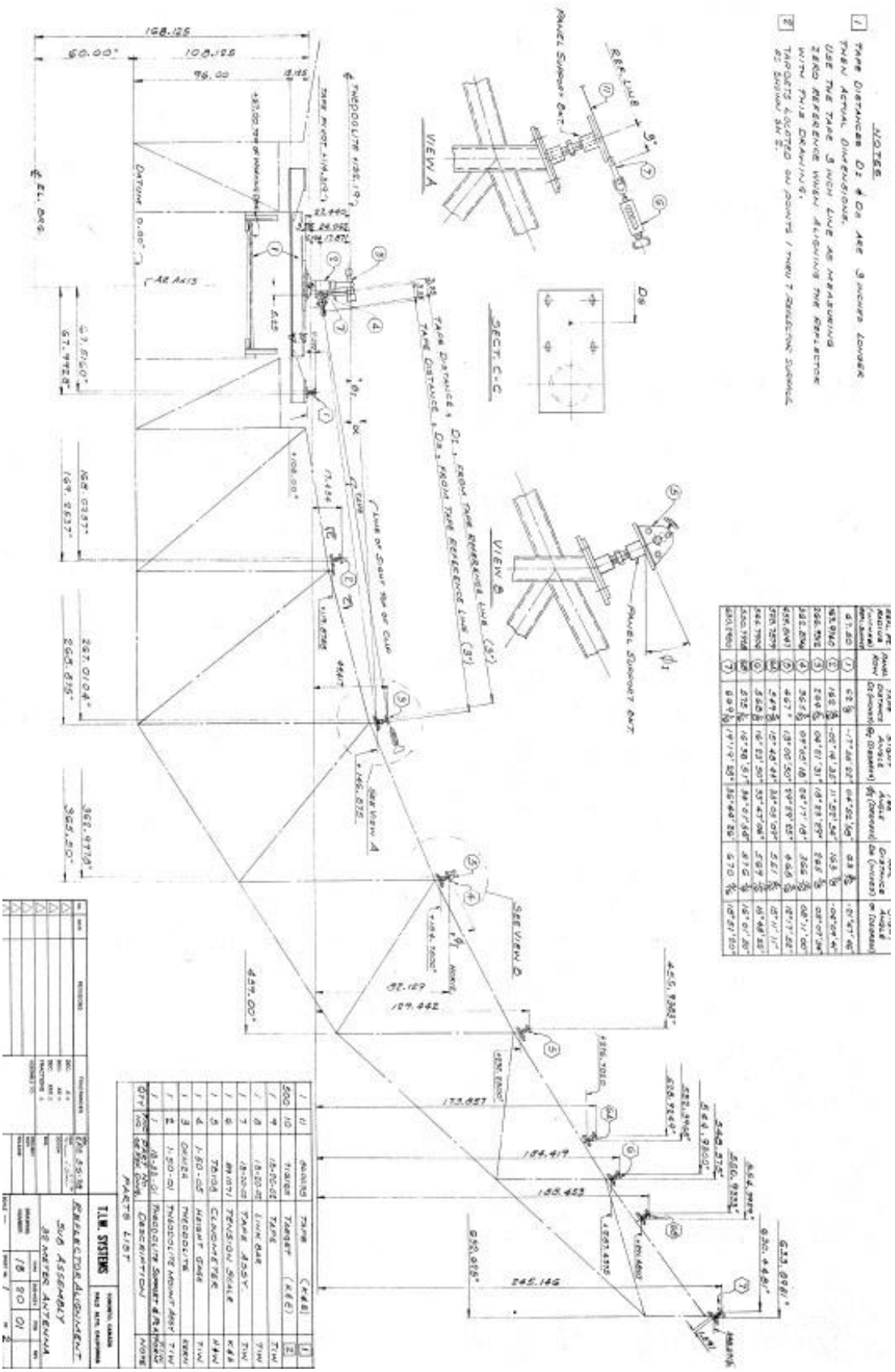

Figure 2.5: Radial Truss with Theoretical Dish Surface Nodes [9]

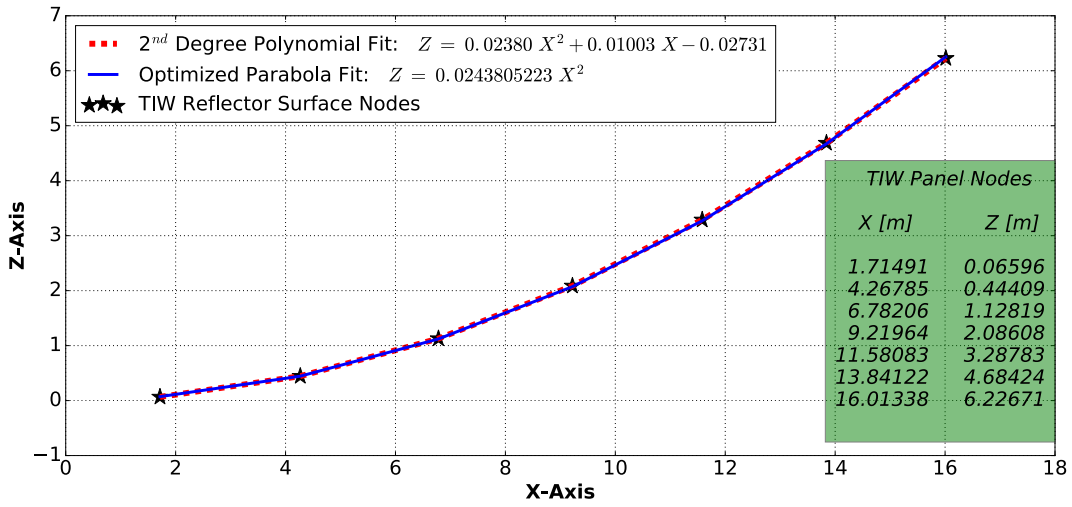

Figure 2.6: Parabolic Reflector Equation

2.3 The SKA Project

The SKA project is an international effort to set up the world's most sensitive and largest arrays of radio telescopes, with the goal of probing the universe in greater detail than ever before. VLBI capable network groups such as, (a) European VLBI Network (EVN), (b) America's Very Long Baseline Array (US VLBA), (c) East-Asia VLBI Network (EAVN), and (d) Australia Telescope Long Baseline Array (AT-LBA) are spread across the globe and are working together in advancing the agenda of the SKA. Figure 2.7 shows these organizations with a gap created between Europe and Southern Africa. The African VLBI Network (AVN) was therefore proposed to fill the existing gap, which will improve the output quality of astronomical observations.

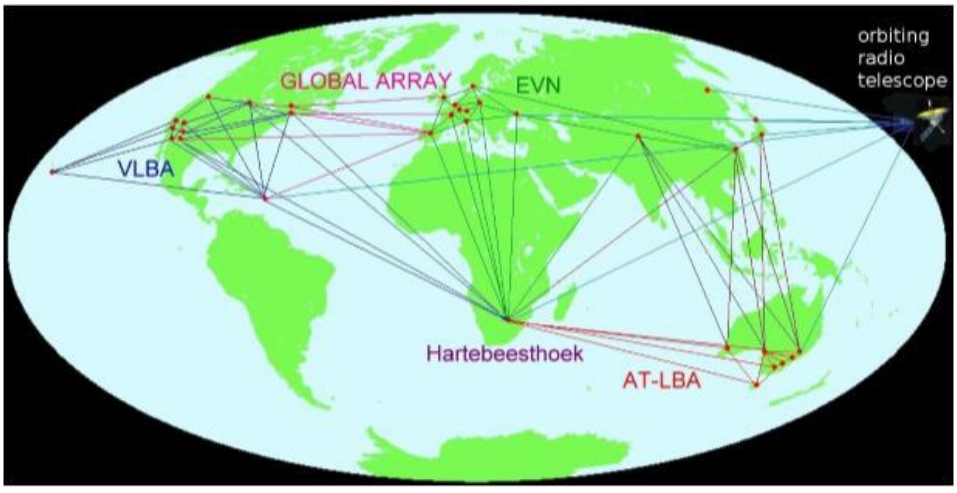

Figure 2.7: Global VLBI Networks
(Image: `http://www.hartrao.ac.za/summary/sumeng.html` - accessed on 30/04/2016)

A joint research collaboration between the EVN and US VLBA forms the Global Array network.

2.4 The AVN Project

The AVN became operational in 2011 with the immediate goal of building the capacity of radio astronomers and engineers across the African countries in preparation towards the SKA project. The 26 m and 15 m radio telescopes at HartRAO, South Africa (SA) are presently the only participating VLBI capable outstation in Africa. SKA-SA plays a pivotal role in establishing this transformational mega-science project across the African continent.

Several VLBI-capable outstations on the continent of Africa were identified. Most of these outstations possess defunct satellite earth station antennas rolled-out between the mid 60s and early 80s by Intelsat. These served as telecommunication antennas across the continent until the implementation of more efficient fibre optic communication.

Currently, the AVN project targets to convert four 32 m class antennas in Ghana, Kenya, Zambia and Madagascar into radio astronomy telescopes, and to build four new telescopes in four other partner African countries (Botswana, Mauritius, Namibia and Mozambique). Figure 2.8 shows a map of the selected satellite dishes to be converted as well as newly built telescopes participating in the AVN project.

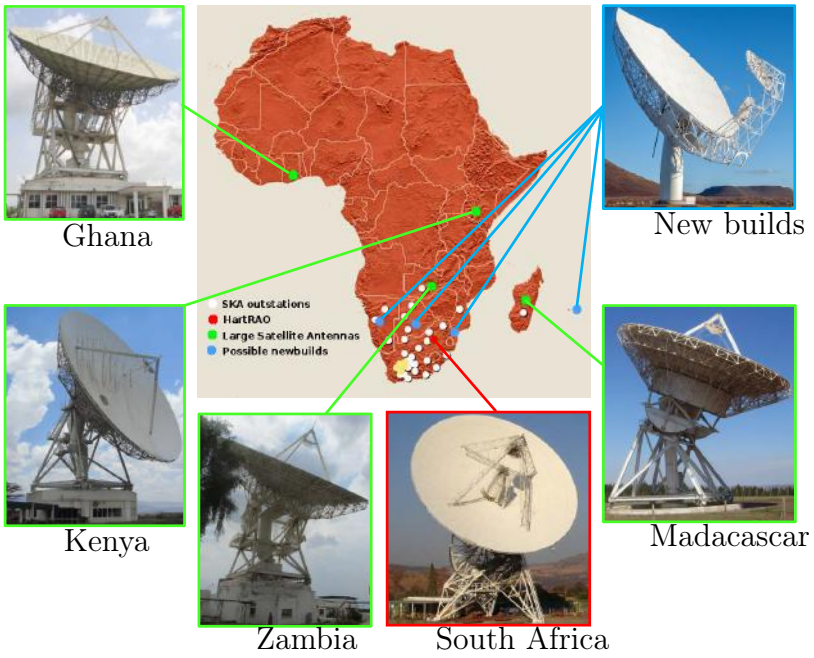

Figure 2.8: Satellite Dishes across AVN Partner Countries [10]

2.5 The Ghana 32 m Antenna

The Ghana 32 m antenna earth station was initially built and used as a telecommunication dish by microwave links through geostationary satellites. The earth station was owned by Vodafone Ghana Limited, a Ghanaian telecommunication company. The African undersea cable project, an efficient wideband communication system employing fibre optics, rendered this outstation inefficient and inoperative as an instrument for telecommunication. In 2011, the SKA-SA conducted an initial feasibility check and structural audit to evaluate the health of the antenna for conversion into a radio astronomy telescope. A memorandum of understanding signed in 2012 released the 32 m dish from Vodafone Ghana Limited to the government of Ghana, who in turn made it available for participation in the AVN project.

One of the main advantages in using Ghana as a VLBI outstation is its strategic position in the equatorial region of Africa. Most outstations in this region (especially West and Central African countries) have the advantage of a broader sky view which encompasses the entire plane of the Milky Way Galaxy.

The Ghana Space Science and Technology Institute (GSSTI) under the auspices of the Ghana Atomic Energy Commission (GAEC) was given oversight responsibility for the radio astronomy observatory, designated by the Ghana government. SKA-SA engineers and scientists, playing a leading role in the AVN project, are working closely with their counterparts in Ghana to convert the antenna into a radio astronomy telescope.

Figure 2.9 shows the Ghana 32 m antenna under conversion. The first plan for the conversion is to upgrade the mechanical and control systems with the existing feed fitted with 6.7 GHz receivers for initial single dish and VLBI observations. The converted telescope will be required to operate up to an observing frequency of 18 GHz [11]. The conversion activities are discussed in section 2.5.2.

The antenna weighs about 240 tonnes, consisting mainly of steel and aluminium, and is mounted on top of a building that houses the control systems and processing units. The dish is steerable about both the azimuth and the elevation axes. It is a dual focus antenna, with a Cassegrain primary paraboloid reflector, a fixed secondary hyperboloid reflector, and a beam waveguide (BMG).

Figure 2.9: The Ghana 32 m Antenna (Image courtesy SKA-SA)

2.5.1 Surface and Pointing Accuracy Requirements

One of the factors which affects the station's ability to meet AVN user requirements is the surface accuracy and pointing accuracy achievable by the antenna.

Ruze [12] provided the Ruze formula shown in equation 2.5.1 which provides an elegant way of calculating the surface efficiency, η_{sf} of a paraboloid reflector.

$$\eta_{sf} = e^{-(\frac{4\pi\sigma_{rms}}{\lambda})^2} \tag{2.5.1}$$

Where σ_{rms} is the rms surface error of the telescope's reflector surface, λ is the

observing wavelength and can also be expressed as

$$\lambda = \frac{\nu}{f}$$

where ν and f are the speed of light in air and operating frequency respectively.

A typical operating surface efficiency for a 32 m class radio telescope ranges between 50% and 70%. Assuming a minimum surface efficiency of $\eta_{sf} = 50\%$, and re-arranging the Ruze formula,

$$\sigma_{rms} = \frac{\lambda}{4\pi}\sqrt{-\ln(\eta_{sf})} = \frac{\lambda}{15}$$

For the Ghana 32 m radio telescope, given an operating frequency of $f = 6.7$ GHz and $\nu = 3.0 \times 10^8$ m/s, the requirements for the RMS surface accuracy of the dish surface are

$$\sigma_{rms} = \frac{3.0 \times 10^8}{15 \times 6.7 \times 10^9} = 2.99 \text{ mm}$$

The requirement for pointing accuracy for the Ghana 32 m Kuntunse radio telescope is less than 10% of the antenna's half-power beam width (HPBW) [11]. Figure 2.10 shows the radiation field pattern of an antenna with main beam, sidelobes, HPBW and FNBW (first null to beam width). The HPBW is the subtended angle of the beam at half-power level (50% power or -3 dB beam width) from the peak of the main beam. The HPBW varies with the antenna aperture illumination or taper, and is given by equation 2.5.2 for typical parabolic antennas.

$$HPBW = 1.2\,\frac{\lambda}{D} \quad \text{in radians} \tag{2.5.2}$$

where D is the primary reflector's outer diameter ($D = 32$ m for the Ghana dish).

$$HPBW = \frac{1.2\,\nu}{D\,f} = \frac{1.2 \times 3.0 \times 10^8}{32 \times 6.7 \times 10^9} \text{ rad} = 0.0962^\circ$$

Therefore, the pointing accuracy requirement ($<$ 10% HPBW) for the Ghana 32 m diameter radio telescope at 6.7 GHz observing frequency is 0.0096°. Similarly, the telescope with an upgraded observing frequency of 18 GHz is expected to meet the surface and pointing accuracy requirements of 1.11 mm and 0.0036° respectively.

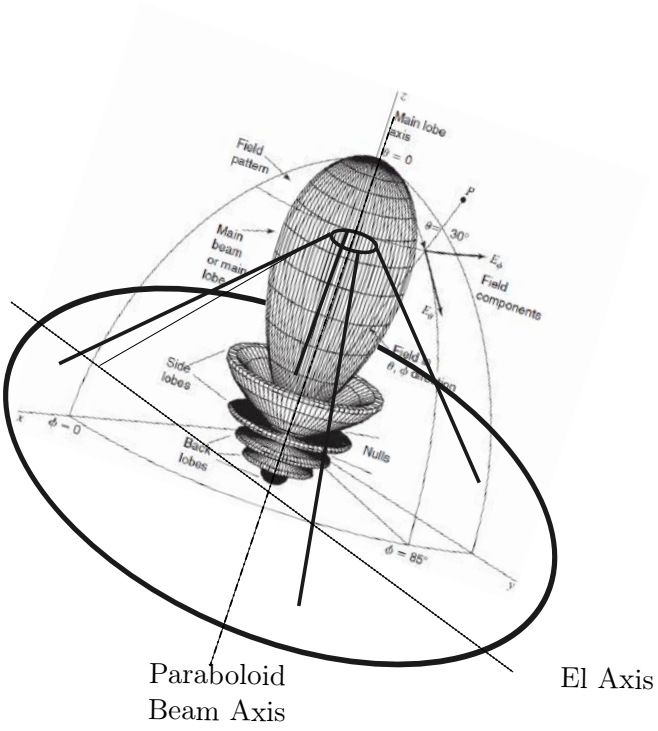

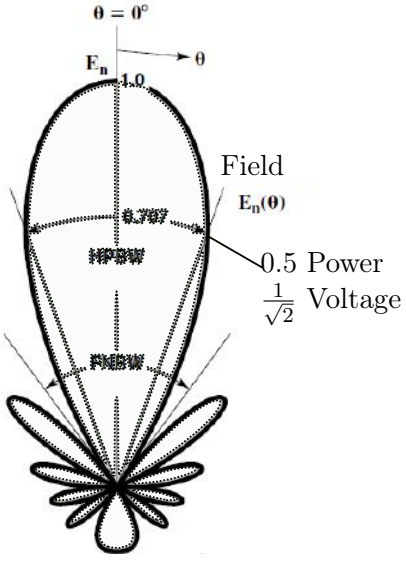

Figure 2.10: Antenna Radiation Pattern (Image Adapted from Kraus and Marhefka [13])

2.5.2 Conversion Activities

The entire conversion project is carried out by six main teams established by SKA-SA namely (a) Structural Mechanical Work Group (SMWG), (b) Con-

trol and Monitoring Work Group (CMWG), (c) Signal Chain Work Group (SCWG), (d) Software Work Group (SWWG), (e) Science Processing Work Group (SPWG), and (f) Project Management Work Group (PMWG). These groups work together to meet a set of AVN user requirements and specifications applicable for VLBI research experiments.

The conversion process was initiated with preliminary structural integrity study and recommendations by a team from the original antenna manufacturer, General Dynamics Satellite Communication Systems (GD SATCOM), USA together with the SKA-SA, SMWG. Prior to this, most moving parts of the telescope required lubrication, especially the bearings which were degreased and freshly lubricated. Other renovation work that followed include the activities below:

1. Replacement of the pintle bearing pads.
2. Re-centering of the antenna's azimuth axis to its nominal centre, ensuring antenna's free azimuth rotation.
3. Replacement of shock absorbers complete with their attachment structures.
4. Repainting of the telescope's structural members.
5. Installation of angle encoders and an optical camera. Drift-scan optical pointing testing was performed.
6. Inspection and refurbishment of all brakes and clutches.
7. Replacement of drive motors.
8. Replacement of the quadrupod legs.
9. Designing, procuring, assembling and commissioning of the Antenna Steering Control System (ASCS).
10. Audit, removal and replacement of all redundant electrical cables, limit switches and emergency stops on the telecommunications system.
11. Replacement of control and monitoring sensors.
12. Installation of lighting systems on the antenna structure.
13. Cleaning of beam waveguide mirrors, the primary reflector panels, and conical feed horn.
14. Demonstrated operation using broadband spectrometer deployed on a ROACH (Reconfigurable Open Architecture Computing Hardware) backend.

2.6 Other Antenna Conversions

Most of the VLBI networks spanning across countries and continents have a mix of converted and newly built radio astronomy telescopes. Examples of converted antennas include the Australia Ceduna, Japan Yamaguchi & Baraki, New Zealand Warkworth, and the USA NASA DSS28. These antennas were mainly telecommunication dishes that transmitted television and radio signals. Telecommunications dishes are often limited to only a few movements and pointing at geostationary satellites.

The requirements for radio astronomy telescopes demand that their design be more robust with stringent accuracy during tracking of distant celestial bodies. Therefore, mechanical and software control system upgrades are usually necessary. A good understanding of the structural behaviour of these telescopes gives an advantage to control system software for pointing at sources with greater accuracy.

In Africa, the equatorially mounted 26 m dish antenna at HartRAO, shown in figure 2.11, was the first converted radio astronomy telescope. It was built by the National Aeronautics and Space Administration of the USA (NASA) in 1961 and known as the Deep Space Instrumentation Facility 51 (DSIF 51). It was used as an earth tracking station for NASA's spacecraft missions until 1974. Now, with the primary reflector panels replaced with solid panels, the radio astronomy telescope attains an RMS surface error of 0.5 mm (surface efficiency of $\eta_{sf} = 79\%$ at 23 GHz observing frequency) at zenith [14].

Figure 2.11: HartRAO 26 m Radio Astronomy Telescope
(Image: `http:hartrao.ac.za/gallery/index.html` - accessed on 30/04/2016)

The 30 m Ceduna radio telescope located in Australia (shown in figure 2.12) was constructed in 1969 by Mitsubishi with an elevation-azimuth mount and feeds located at the Nasmyth focus (i.e. a stationary focus point located about the elevation axis).

Figure 2.12: The Ceduna 30 m Antenna
(Image: `http://www.utas.edu.au/maths-physics/facilities/ceduna-observatory` - accessed on 20/08/2016)

Before the conversion, the antenna was a satellite earth station similar to the Ghana 32 m antenna, until the advent of fibre optics communication rendered it obsolete. The University of Tasmania took ownership of the antenna from Telstra in 1995 to be converted into a radio astronomy telescope. Its conversion to a radio astronomy telescope resulted from the need to expand AT-LBA. The Ceduna telescope achieved a pointing accuracy of 5.556 millidegrees (20") with the replacement of new drive motors and angle encoders. An RMS surface accuracy of about 0.8 mm (surface efficiency of $\eta_{sf} = 55\%$ at 23 GHz observing frequency) was also achieved through survey and surface adjustments [15].

New Zealand's 30 m satellite earth station in figure 2.13 is located in Warkworth township and built by NEC corporation, Japan in 1984. The telecommunications antenna underwent a similar conversion as is being undertaken on the Ghana 32 m antenna. Woodburn *et al.* [16] described the details of the conversion process with some implemented activities required for the upgrade. The surface accuracy of the telescope's primary reflector was investigated with a FARO laser scanner from the ground with the antenna pitched at a 6° elevation angle. A total RMS surface error of 3.5 mm (surface efficiency of $\eta_{sf} = 38\%$ at 6.7 GHz observing frequency) was measured with the laser scanner.

Figure 2.13: New Zealand 30 m Radio Telescope [16]

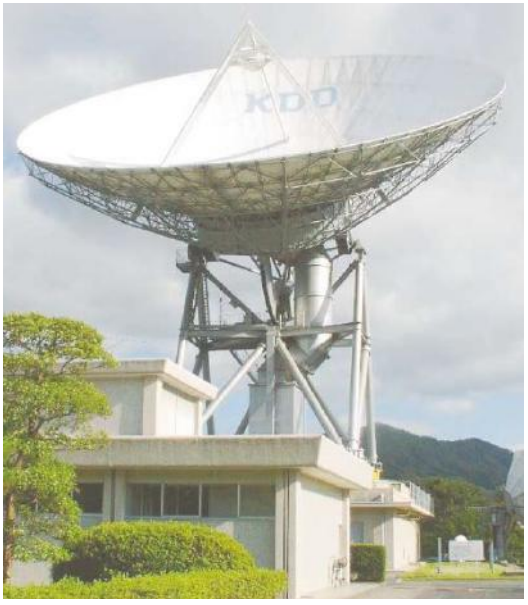

Figure 2.14: Yamaguchi 32m Radio Telescope [17]

Fujisawa *et al.* [17] describes the conversion of the Japan Yamaguchi 32 m Intelsat telecommunication antenna into a radio astronomy telescope in 2001 when it became inoperative. The antenna was constructed in 1979 with an elevation-azimuth drive, mounted on top of a building as shown in figure 2.14, and has a similar configuration to the Ghana 32 m telescope. A preliminary aperture efficiency measurement of 65% at 8 GHz was reported.

2.7 New Built Telescopes

The KAT-7 was built as a demonstration instrument, to prove to the SKA site bid committee that South Africa was capable of building and operating a radio telescope array. It consists of seven 12 m prime focus radio telescopes. Having built KAT-7, the SA government made the decision that even if SA did not get awarded the bid to host the SKA, they would build their own radio telescope array anyway, known as MeerKAT.

The MeerKAT, composed of 64 offset Gregorian 13.5 m radio telescopes, measures an RMS surface error of 0.6 mm (surface efficiency of $\eta_{sf} = 88\%$ at 14.5 GHz observing frequency) for both the primary and the secondary reflectors. Its pointing error is estimated to be within 1.389 millidegree (5") under low-wind and night-time conditions, and 6.944 millidegree (25") during normal operational conditions [18]. Both arrays are situated in the Northern Cape of South Africa. Figure 2.15 shows the Karoo Array Telescopes.

(a) A KAT-7 Dish (b) A MeerKAT Dish

Figure 2.15: The Karoo Array Telescopes (Images courtesy of SKA-SA)

A sister clone to the Ghana 32 m radio telescope is the Medicina 32 m radio telescope, located in Bologna, Italy, which has been in operation since 1983. It is a member of the EVN. The telescope's primary reflector consists of 240 panels. The secondary reflector is equipped with a sliding mechanism that permits its use as both a primary focus and Cassegrain focus dish. During the primary focus mode, the secondary reflector is completely retracted as shown in figure 2.16. At the Cassegrain focus, the angular movement of the hyperbolic secondary reflector aids the use of each of the nine receivers. The RMS surface accuracy and pointing error of the Medicina 32 m radio telescope are estimated to be 0.6 mm (surface efficiency of $\eta_{sf} = 74\%$ at 22 GHz observing frequency) and 8" respectively [19].

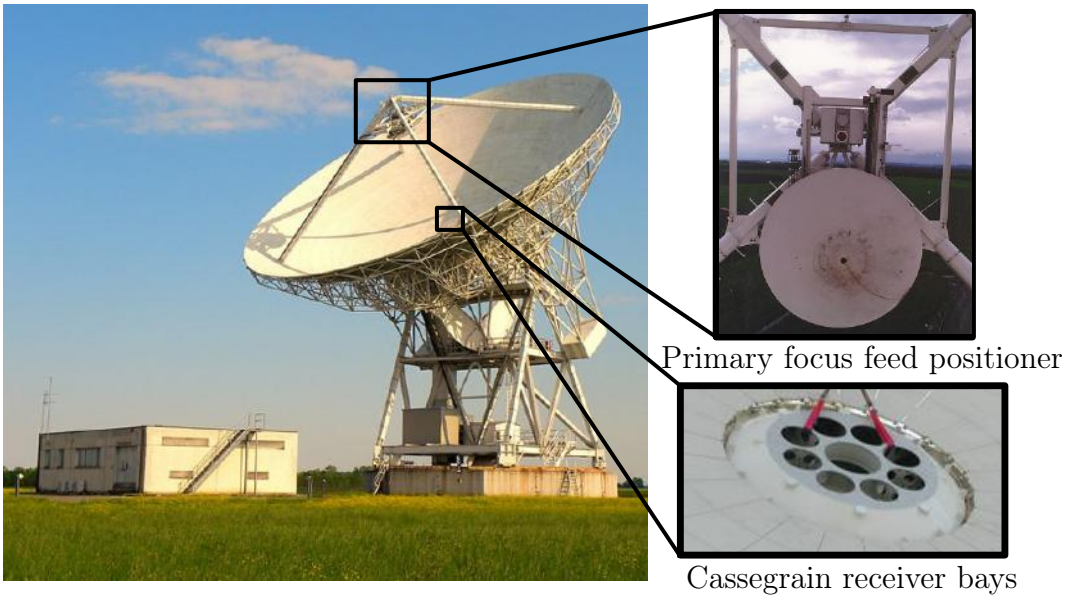

Figure 2.16: Medicina 32 m Telescope (Image adapted from Cenacchi *et al.* [19])

The 30 m Noto VLBI radio telescope, also in Italy, has a similar structural design configuration as the Medicina radio telescope, except that it also employs the use of active surface system controls to compensate for the gravity induced deformations on the primary reflector surface. The 244 automatically programmed actuators are situated at the corners of the primary panels to produce a 0.1 mm RMS primary surface accuracy. This enables observations at higher operating frequencies, up to about 86 GHz as presented by Orfei *et al.* [20].

Montaguti *et al.* [21] used a terrestrial laser scanning technique to capture and quantify the primary reflector deformations for both the Noto and Medicina radio telescopes. A 1.8 cm to 4 cm change in the best-fit focal length from the theoretical focal length was registered for both radio telescopes, over a 90° to 15° elevation angle range.

The Green Bank Telescope (GBT), located in West Virginia, is a 100 m offset Gregorian radio astronomy telescope with an elevation-azimuth mount as shown in figure 2.17. It is currently the world's largest fully steerable telescope equipped with computer-controlled active surface actuators situated at the 2004 primary panel's corners. Prestage *et al.* [22] submitted an article on the advanced metrological systems employed to extend the observing frequency up to 115 GHz with a pointing and RMS surface error target of 1.3" and 210 µm respectively.

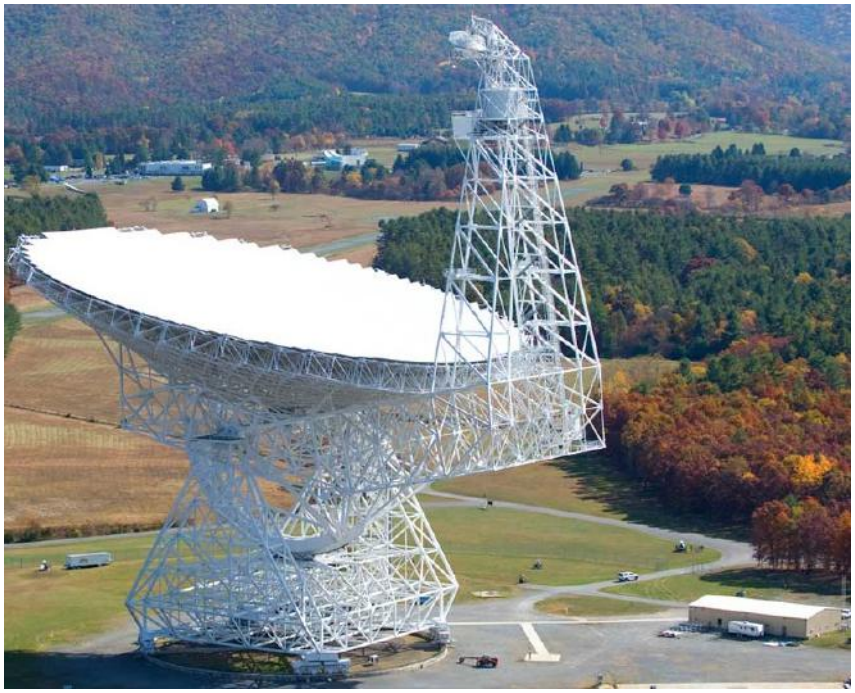

Figure 2.17: The GBT Telescope (Image courtesy of NRAO)

Chapter 3

Numerical Modeling the Radio Telescope

The Ghana 32 m antenna is a complex structure which weighs about 240 tonnes with material composition mainly of steel and aluminium. It is mounted on top of an office building that houses offices, control systems and other digital backends of the earth station. The structural data available for the antenna is the manufacturing drawings in a hand drafted format created by Telesystem International Wireless (TIW Systems) Inc., a subcontractor to GD SATCOM in the late 70s [9]. It has a Cassegrain focus with beam waveguide, paraboloid primary dish reflector, and a fixed hyperboloid secondary reflector. The antenna is piloted to point at satellites or cosmic source(s) by means of its elevation and azimuth servo drive train system. These rotation axes are theoretically perpendicular to each other. Radio emissions from the sky bounce off the primary and secondary reflectors, and are transmitted through a beam waveguide (BWG) to the control and processing room.

In this chapter, a CAD model is generated from the drawing data pack to provide a more accurate mass data as a validation check to the FE model. The CAD model is also useful in verifying the mass balance around the elevation axis. Finally, the FE model of the Ghana 32 m Telescope is created and simulates various operational loading conditions that result in structural deformations of the antenna.

3.1 Nomenclature

The naming and reference axis system described in this section ensures consistency in both the CAD and FE models. The cross-elevation, elevation and beam (or focal) axes are respectively defined in the X, Y, and Z-axis direction of the reference frame located at the primary reflector vertex as discussed in section 3.1.1. The normal, side and axial wind forces also respectively assumed

positive signs with the direction of the axis frame at the dish vertex. Gravity and thermal gradient loads reference the global axis frame.

3.1.1 Coordinate Frames

The model's global coordinate system has the X-axis running along the top of the track rails with the Z-axis defining the azimuth axis of the telescope structure. The Y-axis aligns parallel to the elevation axis of the telescope. In addition to the global coordinate reference system, five other local coordinate frames exist as illustrated in figure 3.1. These local coordinate frames define the counterweight's centre of mass, elevation axis, datum, and primary reflector panel vertex reference. Table 3.1 provides details of all the reference coordinate frames used in creating the FE and the CAD model.

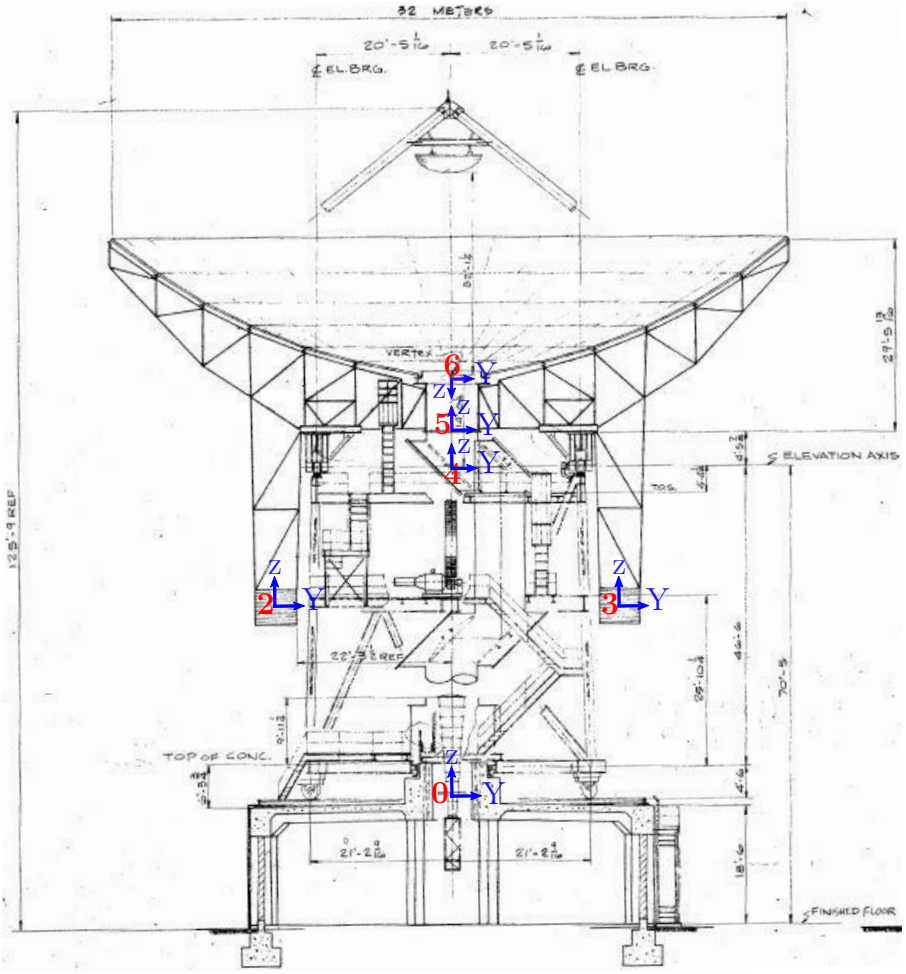

Figure 3.1: Cartesian Reference Frames: Frame 0 represent the Global Reference and Frame 2, 3, 4, 5, 6 represent the Local References (Image adapted from TIW [9])

Table 3.1: Summary of Model's Reference Frames

Name	Description
Axis-0	Defines the telescope's azimuth axis along its Z-axis
Axis-2 & 3	Defines the centre of mass of counterweights
Axis-4	Defines the elevation axis along its Y-axis
Axis-5	Defines the datum for the backup structure
Axis-6	Located at primary reflector vertex and defines nodal vectors of primary reflector panels

3.1.2 Unit System

The manufacturing drawing data presented information of the antenna structure in imperial units. However, the FE and CAD model adopt the SI unit system. This required the original hand-drafted data to be converted to the SI system in order to measure distance, mass and time data in meter (m), Kilograms (Kg) and second (s) respectively.

3.2 The CAD Model

The CAD model of the Ghana 32 m telescope constitutes about 7800 components with different cross-sectional properties developed from the available manufacturing drawing data [9] and on-site measurements. The naming convention for the model adopts the SKA-SA nomenclature and breaks the model into two main assemblies;

1. The Elevation System, and
2. The Alidade Structure

The elevation system describes all moving parts about the elevation axis of the telescope structure. The elevation system is mounted on an alidade structure that rotates about an azimuth axis on a fixed track rail mounted on top of a concrete office building.

The CAD model was developed with the 3D parametric modelling capability of SolidWorks software package. The two main assemblies of the model were further grouped into sub-assemblies to generate the complex geometry of the telescope structure efficiently. Details such as the truss joints, gussets, bolts/washers/nuts, screws, and rivets were excluded. The material properties described in Appendix A were applied on the model structure to calculate their components masses.

3.2.1 Elevation System

The elevation assembly consists of the following sub-assemblies; (a) quadrupod legs, (b) primary reflector panels, (c) backup structure, (d) counterweight structure, (e) elevation wheel, and (f) the elevation axle as shown in figure 3.2a.

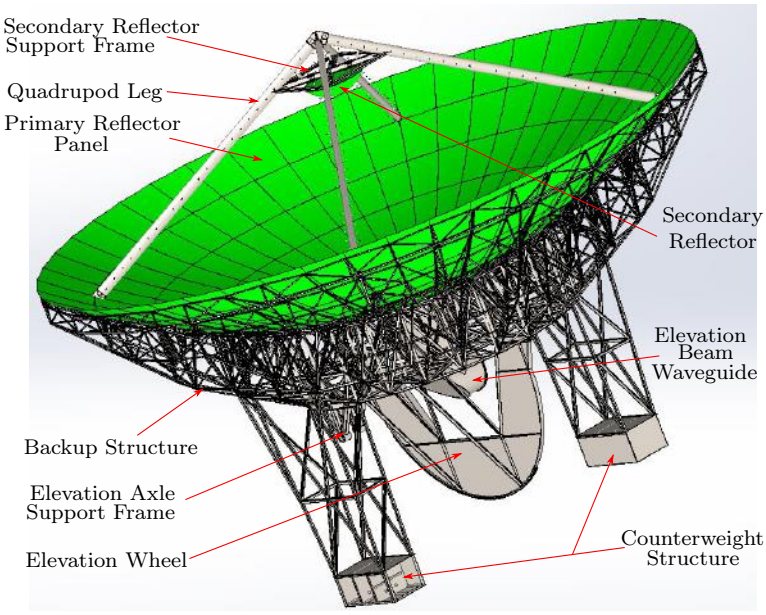

(a) Elevation System

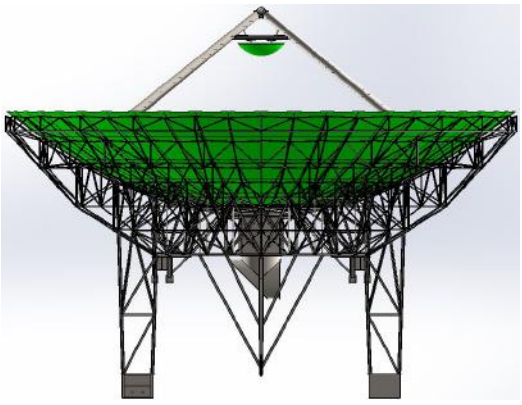

(b) Front View

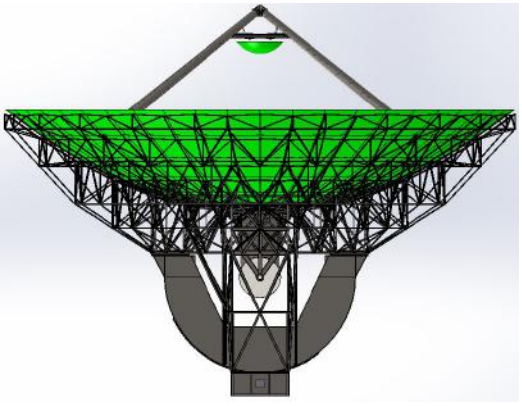

(c) Side View

Figure 3.2: Ghana 32 m Telescope Elevation System

The quadrupod legs, secondary reflector support frame, and the secondary reflector make up the quadrupod assembly. The primary reflector panels consist of 240 aluminium panels forming the paraboloidal surface. The backup structure has 7 different types of radial trusses forming the 48 radial trusses with linking structures. The backup structure supports the panels and the

quadrupod assembly. The elevation wheel, counterweight structure, and elevation BWG are also assembled to the backup structure. A pinion and gears arranged on the elevation wheel enable the elevation system to be driven by a drive train system mounted on the alidade mid platform structure.

Table 3.2 compares the elevation component's rotating masses, the centre of masses' distances, and moment of inertia from the elevation axis for the TIW manufacturing drawing data, CAD and FE models.

Table 3.2: Mass Moment of Inertia for Elevation Components

No.	Description	Mass M [Kg]			x [m]			Mass Moment Mx [kg.m]		
		TIW Data	FE Model	CAD Model	TIW Data	FE Model	CAD Model	TIW Data	FE Model	CAD Model
1	Secondary reflector	272	272	272	14.33	14.52	14.61	3,899	3,951	3,977
2	Secondary reflector support	2,722	4,768	4,647	12.80	13.57	13.58	34,840	64,684	63,104
3	Primary reflector panel	11,793	9,924	14,557	7.71	7.63	7.47	90,944	75,677	108,775
4	Reflector backup structure	49,895	57,853	54,497	4.42	3.35	3.53	220,517	194,037	192,326
5	Elevation wave guide shroud	454	797	1,106	1.83	0.24	0.43	830	194	477
6	Elevation wheel	5,443	12,690	11,957	-3.05	-2.19	-2.22	-16,591	-27,730	-26,566
7	Counterweights	44,543	44,543	44,543	-6.71	-6.71	-6.71	-298,686	-298,703	-298,686
8	Elevation gear	1,179	931	844	-4.88	-5.20	-5.29	-5,751	-4,837	-4,469
9	Counterweight structure	7,257	6,072	6,072	-6.10	-6.72	-6.72	-44,242	-40,832	-40,832
10	Elevation bearing	1,814	1,814	1,814	0.00	0.00	0.00	0	0	0
	Total	**125,373**	**139,664**	**140,310**	**20.36**	**18.50**	**18.68**	**-14,240**	**-33,558**	**-1,894**
	% Difference	**0%**	**11%**	**12%**	**0%**	**-9%**	**-8%**	**0%**	**136%**	**-87%**

x represent component's center of gravity (CG) distance from the elevation axis

The % difference in table 3.2 indicates the total percentage differences between the TIW mass and the FE/CAD model's mass. One of the main differences between the masses of the sub-systems of the TIW data pack and the FE/CAD model can be attributed to the difference in sub-systems' components grouping not clearly defined in the TIW documents. Other factors affecting the mass discrepancies are addressed in section 3.2.3.

The effect of the large difference in the designer's primary reflector panels mass and that of the FE/CAD model (almost 20% increase if weighted against the total) was investigated to check its influence on the telescope RMS surface and pointing error. The FE model reflector panel mass was increased by 20% by adjusting the material density for this study. The load case for the analysis considered the telescope at 0°, 60°, and 90° elevation angle under the gravity, thermal gradient load of 8 K and 5.6 m/s steady-state wind load speed.

Table 3.3 shows the telescope's RMS surface and pointing error sensitivity to the change in the mass of the primary reflector panels. The results shows the

Table 3.3: Effect of Change in Reflector Panel Mass on Total Error

Elevation Angle [°]	RMS Surface Error [mm]			Pointing Error [°/(")]		
	FEM 1	FEM 2	% Difference	FEM 1	FEM 2	% Difference
0	0.536	0.714	28	0.0019 (6.84)	0.0051 (18.36)	91
60	0.727	0.834	14	0.0014 (5.04)	0.0033 (11.88)	81
90	1.011	1.038	3	0.0047 (16.92)	0.0047 (16.92)	0

FEM 1 - Original FE Model

FEM 2 - FE Model with 20% increase in the mass of the primary reflector mass

reflector panel mass as a major contributor to the total error especially at lower elevation angle. Further on-site investigation is therefore required to ensure the reflector panels mass is a representative of the actual telescope panel on site.

3.2.2 Alidade System

The alidade structure supports the elevation system and also rotates the telescope structure about the azimuth axis on the track rails by means of the azimuth drive system. The alidade structure carries both the elevation and azimuth drive systems, the platforms and ladder structures, the elevation bearing and the BWG mounted on top of a pintle cable wrap house. The BWG houses alternating flat and concave mirror arrangements that bounce the radio waves to the feed horn for further processing.

Figure 3.3 shows the alidade structure assembly with mass components in table 3.4.

Table 3.4: Mass of Alidade Components

Item No.	Description	TIW Data	FE Model	CAD Model
1	Azimuth wave guide shroud	3,629	4,741	5,537
2	Elevation drives	4,536	4,536	4,536
3	Azimuth mount	72,575	70,137	71,830
4	Azimuth drives & wheels	9,525	9,525	9,525
5	Pintle bearing & post	2,631	3,441	3,441
6	Ladder & platform	3,629	4,239	9,560
	Total	**96,524**	**96,619**	**104,430**
	% Difference	**0%**	**0%**	**8%**

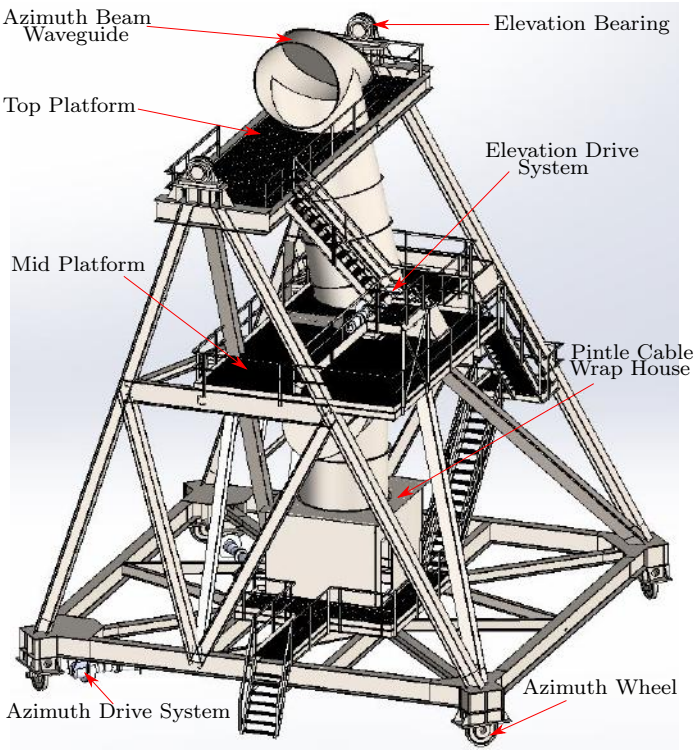

(a) Alidade System

(b) Front View

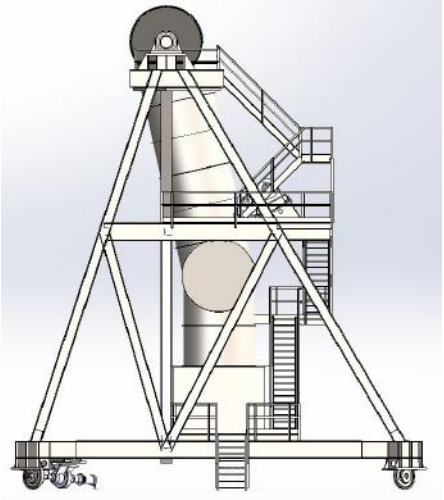

(c) Side View

Figure 3.3: Ghana 32 m Telescope Alidade System

3.2.3 Discrepancies in TIW Data and Actual Antenna

The structural drawings documented in the TIW manufacturing data were first hand drafted in 1978 and over the years, the telescope has seen some renovations or modifications which were either not documented or lost from the site archive. The first visible change observed from the site is the main beam connecting the counterweight structure to the backup structure. This is a hollow pipe circular section contrary to the hollow square pipe section seen in the TIW manufacturing drawing as shown in figure 3.4. Severe corrosion on the quadrupod legs necessitated a complete replacement by SKA-SA. Also, a few detail dimensions on the quadrupod legs were obtained from site photos or measurements on the actual antenna which were not sufficiently provided on the drawing data.

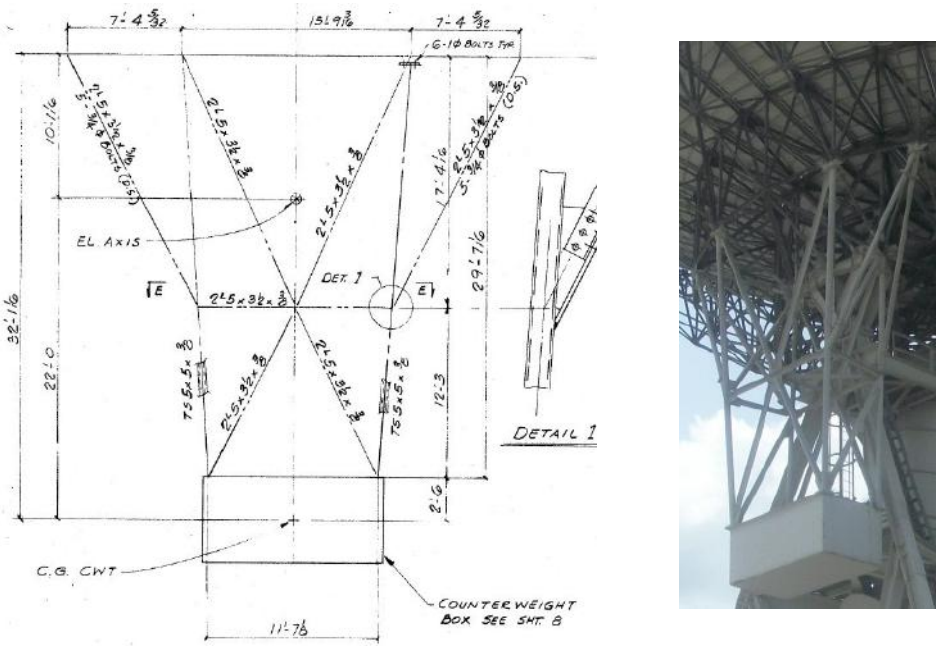

(a) Square Pipe Support Frame (TIW) (b) Circular Pipe Support Frame (Site)

Figure 3.4: Counterweight Support Frames

3.3 FE Model

In developing the Ghana 32 m telescope numerical model, components with very little significance to the mass and/or stiffness of the telescope structure were simplified or deleted to avoid unnecessarily complicating the model, while still remaining conservative. Most load carrying and load transferring properties were retained as described next in section 3.3.1. The components or assemblies showing symmetry of structure, loads, and boundary conditions were fully exploited in creating the full model.

The FE model comprises 61 different types of structural members with sectional properties summarised in Appendix A. This includes different sizes of angle irons, channels, T-sections, Z-sections, I-Beams, circular hollow sections (CHS), square hollow section (SHS), solid bars, and elliptical hollow sections. The FE model created has 110,032 elements that consist mainly of beam, shell, and lumped mass elements. The model has a total of 608,151 degrees of freedom (DOF) and 464 RBE2 elements. The geometrical positions of these elements are referenced from the TIW drawing data and the CAD model with 5 local coordinate frames as described in table 3.1. Table 3.5 tabulates the mechanical and physical material properties of the telescope's FE model components with material specifications referenced from the original designers drawing data pack [9]. The MSC Patran/Nastran software package [23, 24] was used in generating and solving the FE model.

Table 3.5: Material Properties for Ghana 32 m Telescope

Material	**Density [Kg/m^2]**	**Poisson Ratio**	**Young's Modulus [GN/m^2]**	**Thermal Expansion [m/m.K]**	**Application Region**
Al 6061 T6	2700	0.33	68.9	22.2 x 10^{-6}	Primary reflector panels
ASTM A36	7850	0.26	200	12 x 10^{-6}	Alidade, backup structure, etc.
AISI 1022	7868	0.29	205	12 x 10^{-6}	Elevation axle
AISI 1040	7845	0.29	200	12 x 10^{-6}	Azimuth axle

Reference: *www.matweb.com*

3.3.1 Model Simplifications

Most components of the telescope structure, especially the backup structure, are composed of double angle irons arranged in two main configurations, back-to-back and flange-to-edge bolted together with gussets linking other structures. These are simplified to T- and Z-sections as shown in figure 3.5.

Figure 3.5: Simplified Double Angle Iron Sections

The total cross-sectional areas for the back-to-back and flange-to-edge angle irons are maintained in the simplified models and therefore assumed to be the same for truss structures.

The backup and alidade structures were modelled with 1D beam elements. Both the azimuth and the elevation axle were also modelled with 1D beam elements with their smallest nominal shaft sectional area. The primary reflector panels, elevation wheel, azimuth wheel and the BWG were all created with 2D shell elements. The stiffened support structure carrying the azimuth drive system and the entire telescope structure favoured modelling it with 2D shell elements as shown in figure 3.6. The azimuth servo drive system was modelled as a lump mass element.

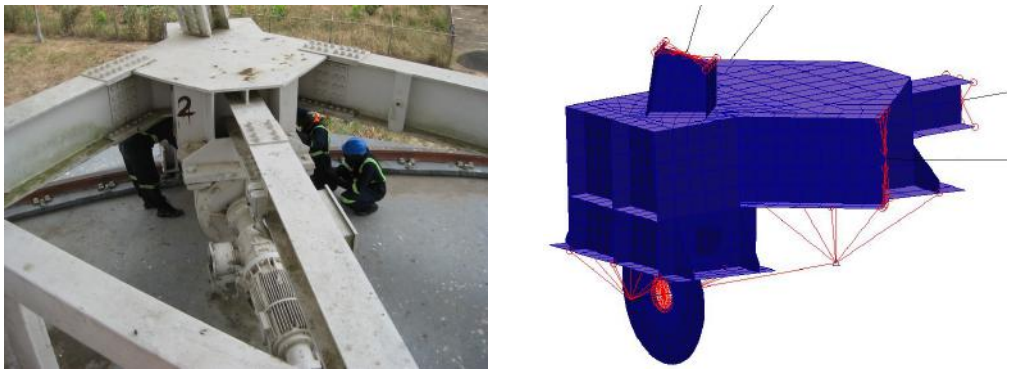

(a) Azimuth Drive Support (b) FE Model of Azimuth Drive Support

Figure 3.6: Azimuth Drive Support and Wheel

The counterweights, secondary reflector, elevation servo drive system, and platforms are simplified as lumped masses at their respective centres of mass due to their negligible influence on the telescope's structural stiffness. The quadrupod assembly and primary reflector panels are connected to the backup structure using RBE2 elements. The azimuth and elevation servo drive mass elements are connected with RBE2 elements to the alidade structure. Generally, RBE2 elements connect the point masses, beams, and shell elements together.
Figure 3.7 shows the lump mass and RBE2 connections on the counterweight and quadrupod assembly.

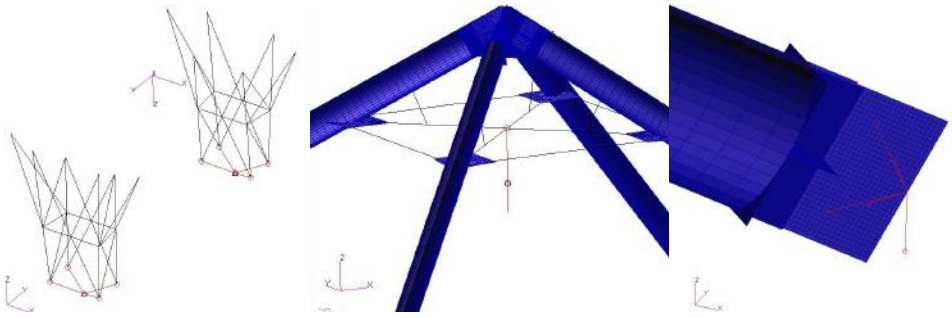

(a) Counterweight (b) Quadrupod Assembly (c) Quadrupod Leg

Figure 3.7: Counterweight and Quadrupod Lump Masses and RBE2

3.3.2 Primary Reflector Panels

The 1.6 mm aluminium primary reflector panels were modelled with stiffened Z-section aluminium profiles in both the radial and circumferential direction as shown in figure 3.8. The panels are bolted to the radial trusses of the backup structure by means of adjustable panel supports. These panel supports were simplified with RBE2 elements which connect the beam stiffened shell elements with the backup structure's beam elements. The first two circumferential rows consist of 24 panels each and the third to the sixth row, 48 panels each totalling 240 panels. Figure 3.9 shows the reflector panel's shell elements consisting of 11,496 surface nodes which reference a local axis located at its vertex. This local axis system is vital to the telescope's error analysis.

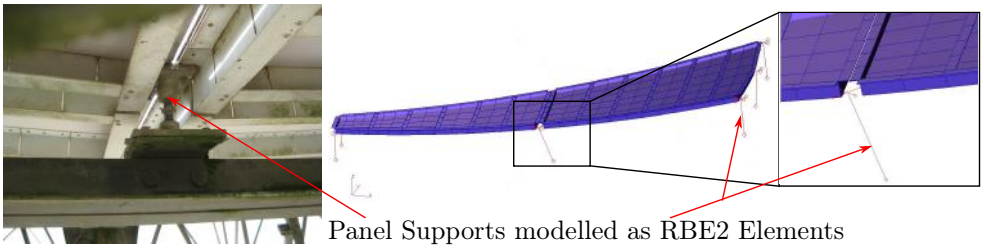

Figure 3.8: Primary Reflector Panel Support

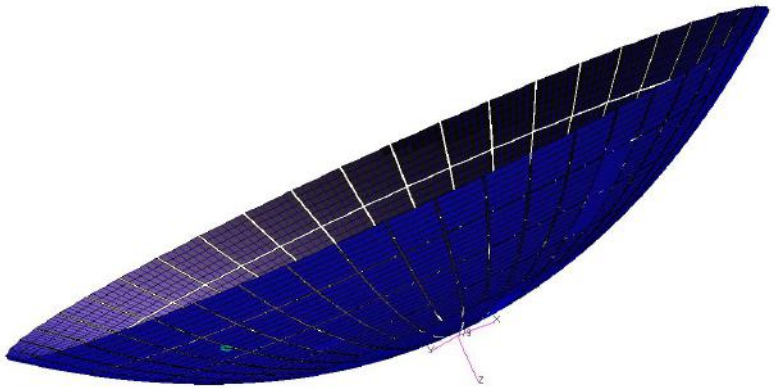

Figure 3.9: Primary Reflector Panels

Figure 3.10 is a complete FE model of the Ghana Kuntunse 32 m radio telescope. The exclusions and assumptions mentioned earlier in section 1.2.2 and section 1.2.3 respectively apply to the model. The model's product breakdown structure is also shown in figure 3.11. This details the naming system and the hierarchical order of assemblies/sub-assemblies used in creating the FE model.

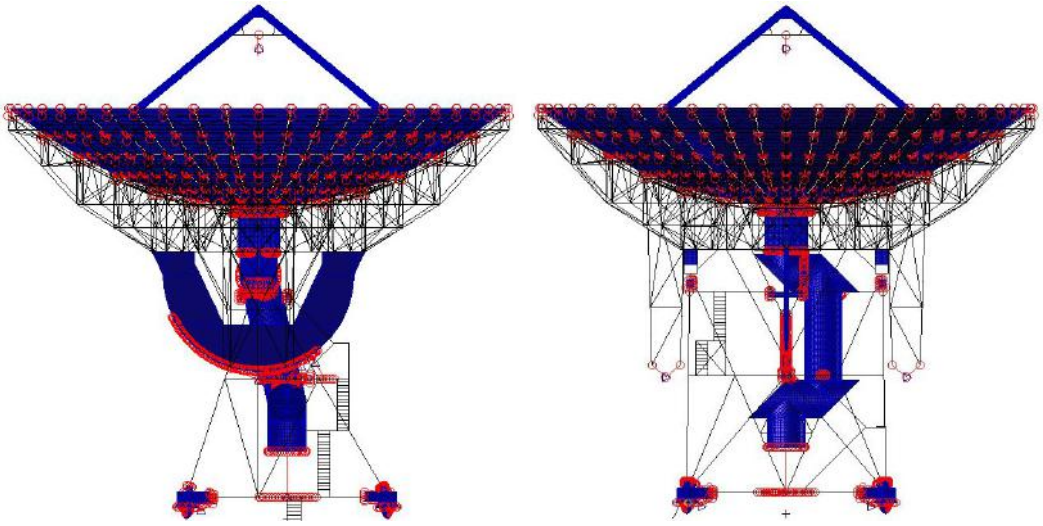

(a) Side View (b) Front View

Figure 3.10: Ghana 32 m telescope FE Model

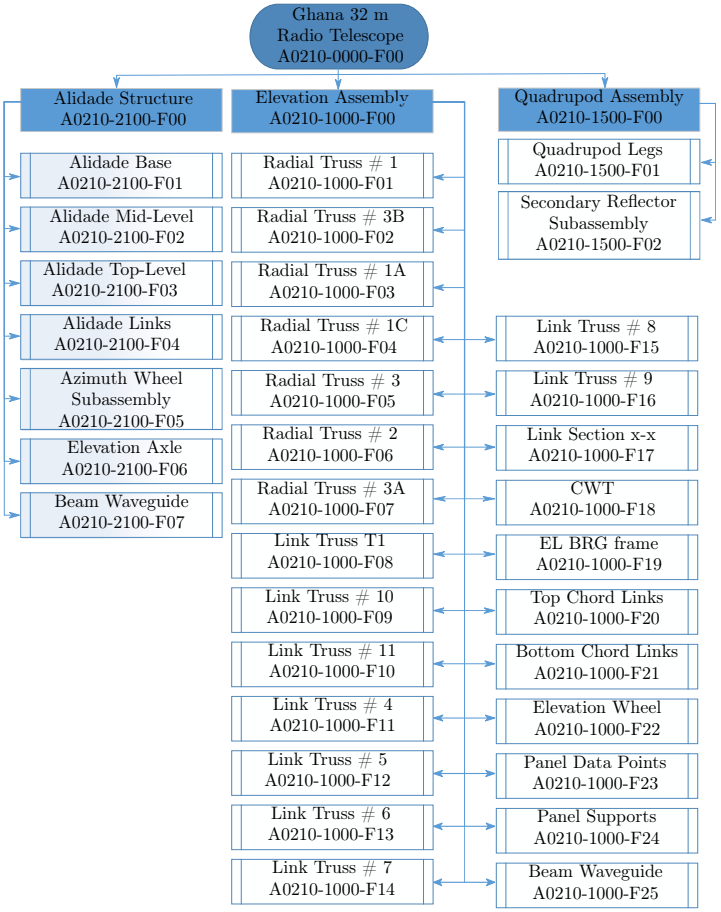

Figure 3.11: FE Model Product Breakdown Structure

3.3.3 Boundary Conditions

The nodes located on the bottom part of each azimuth wheel touching the track rail are fixed in all its DOFs. A pin joint allows rotation between the elevation shaft and bearing to permit the free rotation of the elevation structure assembly. RBE2 elements are placed at the two nodes where the pinion gears make contact with the elevation wheel gear to simulate its braking effect. The elevation and azimuth BWGs are also connected together with RBE2 and RBE2 spider elements with free rotational DOFs about the elevation axis. Figure 3.12 shows the RBE2 spider wagon on the elevation and azimuth BWG.

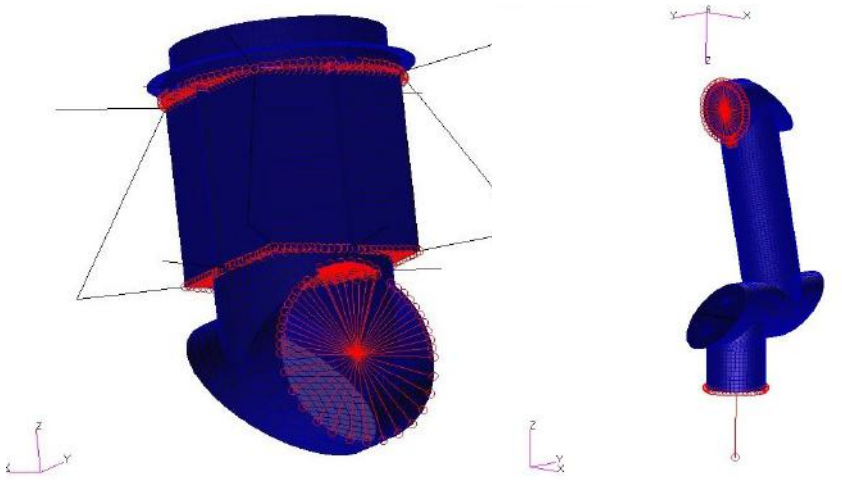

(a) Elevation BWG (b) Azimuth BWG

Figure 3.12: Elevation and Azimuth BWG RBE2

This research work did not attempt to provide in-depth details on the Ghana 32 m radio telescope's structural analysis such as stress analysis due to the complex geometry development of the numerical model. Therefore, the research focused on the deformation fields, especially for the primary reflector and it impacts on the overall pointing error model.

3.4 Structural Deformations

In a typical application, environmental and operational conditions prevailing at the telescope's site translate into external loads that influence the shape and position of the parabolic dish. These external loads are in the form of wind loading, uneven heating and cooling from the sun, and gravity as illustrated in figure 3.13. These result in the structure deforming and thereby degrading the pointing performance of the instrument. The subsequent section explains how these external loads are quantified, implemented, and simulated in the telescope's numerical model.

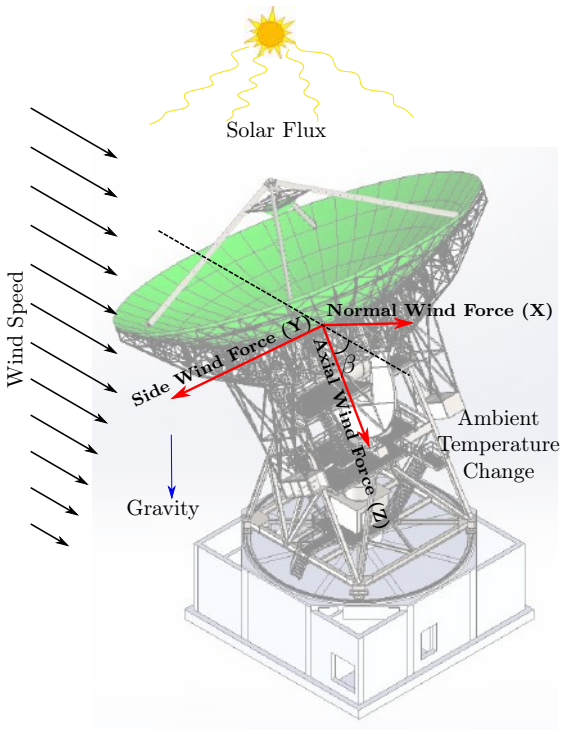

Figure 3.13: External Loads on Telescope

3.4.1 Gravitational Effect

The gravitational force results in the telescope's structural components bending under its own weight. A one (1) g translation downward inertia load in the negative global Z-axis is applied to the FE model. This simulates the gravitational load on the entire telescope structure, using the supplied material densities and the internally calculated element volumes to determine their gravitational forces.

The gravity load on the radio telescope is a function of its elevation angle. Five load cases were implemented which considered the telescope dish oriented at 0°, 60°, 90°, 120°, 180° elevation angles as shown in figure 3.14. Load cases at 120° and 180° elevation angle represent the telescope at 60° and 90° elevation angle rotated through 180° azimuth angle to establish a basis for comparison with the wind and thermal load cases and also check loading consistency in the numerical model.

3.4.2 Wind Loading

The telescope structure is usually subjected to two main types of wind loads, namely, static wind load and wind gusts. The static wind load is a steady state load and is represented as aerodynamic pressure loads exerted on the reflector's paraboloid dish. On the other hand, the wind gust is stochastic,

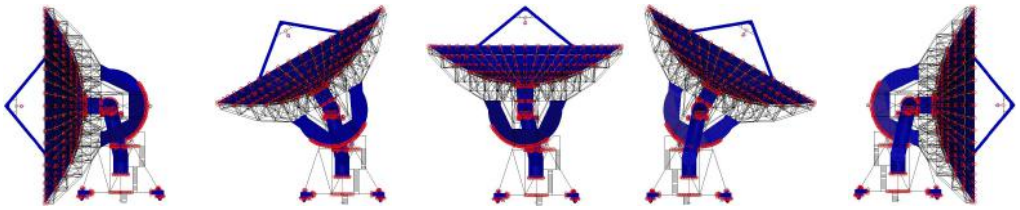

(a) 0° El (b) 60° El (c) 90° El (d) 120° El (e) 180° El

Figure 3.14: FE Model Load Case Orientations

resulting in oscillations of the telescope structure. Gawronski *et al.* [25],[26] presented the analytical model of the wind gust effect on the NASA Deep Space Network (DSN) antennas based on the Davenport spectra. However, this research focuses on steady-state wind loading.

To derive the static wind load on the dish, a typical day is assumed with a 13.41 m/s (30 mph) wind speed on the Ghana 32 m diameter dish. The components of the wind force are referenced from the dish vertex axis as shown in figure 3.13 with β as the elevation wind attack angle. Similar dish orientation load cases (0°, 60°, 90°, 120°, and 180° elevation wind attack angles) to the telescope's gravitational load cases were considered.

The aerodynamic nodal wind force, F^i_{sw} exerted on the reflector dish surface of the numerical model is calculated from equation 3.4.1 [27, 28].

$$F^i_{sw} = q\ C^i_d\ A^i_{pda} \tag{3.4.1}$$

where

$$q = \frac{1}{2}\ \rho\ v^2$$

and q is the dynamic pressure, C^i_d is the nodal drag coefficient, A^i_{pda} is the projected dish surface area per grid normal to the wind direction, ρ is the density of air, and v is the wind speed.

Assuming an air density ρ of 1.1684 kg/m^3 at an average site temperature of 25 °C, pressure of 101 kPa and dew point of 22 °C, the dynamic pressure, q is computed as:

$$q = 105.056 \text{ Pa}$$

The nodal drag coefficient, C^i_d varies across the dish surface and also depends on the orientation of the dish with respect to the wind angle of attack, β. Kron [28] presented a means of extending existing wind tunnel pressure coefficients from the work of Levy and Kurtz [29] and Fox [27] to other antennas. The focal-to-diameter ratio of the wind tunnel test data provided by Kron [28] ($\frac{f}{D}$=0.33)

closely matches that of the Ghana 32 m telescope with $\frac{f}{D}$=0.32. The wind force computed using this wind tunnel test data only accounts for the loading on the parabolic dish surface and therefore excludes the remaining components of the telescope structure. This is conservative as the telescope dish (80% of the total telescope's surface area exposed to the wind) is the main contributor of the wind loading to its surface deformation. The remaining components are mostly alidade structural beams which are more stiffened to wind resistance and constitutes 20% of the total telescope's surface area exposed to the wind.

An external program written in Python was used to generate the wind tunnel test nodal positions that fit the topography of the Ghana 32 m telescope dish. The nodal positions are determined from the radius-to-diameter ($\frac{R}{D}$) ratios of forty-four wind tunnel test nodes with their corresponding angular positions and pressure coefficients. Figure 3.15a to 3.15e show the contour plots of the wind tunnel test pressure coefficients at 0°, 60°, 90°, 120°, and 180° wind angles of attack respectively. The pressure coefficients for the 11,496 nodes on the Ghana 32 m dish surface are then calculated by interpolating these nodal coefficients as shown in Figure 3.16a to 3.16e.

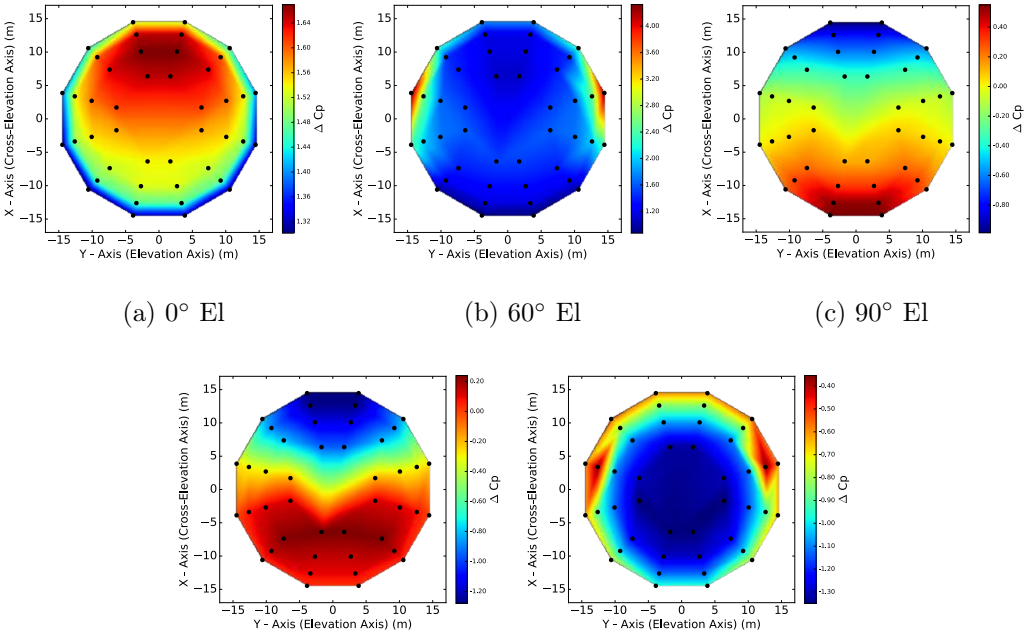

(a) 0° El (b) 60° El (c) 90° El

(d) 120° El (e) 180° El

Figure 3.15: Wind Tunnel Test Pressure Coefficients for a dish with $\frac{f}{D} = 0.33$ (Kron 1971)

The integral of these pressure coefficients gives the primary reflector pressure coefficient for a given β orientation of the radio telescope. The wind tunnel

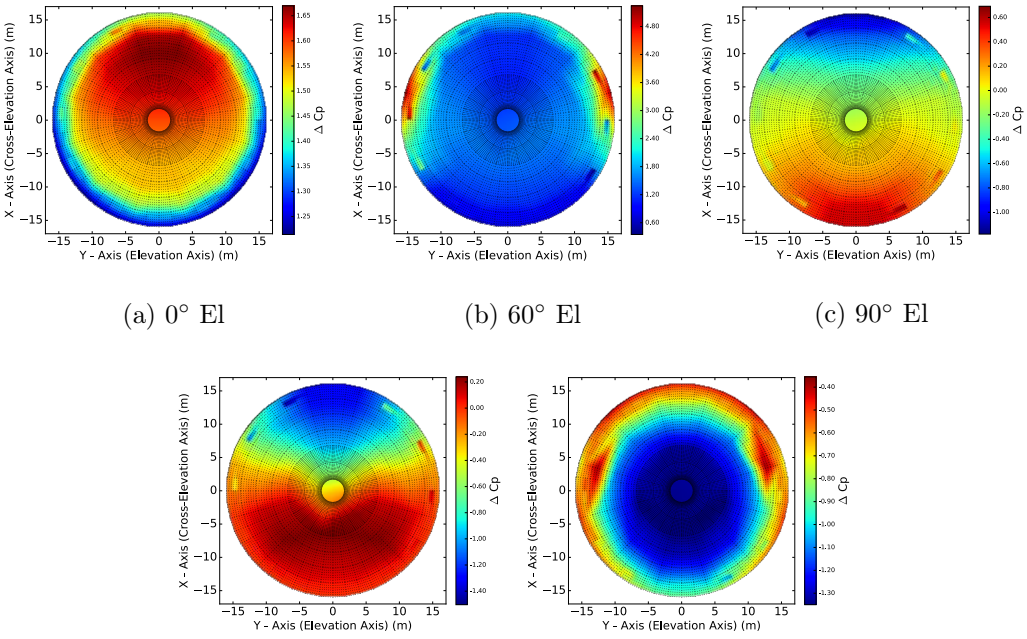

(a) 0° El (b) 60° El (c) 90° El

(d) 120° El (e) 180° El

Figure 3.16: Interpolated Pressure Coefficients for Ghana 32 m Telescope with with $\frac{f}{D} = 0.32$

test data shows that the dish at 60° elevation wind attack angle results in a high-pressure coefficient distribution over the entire dish surface as seen in figure 3.15b. In this position, the dish behaves like an aerofoil providing a high reactive resistance to the wind angle of attack. Figure 3.15c gives the least resistance to wind pressure which is consistent with the stowing position of the elevation system during severe or survival wind conditions. A plot of the mean pressure coefficient at each wind attack position is shown in figure 3.17.

The nodal area associated with each dish surface grid can be computed by applying 1 Pa uniform pressure on the dish surface and extracting the resulting nodal force which represents the weight factor of each grid. Equation 3.4.2 shows the nodal force generated by pressure P exerted on an element surface.

$$F_i^e = \int P \; N_i^e \; dA \tag{3.4.2}$$

Now substituting, $P = 1$,

$$F_i^e = \int N_i^e \; dA = A_i$$

Each quad elements on the dish surface assign $\frac{1}{4}$ of its nodal force denoted as N_i^e under 1 Pa pressure to each node and upon matrix assembly in MSC

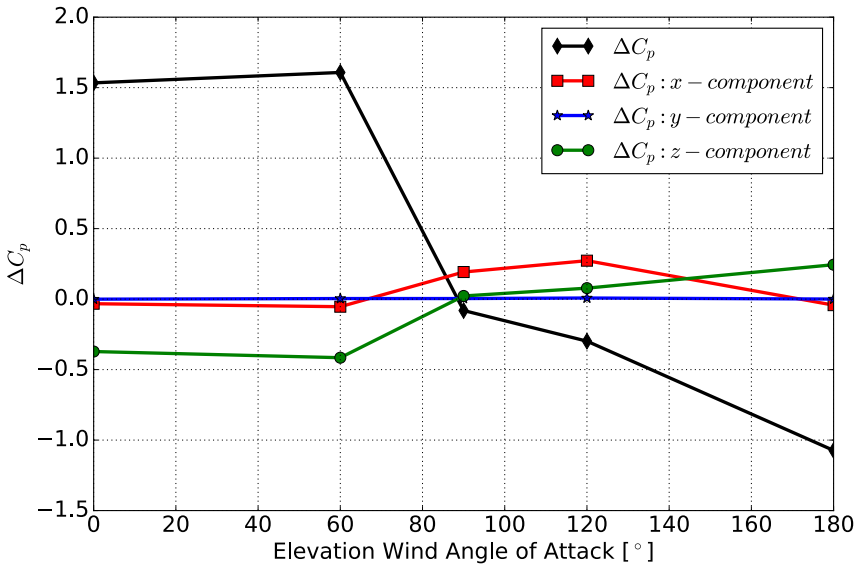

Figure 3.17: Mean Pressure Coefficients at Different Elevation Angle

Patran/Nastran, the nodal forces represent the surface area, A_i associated with each grid node. The integral of these nodal areas is the total surface area, A_{pda} which correlate well with the projected net area from the CAD model as elaborated in table 3.6.

Table 3.6: Projected Dish Area of the Ghana 32 m Radio Telescope

Area	**Wind Attack Angle, β**		
	0°/180°	60°/120°	90°
Projected Area [m^2]	807.06	407.88	134.04
Net Area (CAD Model) [m^2]	704.62	352.31	118.64
Net Area (FE Model) [m^2]	706.78	358.36	118.96

The difference between the projected dish area and the net areas is the gap sizes in between the panels along its circumference and radial length. The difference between the net areas of the CAD model and the FE model is the panel's discretized edge approximations in the FE model's quad element construction and can be further reduced by mesh refinement.

The static wind force on each panel FE node, F_{sw}^i is evaluated using equation 3.4.1, and then applied to the FE model as input load to simulate the wind loading effect. Figure 3.18 and 3.19 show the wind force vector plot and the nodal wind load on the Ghana 32 m diameter dish at different elevation angle orientations.

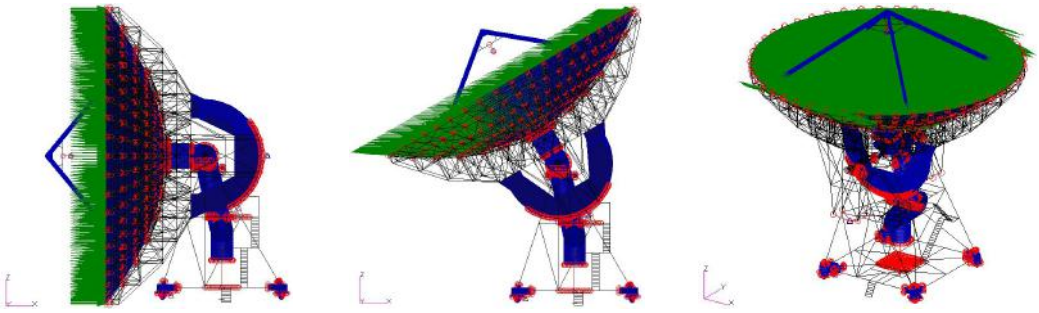

(a) 0° El (b) 60° El (c) 90° El

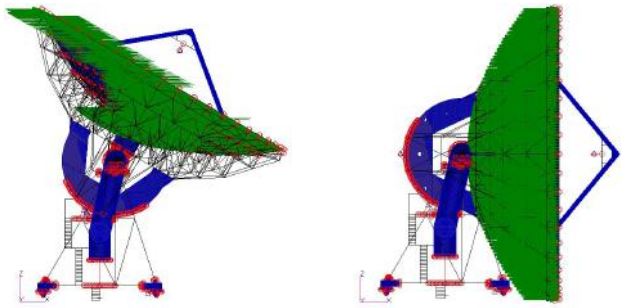

(d) 120° El (e) 180° El

Figure 3.18: Vector Plot of Wind Force at 13.41 m/s Wind Speed

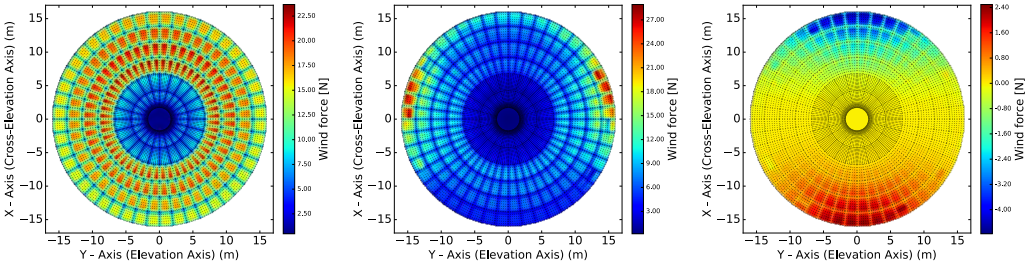

(a) 0° El (b) 60° El (c) 90° El

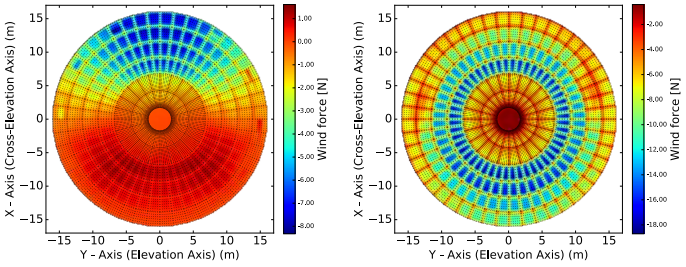

(d) 120° El (e) 180° El

Figure 3.19: Nodal Wind Force on Dish at 13.41 m/s Wind Speed

Figures 3.20a and 3.20b show the total wind forces on the FE model and TIW Drawing respectively on the Ghana 32 m dish calculated at 13.41 m/s wind speed at different wind attack angles. Both plots show similar order of magnitude except at the 60° wind attack angles. The projected area associated with the dish at 60° results in a smaller wind force compared to the dish at the 0° position with maximum dish area.

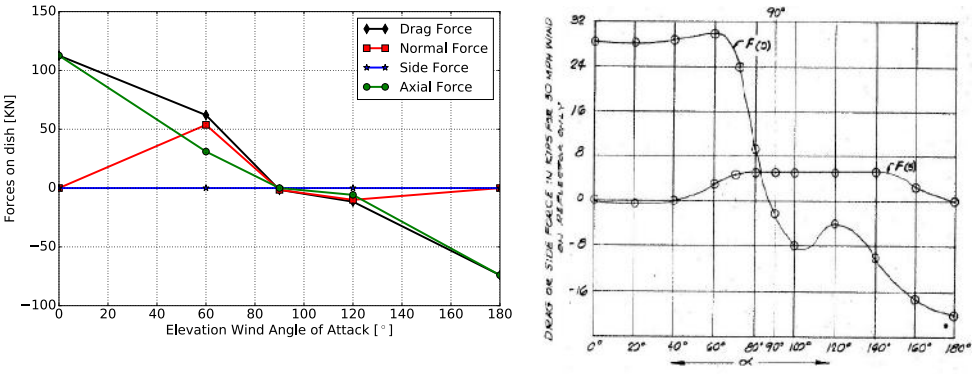

(a) FE Model (b) TIW Data

Figure 3.20: Wind Force Comparison on Dish at Different Wind Attack Angles

3.4.3 Thermal Loading

The thermal loading on the telescope is a function of the position of the sun which results in a temperature variation across the entire structure as some components are subject to heating of the sun while other parts remain at low temperature. The sun passes directly over the telescope because of Ghana's location closer to the equator. Maximum temperature is usually recorded when the sun is directly over the structure. The differential temperature on the FE model is generated by driving a thermal gradient of 8 °C across the entire antenna as reasonably confirmed by a similar approach used in analysing the MeerKAT Dual Offset Antenna by Mutzberg [see 30, Page 46-48]. The thermal load is assumed as a linear temperature profile as shown in the gradient profile plot in figure 3.21.

The MSC Patran Command Language (PCL) built-in spatial field function was used to applied the thermal gradient across the structure of the telescope.

Z	Value
0.	296.14999
3.6803174	297.03888
7.3606348	297.92776
11.040953	298.81668
14.72127	299.70557
18.401587	300.59445
22.081903	301.48334
25.76222	302.37222
29.442537	303.26111
33.122856	304.14999

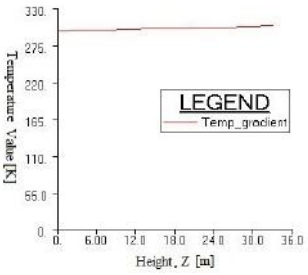

Figure 3.21: Temperature Profile Plot across FE Model [23]

3.5 Operational Conditions and Load Cases

The Ghana Kuntunse 32 m Satellite Earth Station has a tropical savanna climate similar to the closest weather station at the Kotoka International Airport in Accra, Ghana about 29 km away. Figure 3.22 shows the average year temperature and wind speed records from 2008 to 2012 at the Kotoka International Airport weather station. The Kuntunse Earth Station, therefore, assumes the same temperature and wind speed data.

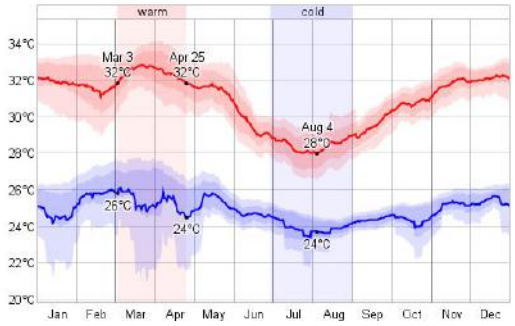

(a) **Temperature**: The daily average high and low temperature represented by red and blue lines respectively

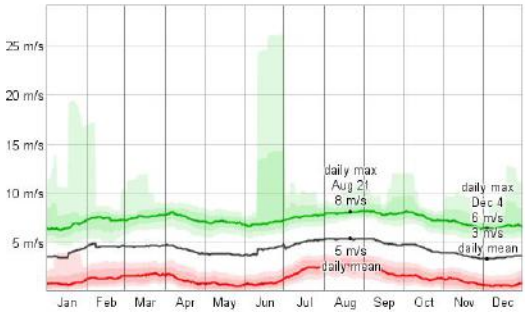

(b) **Wind Speed**: The green, black and red lines respectively represents daily maximum, mean and minimum wind speed

Image: `https://weatherspark.com/averages/28541/Accra-Greater-Accra-Ghana` - accessed on 30/05/2016

Figure 3.22: Average Annual Historical Weather Data

A typical load case is a combination of two or more operating conditions which degrades the telescope pointing performance during a typical science observation. This defines the structural deformation of the radio telescope at any period in time during science observations. Examples of such conditions include: (a) the position of the radio telescope's dish with respect to its elevation/azimuth angle, (b) gravity loading, (c) thermal loading, and (d) wind loading.

The operational conditions under consideration are grouped as:

A. Gravity loading

A1 The radio telescope under its own weight (gravity)

B. Thermal loading

B1 The telescope at 0° elevation/azimuth angle initially with an ambient temperature of 25 °C subjected to a 8 °C thermal gradient from the *top* to the *bottom* across the entire telescope structure as shown in figure 3.24a.

B2 The telescope at 0° elevation/azimuth angle initially with an ambient temperature of 25 °C subjected to a 8 °C thermal gradient from the *left* to the *right* across the entire telescope structure as shown in figure 3.24b.

B3 The telescope at 0° elevation/azimuth angle initially with an ambient temperature of 25 °C subjected to a 8 °C thermal gradient from the *front* to the *back* across the entire telescope structure as shown in figure 3.24c.

B4 The telescope at 90° elevation angle initially with an ambient temperature of 25 °C subjected to a 8 °C thermal gradient from the *top* to the *bottom* across the entire telescope structure as shown in figure 3.24d.

C. Wind Loading

C1 The telescope operating at low wind speed of 3 m/s.

C2 The telescope operating at an average wind speed of 5.556 m/s at site median [11].

C3 The telescope operating at 8.94 m/s [28] high wind speed.

C4 The telescope operating at 13.41 m/s [9] high wind speed.

D. Telescope's elevation axis rotation

D1 Elevation system at a pitch angle of 0°

D2 Elevation system at a pitch angle of 60°

D3 Elevation system at a pitch angle of 90°

E. Telescope's azimuth axis rotation

E1 The telescope at 0° yaw angle about the azimuth axis

E2 The telescope at 180° yaw angle about the azimuth axis

F. Normal mode analysis of the telescope

Considering all possible load combinations results in a very large number of load cases to consider during the analysis. As a result, Appendix B identifies selected load cases used in the FE analysis of the Ghana 32 m radio telescope. These load cases were selected to represent the worst case scenarios that should be tested in the FE environment.

The load cases summarized in table B.1 were selected to evaluate the mechanical pointing performance of the Ghana 32 m radio telescope as grouped below;

- LC1 to LC5 are used to study the effect of gravitational load on the telescope structure without wind and thermal load at different elevation angles.
- LC6 to LC10 consider only the effect of the thermal loading on the telescope rotated through different elevation angles as shown in figure 3.23.
- The telescope's thermal loading effects - as thermal gradients applied vertically, horizontally from left to right, and horizontally from front to the back of the entire structure - are observed in load cases LC6, LC11, LC12, and LC8 as shown in figure 3.24.
- Load cases LC13 to LC17 represent the wind load effect on the telescope at an average wind speed of 5.56 m/s as the telescope is steered through different elevation angles.
- Load cases LC18 to LC22 are used to evaluate the RMS surface error of the Ghana 32 m radio telescope subjected to a wind load of 8.96 m/s to enable comparison with the 26 m diameter JPL antenna [28].
- Load cases LC23, LC14, LC19 and LC24 examine the different wind speed loads on the telescope at 60° elevation angle and 0° azimuth angle.
- A typical operating condition at an average wind speed of 5.56 m/s with 8 °C thermal gradient applied vertically on the entire structure, from an ambient temperature of 23 °C, includes the combined effect of gravity, wind, and thermal loading as the telescope is steered through different elevation angles. This is studied in load cases LC25 to LC29.
- Finally, LC30 studies the modal analysis of the numerical model at 0° elevation angle.

The deformation fields of all load cases are exported to an external program for further post-processing discussed in the next chapter. Figure 3.25 shows the telescope's deformation under combined load cases LC25 to LC29 in a

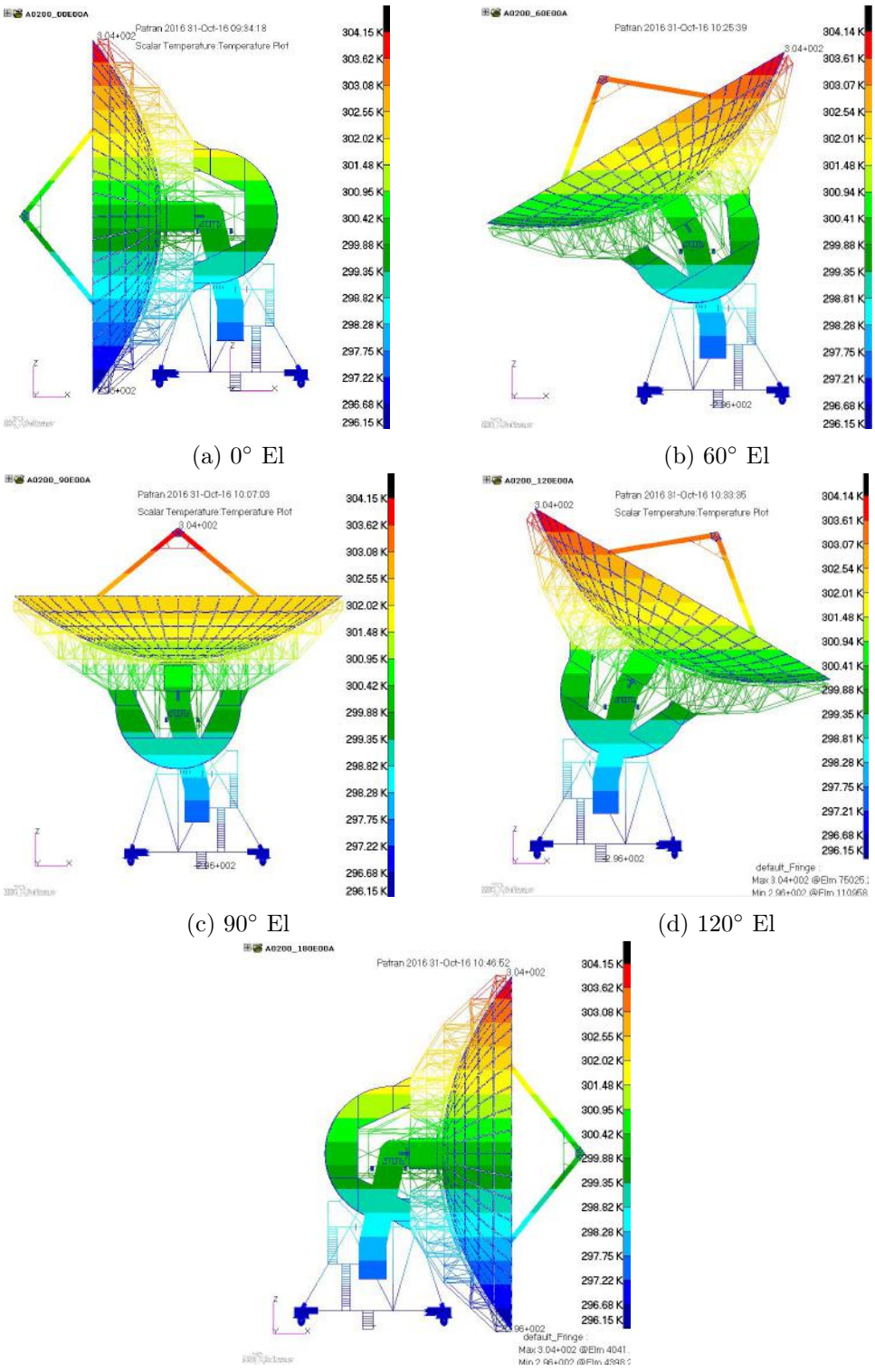

(a) 0° El

(b) 60° El

(c) 90° El

(d) 120° El

(e) 180° El

Figure 3.23: Thermal Loading at Different Elevation Angles

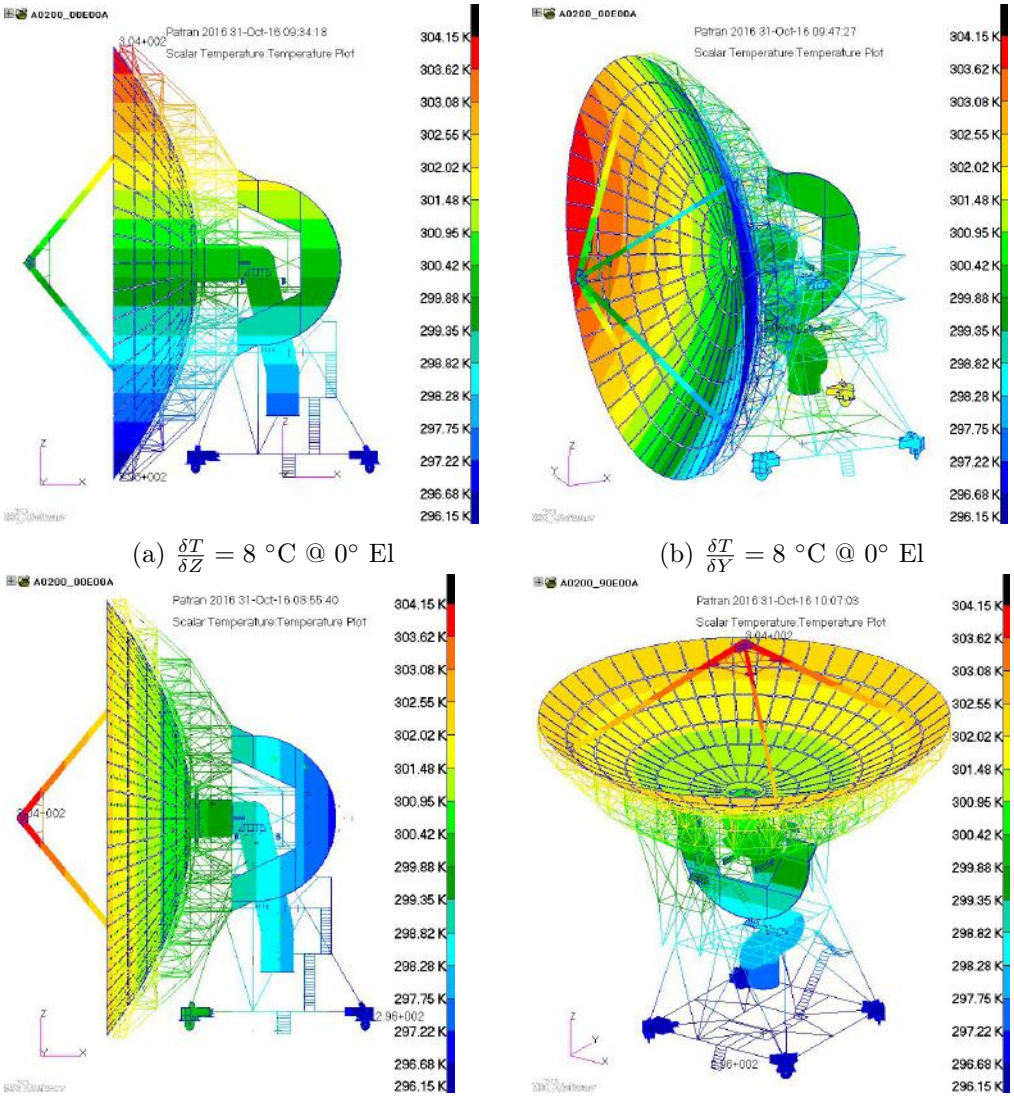

(a) $\frac{\delta T}{\delta Z} = 8$ °C @ 0° El

(b) $\frac{\delta T}{\delta Y} = 8$ °C @ 0° El

(c) $\frac{\delta T}{\delta X} = 8$ °C @ 0° El

(d) $\frac{\delta T}{\delta X} = 8$ °C @ 90° El

Figure 3.24: Contour Plot of Thermal Gradients Across Telescope

typical average operating condition. The quadrupod leg assembly registered the highest displacement in all load cases with maximum overall deformation at the 180° wind angle of attack position (convex side of dish facing upstream wind as shown in figure 3.25e).

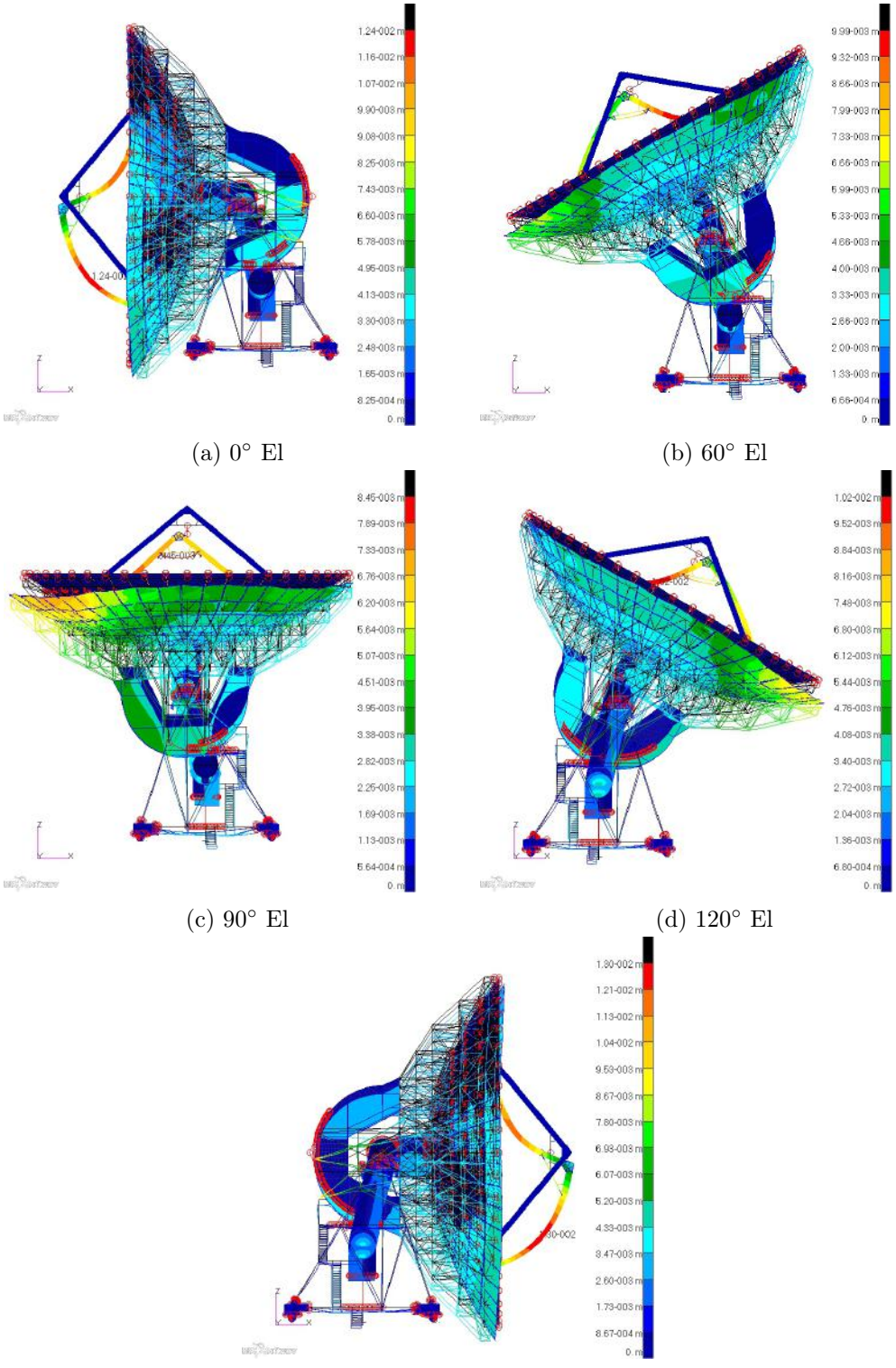

(a) 0° El

(b) 60° El

(c) 90° El

(d) 120° El

(e) 180° El

Figure 3.25: Deformation Fringe Plot of Telescope under Combined Loads

Figure 3.26 and 3.27 show the load cases under gravity, wind, thermal, and also a combination of the three loads at 60° elevation angle. The deformation field on both the overall telescope and the primary dish shows gravity loading as the most dominant load case at 60° elevation angle during an average site operating condition.

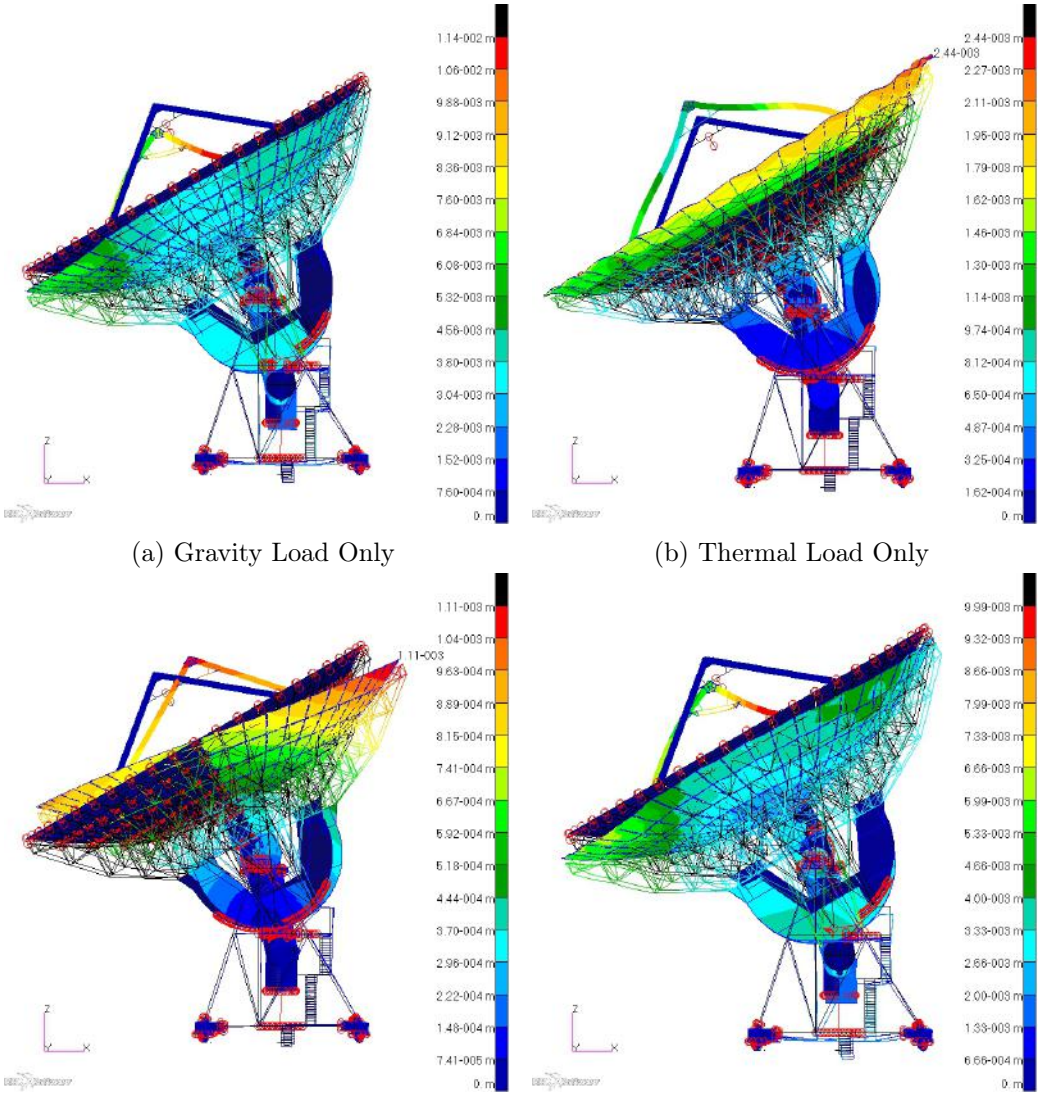

(a) Gravity Load Only

(b) Thermal Load Only

(c) Wind Load Only

(d) Combined Load

Figure 3.26: Deformation Plot at 60° Elevation Angle on Telescope - display the overall telescope deformation

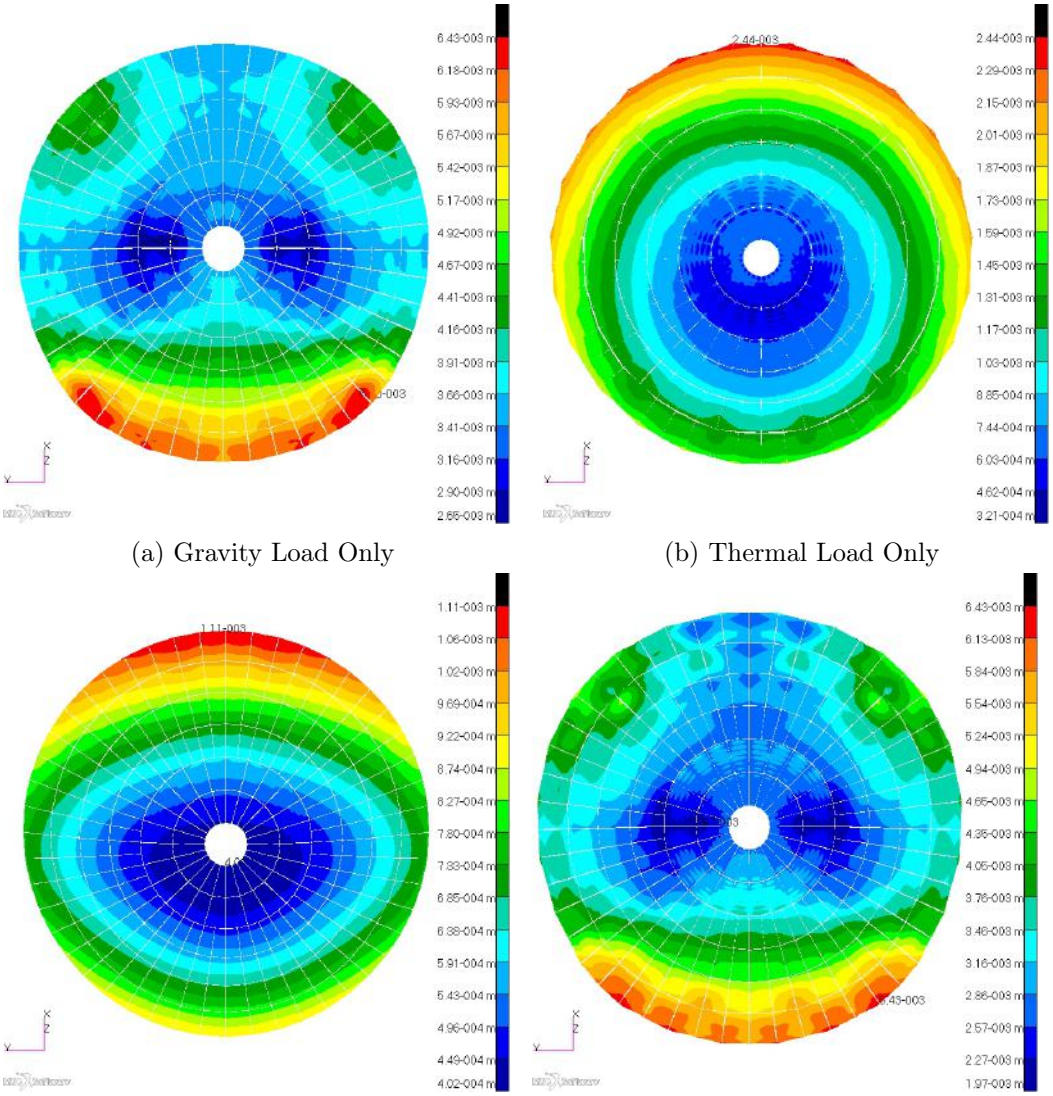

(a) Gravity Load Only

(b) Thermal Load Only

(c) Wind Load Only

(d) Combined Load

Figure 3.27: Deformation Plot at 60° Elevation Angle on Dish Surface - display the primary reflector deformation field

The combined dish deformation field as shown in figure 3.27d is obtained by adding the individual contributions from each load condition. The deformation plot references the global frame system discussed in figure 3.1 and table 3.1. The deformation plots of the dish surface with calculated RMS surface and pointing errors for all twenty-nine load cases are presented in Appendix C.

The results of load case LC30 as shown in figure 3.29 presents the first ten natural mode shapes of the Ghana 32 m telescope.

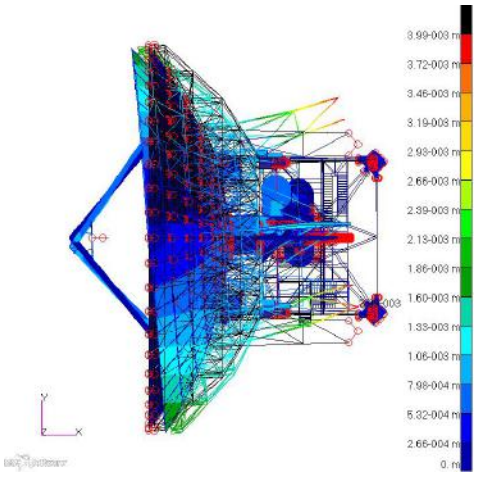

(a) Mode 1 (2.19 Hz)

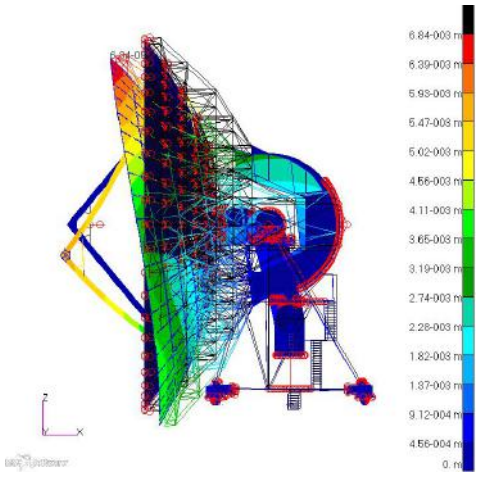

(b) Mode 2 (2.38 Hz)

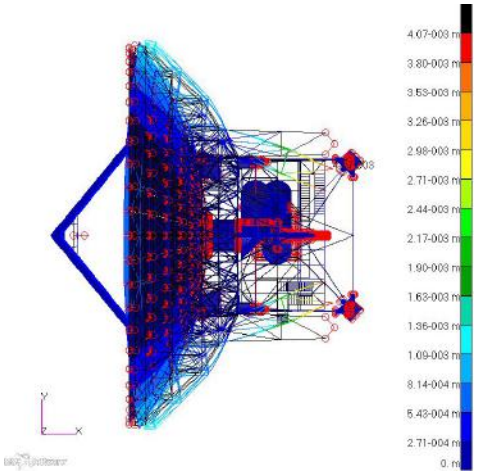

(c) Mode 3 (2.77 Hz)

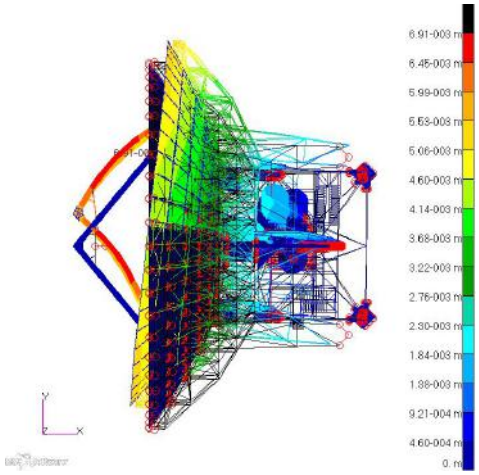

(d) Mode 4 (3.02 Hz)

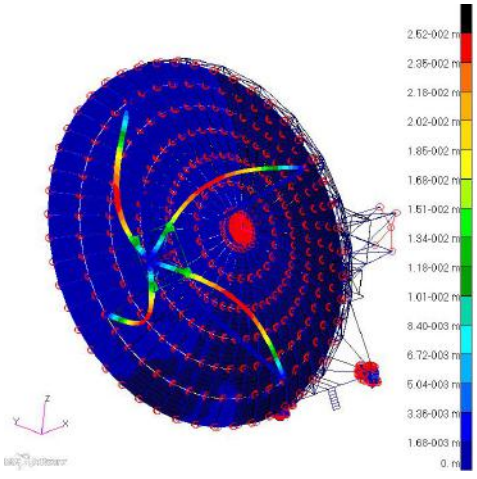

(e) Mode 5 (3.75 Hz)

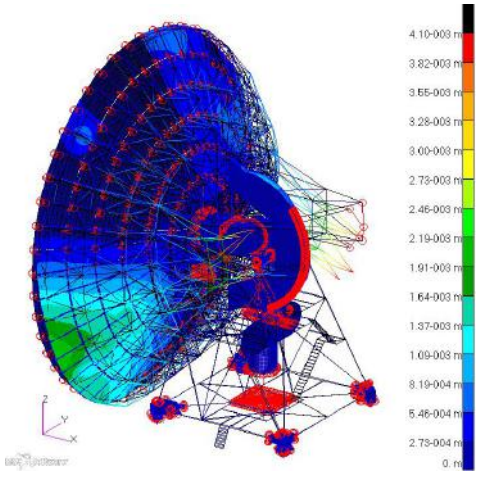

(f) Mode 6 (4.91 Hz)

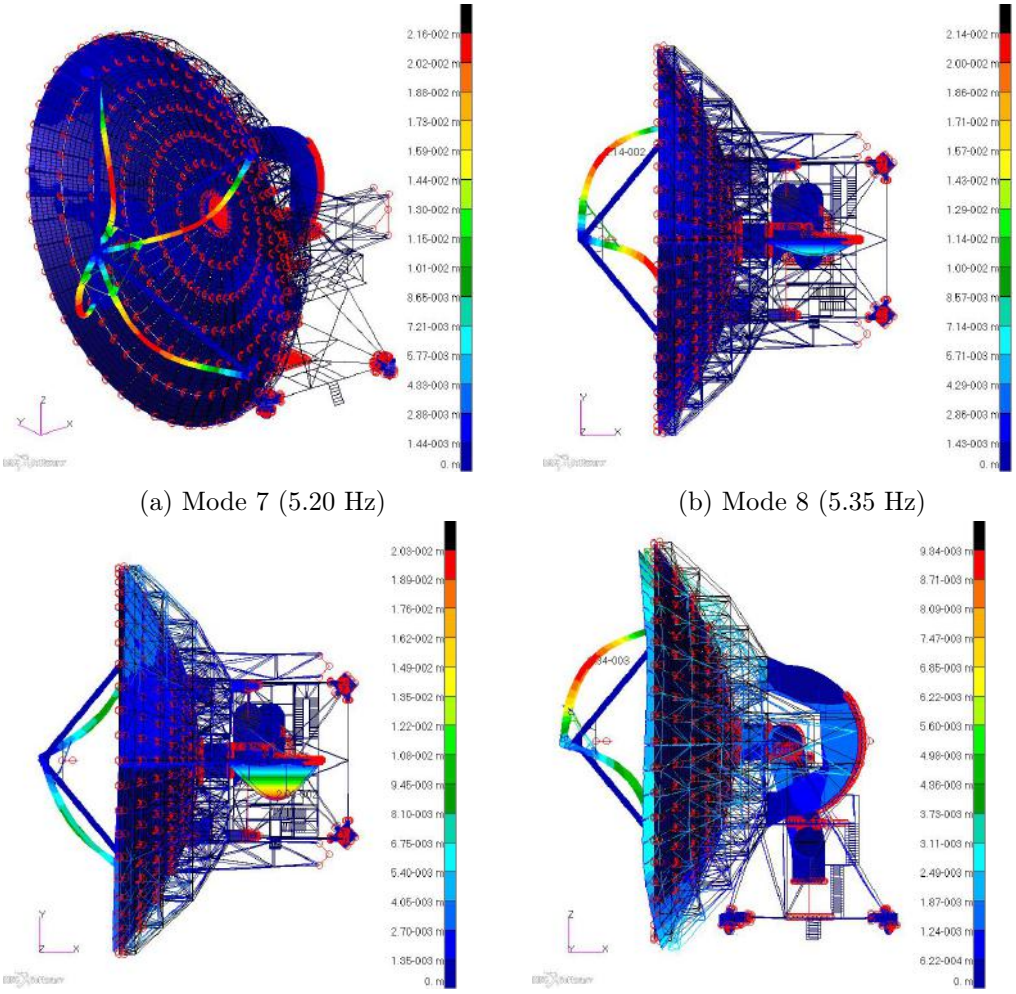

(a) Mode 7 (5.20 Hz)

(b) Mode 8 (5.35 Hz)

(c) Mode 9 (5.55 Hz)

(d) Mode 10 (5.61 Hz)

Figure 3.29: First Ten Natural Modes of Ghana 32 m Radio Telescope's Model at 0° elevation/azimuth angle

Chapter 4

Error Analysis

In the ideal state, a radio telescope's beam axis (or focal axis) directly coincides with the direction vector of the commanded control system input during either pointing or tracking of a celestial source(s). In reality, however, the specified pointing vector is corrupted by atmospheric RF refraction, control system errors, receiver errors and mechanical errors. It is therefore necessary to implement a good mathematical pointing model that quantifies these imperfections and corrects the errors through control system inputs.

The main contributors for the mechanical errors include the telescope's structural deformations, manufacturing alignment errors, and servo drive train errors. The structural deformation is mainly influenced by the gravity, wind and thermal loading, and is a major contributor to the pointing error of a radio telescope. The FE analysis results provide information on how the telescope structural deformation changes the shape, position, and orientation of its paraboloid reflector.

The FE analysis results, however, are corrupted by the rigid body motion of the entire dish surface mainly due to the deformation of the supporting alidade structure. This chapter captures how the noise in the FE output results is eliminated by further post-processing of the data using an external program routine (written in Python) for determining the telescope's surface errors and pointing direction.

4.1 Least Square Data Fitting

The telescope's reflector deformation field as obtained from the FE analysis complicates the error data interpretation. In most parabolic telescopic designs, it is a common approach to first eliminate the rigid body motion from the FE deformation field, before fitting an idealised paraboloid through the nodal displacement data. The pointing vector obtained from the fitted paraboloid

beam axis then defines the pointing direction of the radio telescope under structural deformation.

The rigid body motion is first quantified and eliminated by adding a series of Zernike polynomials. Genberg [31] presented how the Zernike polynomials are implemented with derived quantities useful for further data analysis and interpretation of the reflector surface properties as discussed in section 4.1.1.

4.1.1 Zernike Polynomials

The Zernike polynomials are often used by optical engineers to capture reflector surface defects into quantifiable terms that add meaning to the data clusters obtained. The generalised Zernike polynomial, Z_p expressed in a rectangular Cartesian coordinate system, can be written as equation 4.1.1 [31].

$$Z_p(x, y) = \sum_{j=1}^{m} C_j \phi_j \tag{4.1.1}$$

where ϕ, C, and m represent the Zernike term, Zernike term's coefficient, and the number of polynomial terms respectively. The first few Zernike polynomial terms include;

Bias or Piston	C_1
X and Y Tilt	$C_2x \ + \ C_3y$
Focus	$C_4(2r^2 - 1)$
Primary Astigmatism	$C_5 2xy \ + \ C_6(x^2 - y^2)$
Primary Coma	$(C_7y + C_8x)(3r^2 - 2)$
Primary Spherical	$C_9(6r^4 - 6r^2 + 1)$
Secondary Spherical	$C_{10}(20r^6 - 30r^4 + 12r^2 - 1)$
	+ higher order terms
where $r^2 = x^2 + y^2$	

The rigid body motions are described by the first three terms, bias (C_1) and tilts (C_2 and C_3). This quantifies the translation of the dish along its focal (Z-) axis and the rotations about the X- and Y-axes which represent rigid body motions in the FE model deformation data. The remaining higher order terms account for aberrations normally used in optics but not needed in this study.

For each node point on the reflector surface, the Zernike polynomial is rewritten

as equation 4.1.2:

$$\begin{aligned} Z_{p_i} &= \sum_{j=1}^{m} C_j \phi(x_i, y_i) \\ &= \sum_{j=1}^{m} C_j \phi_j^i \end{aligned} \tag{4.1.2}$$

The least square error E is given by equation 4.1.3:

$$\begin{aligned} E &= \sum_{i=1}^{n} W_i [U_i - Z_i]^2 \\ &= \sum_{i=1}^{n} W_i [U_i - \sum_{j=1}^{m} C_j \phi_j^i]^2 \end{aligned} \tag{4.1.3}$$

where U_i is the nodal displacements on the reflector surface and W_i is the weighing factor associated with each grid (can be obtained from equation 3.4.2).

The least square errors are minimised by differentiating with respect to the coefficients and setting the first derivative to zero as illustrated in equation 4.1.4:

$$\begin{aligned} \frac{\partial E}{\partial C_k} &= 2 \sum_{i=1}^{n} W_i [U_i - \sum_{j=1}^{m} C_j \phi_j^i] \phi_k^i \\ &= 2 \sum_{i=1}^{n} W_i U_i \phi_k^i - 2 \sum_{i=1}^{n} \sum_{j=1}^{m} W_i C_j \phi_j^i \phi_k^i \\ &= 0 \end{aligned} \tag{4.1.4}$$

Assigning, $F_k = 2 \sum_{i=1}^{n} W_i U_i \phi_k^i$ and $H_{jk} = 2 \sum_{i=1}^{n} \sum_{j=1}^{m} W_i \phi_j^i \phi_k^i$ and rearranging in matrix form, the least square problem is formulated by equation 4.1.5.

$$[H_{jk}] \{C_j\} = \{F_k\}$$

$$2 \begin{bmatrix} W_1.[1 & x_1 & y_1].[1 + x_1 + y_1] \\ W_2.[1 & x_2 & y_2].[1 + x_2 + y_2] \\ W_3.[1 & x_3 & y_3].[1 + x_3 + y_3] \\ W_4.[1 & x_4 & y_4].[1 + x_4 + y_4] \\ \vdots & \vdots & \vdots \\ W_n.[1 & x_n & y_n].[1 + x_n + y_n] \end{bmatrix} \begin{bmatrix} C_1 \\ C_2 \\ C_3 \end{bmatrix} = 2 \begin{bmatrix} W_1.U_1.[1 + x_1 + y_1] \\ W_2.U_2.[1 + x_2 + y_2] \\ W_3.U_3.[1 + x_3 + y_3] \\ W_4.U_4.[1 + x_4 + y_4] \\ \vdots \\ W_n.U_n.[1 + x_n + y_n] \end{bmatrix} \tag{4.1.5}$$

where n is the number of grid points (11,496 nodes for the Ghana 32 m dish FE model) and ϕ_k is the Zernike polynomial derivative with respect to its coefficients.

4.1.2 Homogeneous Transformation Matrix

The homogeneous transformation matrix commonly used in robotics and the aerospace industry, combines both the translation and rotation of an object into a single matrix. This provides a convenient means of eliminating the rigid body motion in the FE data using the translation and rotations quantified by the Zernike polynomials.

Considering a yaw about the Z-axis ($R_{z,\varphi}$), a pitch about the Y-axis ($R_{y,\theta}$), and a roll about X-axis ($R_{x,\psi}$) with respect to a fixed reference frame as shown in figure 4.1. The rotational transformation matrix, R_{xyz} is then given by equation 4.1.6.

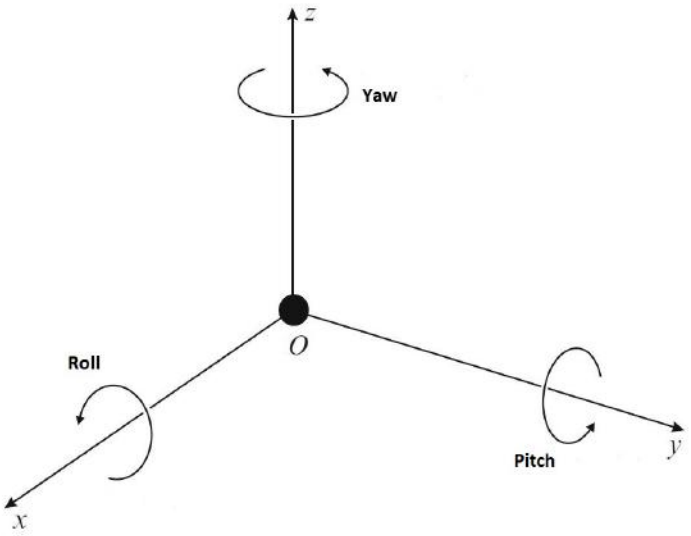

Figure 4.1: Right-Hand Rectangular Reference Frame

$$
\begin{aligned}
R_{xyz} &= R_{z,\varphi}\ R_{y,\theta}\ R_{x,\psi} \\
&= \begin{bmatrix} C_\varphi & -S_\varphi & 0 \\ S_\varphi & C_\varphi & 0 \\ 0 & 0 & 1 \end{bmatrix} \begin{bmatrix} C_\theta & 0 & S_\theta \\ 0 & 1 & 0 \\ -S_\theta & 0 & C_\theta \end{bmatrix} \begin{bmatrix} 1 & 0 & 0 \\ 0 & C_\psi & -S_\psi \\ 0 & S_\psi & C_\psi \end{bmatrix} \\
&= \begin{bmatrix} C_\varphi C_\theta & -S_\varphi C_\psi + C_\varphi S_\theta S_\psi & S_\varphi S_\psi + C_\varphi S_\theta C_\psi \\ S_\varphi C_\theta & C_\varphi C_\psi + S_\varphi S_\theta S_\psi & -C_\varphi S_\psi + S_\varphi S_\theta S_\psi \\ -S_\theta & C_\theta S_\psi & C_\theta C_\psi \end{bmatrix}
\end{aligned} \tag{4.1.6}
$$

where C and S represent the cosine and sine functions respectively and φ, θ, and ψ are the yaw, pitch, and roll angles respectively.

The translation vector, T_{xyz} of the moving frame from a fixed reference frame

is given by equation 4.1.7.

$$T_{xyz} = \begin{bmatrix} T_x \\ T_y \\ T_z \end{bmatrix} \tag{4.1.7}$$

The homogeneous transformation matrix, HT combines equation 4.1.6 and equation 4.1.7 into a single matrix as equation 4.1.8:

$$\begin{aligned} HT &= \begin{bmatrix} R_{xyz} & T_{xyz} \\ 0 & 1 \end{bmatrix} \\ &= \begin{bmatrix} C_\varphi C_\theta & -S_\varphi C_\psi + C_\varphi S_\theta S_\psi & S_\varphi S_\psi + C_\varphi S_\theta C_\psi & T_x \\ S_\varphi C_\theta & C_\varphi C_\psi + S_\varphi S_\theta S_\psi & -C_\varphi S_\psi + S_\varphi S_\theta S_\psi & T_y \\ -S_\theta & C_\theta S_\psi & C_\theta C_\psi & T_z \\ 0 & 0 & 0 & 1 \end{bmatrix} \end{aligned} \tag{4.1.8}$$

and the corresponding homogeneous representation of the nodal grid position coordinate to be transformed is written as;

$$\begin{bmatrix} x_i \\ y_i \\ z_i \\ 1 \end{bmatrix}$$

The bias or Z-translation (C_1), X-tilt ($\arctan(C_2)$), and the Y-tilt ($\arctan(C_3)$) make the translation and rotation parameters components of the homogeneous transformation matrix to get rid of the rigid body motion. An idealised paraboloid is then fitted through the resulting data, and finally the RMS surface and pointing errors are calculated.

4.2 Surface Accuracy

The deformation of the reflector surface introduces surface errors which become significant and reduce the overall antenna gain. The antenna gain traces how well radio emissions from the distant source are converted into electrical power. The surface error is even worse with increasing reflector size and at higher frequencies. The surface errors of the telescope's reflector, also known as surface roughness are described as the deviation of the telescope's surface from the idealised paraboloidal surface due to the structural deformation of the telescope.

The numerical measure of the surface error, σ_i, associated with each node on the dish surface is the difference between the undeformed nodal focal distance, $\mathrm{uf_d}^i$ and the best fit paraboloid nodal focal distance, $\mathrm{ff_d}^i$ as illustrated in figure 4.2 and expressed by equation 4.2.1.

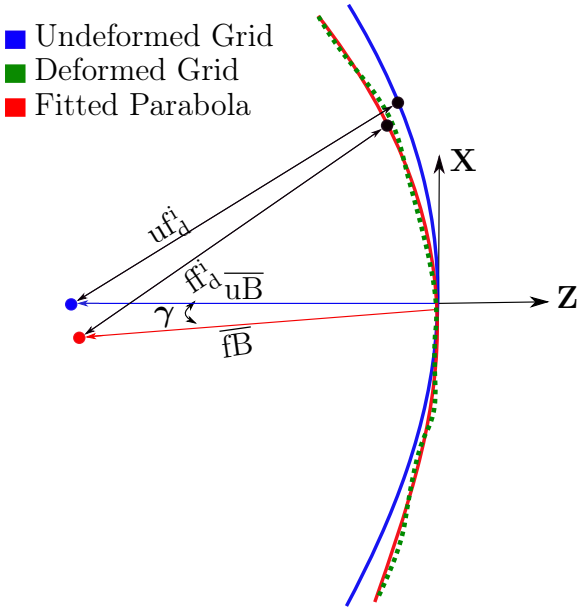

Figure 4.2: Dish Surface Errors (Image adapted from Joubert [32])

$$\sigma_i = {uf_d}^i - {ff_d}^i \tag{4.2.1}$$

The reflector surface accuracy, σ_{rms} is the root-mean-square value of the surface errors or roughness defined in equation 4.2.1, and can be written as equation 4.2.2.

$$\sigma_{rms} = \sqrt{\frac{\sum_{i=1}^{n} \sigma_i^2 . A_i}{\sum_{i=1}^{n} A_i}} \tag{4.2.2}$$

where i, n and A_i are the grid node, the total number of grid nodes, and the surface area per grid node (see equation 3.4.2, calculated as the weighing factor per grid).

4.3 Pointing Error

The pointing error, γ, resulting from the telescope's structural deformation is the quantitative measure of the angular offset between the undeformed beam axis and the fitted paraboloid beam axis as illustrated in figure 4.2. It is also known as the "tracking error" during tracking of celestial sources and is calculated using equation 4.3.1.

$$\gamma = \cos^{-1}\left(\frac{\overline{\mathrm{uB}}.\overline{\mathrm{fB}}}{||\overline{\mathrm{uB}}||.||\overline{\mathrm{fB}}||}\right) \tag{4.3.1}$$

The pointing accuracy, γ_{rms}, is the root-mean-square value of the pointing errors for a given sets of load cases, and is evaluated from equation 4.3.2.

$$\gamma_{rms} = \sqrt{\frac{\sum_{l=1}^{t} \gamma_i^2}{t}} \tag{4.3.2}$$

where l and t are the load case and the total number of load cases respectively under investigation.

The required surface and pointing accuracy for the Ghana 32 m telescope for optimal performance as a radio astronomy instrument were discussed in section 2.5.1.

4.4 External Program

A Python program routine was developed to implement the numerical solution for the Ghana 32 m radio telescope's surface accuracy and pointing errors. Figure 4.3 shows the external scripts coupled to the FE model.

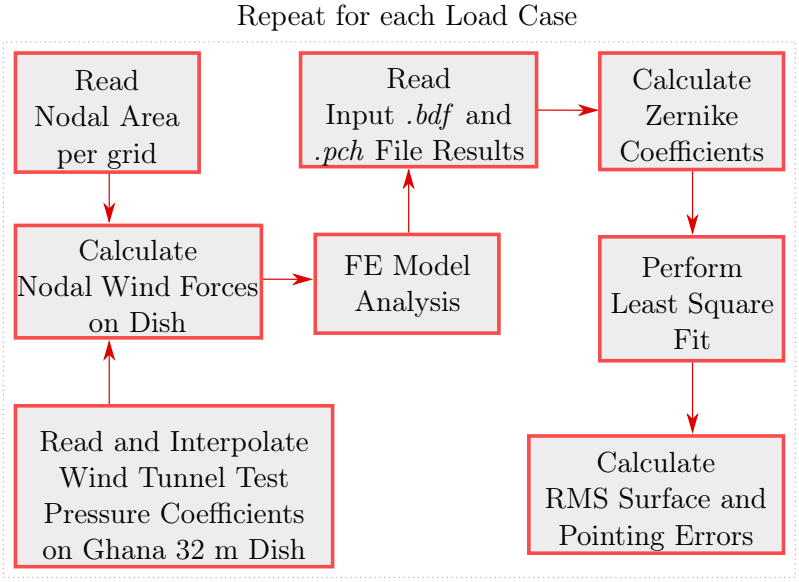

Figure 4.3: External Program Coupled with FE Analysis

4.5 Simulated Results

The wind loading results for the Ghana 32 m telescope were compared with the JPL 26 m antenna presented by Kron [28] as shown in table 4.1 and figure 4.4 for similar wind angles of attack on the telescope's dish.

Table 4.1: Ghana 32 m and JPL 26 m Dish Surface Accuracy Comparison

	Wind Attack Angle, β				
	0° (LC18)	60° (LC19)	90° (LC20)	120° (LC21)	180° (LC22)
JPL 26 m Dish [28] [mm]	0.1448	0.2946	0.0635	0.2387	0.0864
	0.3449*	0.7018*	0.1513*	0.5686*	0.2058*
Ghana 32 m Dish [mm]	0.5800	1.0321	0.0330	0.0912	0.5075
	0.4490*	0.7999*	0.0255*	0.0706*	0.3929*

*Normalized Values

The RMS surface errors from both dishes show similar trends. The worse case RMS surface error occurred at 60° wind attack position for both the JPL 26 m and the Ghana 32 m dish. Also, both dishes have their least RMS error at the 90° wind attack positions. The difference in values may be attributed to the reflector's backup structure topography and the subtle difference in their focal to diameter ratio.

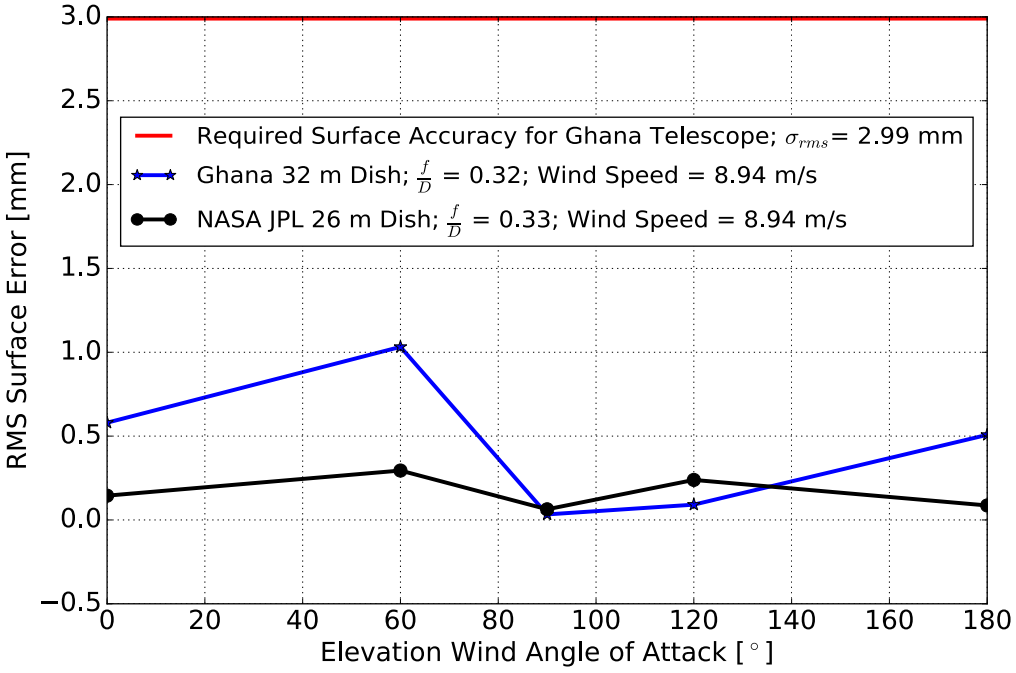

Figure 4.4: JPL 26 m and Ghana 32 m Dish Surface Accuracy Comparison

Table 4.2 shows the effect of gravity, thermal, wind, and combined loading on the RMS surface accuracy of the Ghana 32 m radio telescope for the different elevation angles. The thermal load cases considered the sun directly over the radio telescope inducing a vertical 8 °C thermal gradient through the entire structure for the different elevation angles. A wind load at 5.56 m/s average wind speed was implemented. The 120° and 180° elevation angles represent the telescope at 60° and 0° elevation angles rotated through 180° azimuth angle respectively for the load cases as shown in figure 4.5. The gravity and thermal load cases show symmetry about the 90° elevation with an accuracy difference in the order of 1.0 x 10^{-12} between the 0° and 180° elevation angles, and also that between the 60° and 120° elevation angles. All load cases fall within the acceptable margin of surface accuracy required for the first phase of science observations.

Table 4.2: Surface Accuracy of the Ghana 32 m Radio Telescope

Load Cases	**Reflector Dish Orientation**				
	0° El/Az	60° El/ 0° Az	90° El/ 0° Az	60° El/ 180° Az	0° El/ 180° Az
Gravity Load LC1-LC5 [mm]	0.506	0.767	0.929	0.767	0.506
Thermal Load LC6-LC10 [mm]	0.305	0.203	0.133	0.203	0.305
Wind Load LC13-LC17 [mm]	0.224	0.398	0.013	0.035	0.195
Combined Load LC25-LC29 [mm]	0.536	0.727	1.011	0.883	0.660

El - Dish Elevation Angle Az - Telescope Azimuth Angle

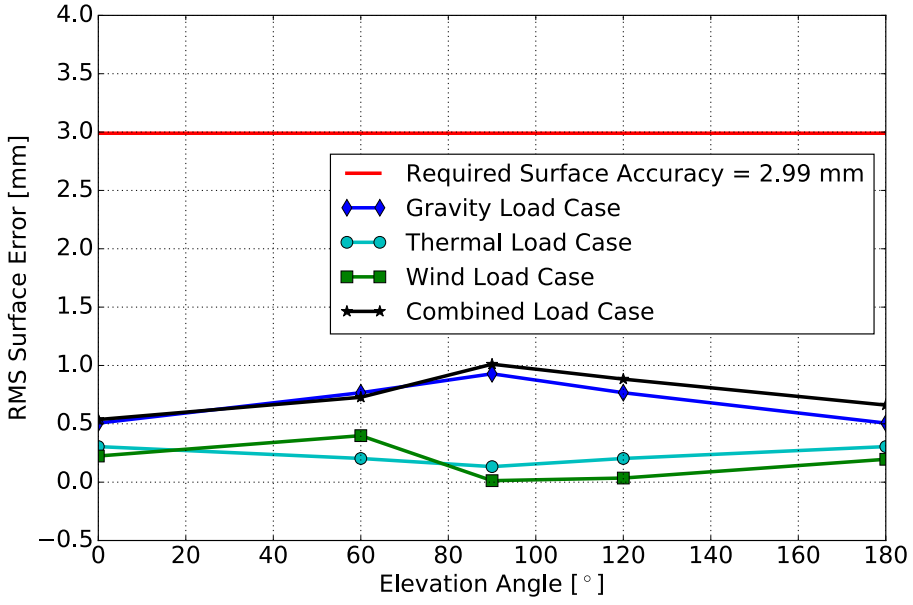

Figure 4.5: Plot of Ghana 32 m Telescope Surface Accuracy

The associated telescope's pointing errors for the same gravity, wind, thermal, and combined load cases are presented in table 4.3 and figure 4.6. Similar to the RMS surface error plot, the pointing errors shows symmetry for the gravity and thermal wind load case. All load cases fall within the required pointing accuracy value for the Ghana 32 m radio telescope and will be integrated into the pointing model once validated with photogrammetry or microwave holography surface measurements to account for structural deformation pointing errors.

Table 4.3: Pointing Error of the Ghana 32 m Radio Telescope due to Structural Deformation

Load Cases	**Reflector Dish Orientation**				
	0° El/Az	60° El/ 0° Az	90° El/ 0° Az	60° El/ 180° Az	0° El/ 180° Az
Gravity Load LC1-LC5 [°]	0.0016	0.0027	0.0040	0.0027	0.0016
	5.76"	9.72"	14.4"	9.72"	5.76"
Thermal Load LC6-LC10 [°]	0.0021	0.0013	0.0006	0.0013	0.0021
	7.56"	4.68"	2.16"	4.68"	7.56"
Wind Load LC13-LC17 [°]	0.0016	0.0027	0.0001	0.0002	0.0014
	5.76"	9.72"	0.36"	0.72"	5.04"
Combined Load LC25-LC29 [°]	0.0019	0.0014	0.0047	0.0042	0.0045
	6.84"	5.04"	16.92"	15.12"	16.2"

El - Dish Elevation Angle Az - Telescope Azimuth Angle

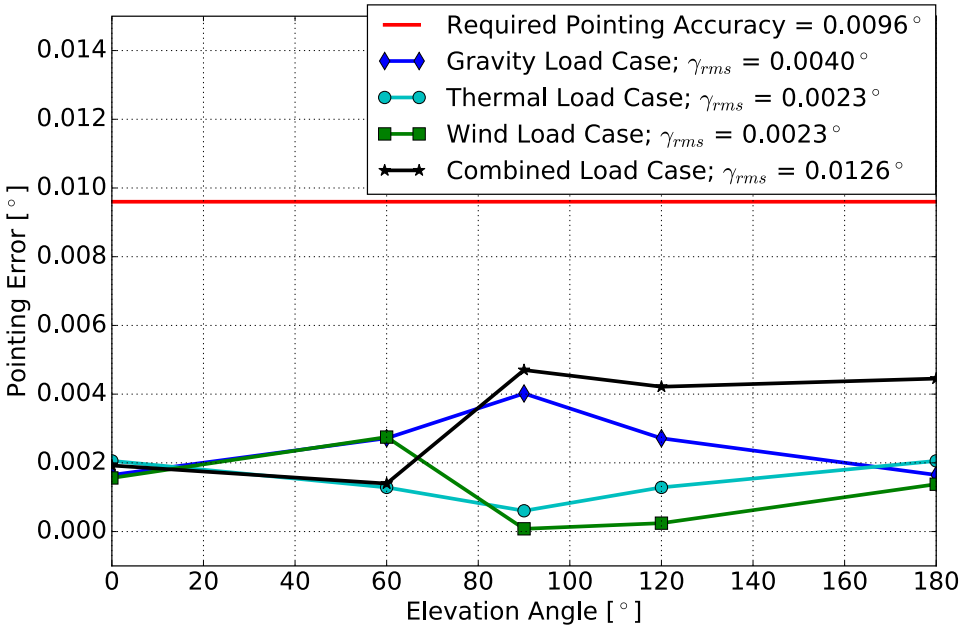

Figure 4.6: Plot of Ghana 32 m Telescope's Pointing Errors induced by structural deformation

The effect of the thermal loading on the Ghana 32 m radio telescope's surface accuracy and pointing errors was investigated for the different thermal gradient application illustrated in figure 4.7. The output results are shown in table 4.4. The worst case RMS surface error for this load case set was registered at 0.658 mm with the telescope at 0° elevation angle with 8 °C thermal gradient applied horizontally from the front of the concave side of the telescope to the back. All the load cases fall within the required RMS surface and pointing error values of the telescope.

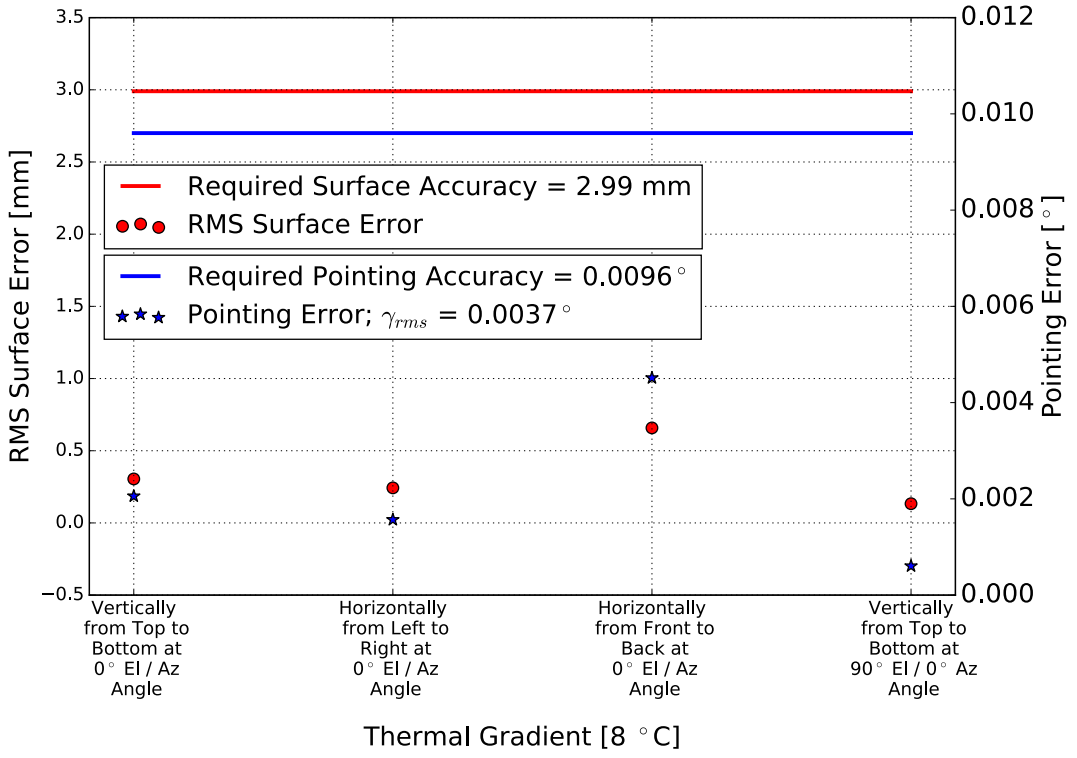

Figure 4.7: Thermal Load Applied on Telescope from Different Directions

Table 4.4: Thermal Load on Telescope from Different Positions

Error	**Reflector Dish Orientation**			
	0° El/Az (LC6)	0° El/Az (LC11)	0° El/Az (LC12)	90° El/ 0° Az (LC8)
RMS Surface Accuracy [mm]	0.305	0.243	0.658	0.133
Pointing Error [°]	0.0021	0.0016	0.0045	0.0006

El - Dish Elevation Angle Az - Telescope Azimuth Angle

Finally, the wind load on the Ghana 32 m radio telescope at 60° elevation angle and 0° azimuth angle is varied to study its effect on the telescope's RMS surface and pointing error as shown in table 4.5 and figure 4.8. A gradual increase in both the RMS surface and pointing errors was recorded for these load cases, peaking at 2.322 mm and 0.0160° respectively at 13.41 m/s. The surface accuracy and pointing error exceed the allowable margin beyond the 8.94 m/s wind speed value. Science observation will rarely take place beyond this range since the annual average maximum wind speed record is about 8 m/s wind speed at the site as shown in figure 3.22b.

Table 4.5: Wind Load on Telescope at Varying Wind Speed

Error	**Wind Speed on Telescope at 60° El/ 0° Az**			
	3 m/s (LC23)	5.56 m/s (LC14)	8.94 m/s (LC19)	13.41 m/s (LC24)
RMS Surface Accuracy [mm]	0.116	0.398	1.032	2.322
Pointing Error [°]	0.0008	0.0027	0.0071	0.0160

El - Dish Elevation Angle Az - Telescope Azimuth Angle

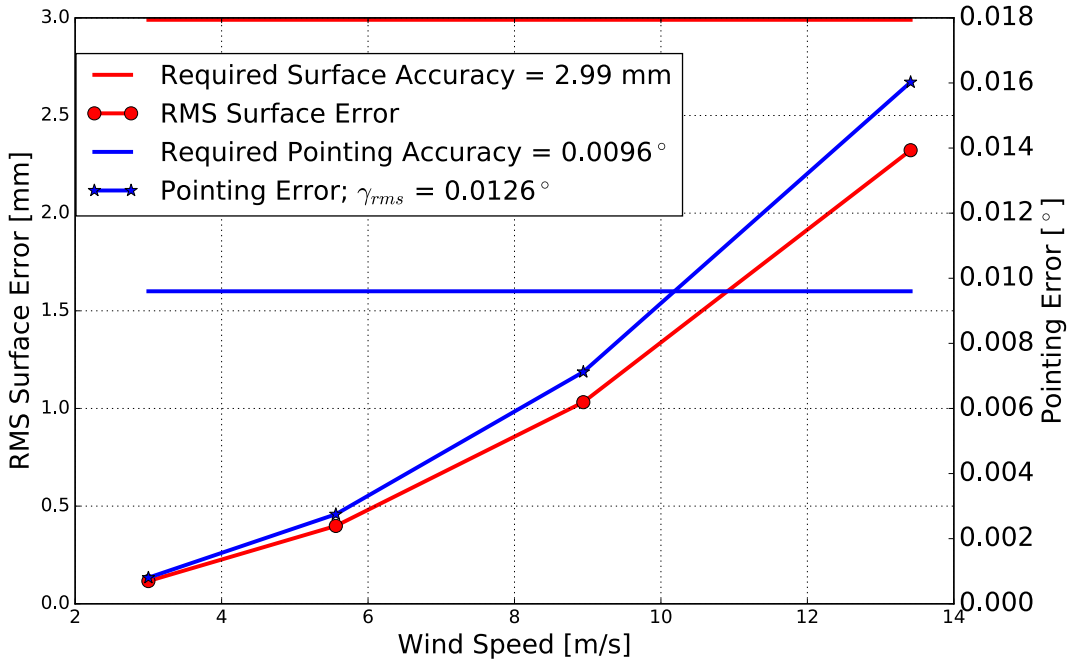

Figure 4.8: Telescope at 60° subject to Varying Wind Load

Chapter 5

Experimental Data

The Ghana 32 m telecommunication dish at Kuntunse is currently under conversion into a radio astronomy telescope as part of the AVN project. The technique used by the original manufacturer of the antenna, GD SATCOM, to measure the surface roughness of the dish was the theodolite and tape method after the initial installation. The measured error data was then used to reset the panel's misalignment to the theoretical paraboloid values. This error data is evaluated and compared with the simulated results of the Ghana 32 m diameter radio telescope's numerical model. The AVN plans to use one of the modern surface measurement techniques to acquire the current surface errors of the Ghana 32 m diameter dish surface, which can be used for future comparison with the results of the numerical model presented here.

This chapter introduces the various surface measurement techniques used in evaluating the surface roughness of radio astronomy telescopes, and feasible options for the AVN Ghana 32 m telescope.

5.1 Reflector Measurement Techniques

The three main techniques which are widely used for measuring radio telescope reflector surface errors are, (a) microwave holography, (b) laser scanning, and (c) photogrammetry. A fourth method, the theodolite and tape measuring technique as initially used in adjusting the Ghana 32 m diameter panels, also exists. The results from this method are further discussed in section 5.2.

Microwave holography uses a radio measuring technique which is based on antenna theory. The shape of the primary reflector surface is derived from the amplitude and phase of the antenna beam measured from a strong radio signal in the far-field of the antenna. Holography is establishing itself as a radio astronomy measurement technique at high observing frequencies as described by Baars *et al.* [33] and Hunter *et al.* [34]. A reference antenna is

required to observe the source in parallel with the antenna to be measured. Cosmic sources are usually faint, and therefore would require a large aperture reference antenna for the measurement. An alternative to the cosmic source is to use a powerful artificial source such as a satellite transmission beacon usually with high-cost implications. Holography also requires compensation for the secondary reflector and quadrupod assembly diffraction. This makes holography not too appealing as a surface measurement technique for the AVN Ghana 32 m radio telescope. With access to setup tools and equipment, the holography measuring technique remains one of the most accurate techniques but requires highly skilled professionals in manning the experiment compared to the other methods.

The laser scanning and photogrammetry techniques are optical methods which use visible light to measure positions on the reflector surface to millimetre accuracy. Sarti *et al.* [35] describe how the laser scanning technique was implemented in measuring both the surface errors of the 32 m Medicina and Noto radio telescopes. A GS200 Trimble-Mensi LS was used to obtain the measurements of the surface deviations of the primary reflector from two opposite positions around the dish vertex at different elevation angles. Figure 5.1 shows the instrument mounted on the Noto telescope. The disadvantages of the instrument are that it cannot account for the deformation around the aperture support where it is mounted, easily loses calibration when tipped during measurement, and that the process is slow for a denser sample rate. The operation of the laser scanner requires a moderately skilled operator with high instrument cost.

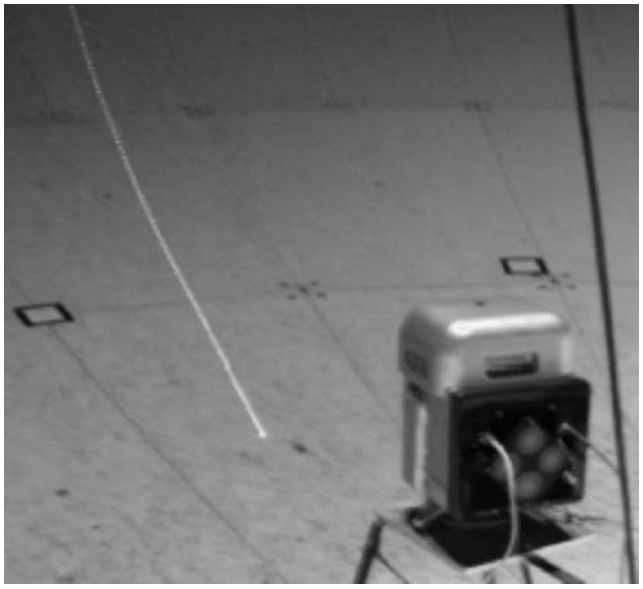

Figure 5.1: GS200 Trimble-Mensi LS on Noto Telescope [35]

In the photogrammetry measurement technique, images of the dish surface are taken from different perspective angles which are then reconstructed to obtain the surface contour of the dish surface. Reflective targets are placed on the dish surface to improve the accuracy of the measurements with pictures usually acquired at night. The photographs can be taken from different possible aerial platforms such as: (a) unmanned aerial vehicle (UAV) or drone, (b) manned aerial vehicle (e.g plane or helicopter), (c) balloons (either manned or unmanned), (d) crane, or (e) kite. The proximity required for photographs, associated cost and risk make the manned aerial vehicle an unattractive option for the Ghana 32 m telescope. A kite requires wind and is generally unstable. The height of the telescope structure makes the crane option also expensive. The most feasible options for the AVN project are thus the unmanned balloon and UAV photogrammetry options as described by Copley *et al.* [36]. Figure 5.2 illustrates a typical unmanned balloon photogrammetry setup.

Figure 5.2: Ballon Photogrammetry [37]

5.2 Theodolite and Tape Measured Error

Figure 2.5 shows the theodolite and tape mounting on the backup radial truss structure on the Ghana 32 m diameter dish during the initial panel resetting by TIW Systems [38]. The surface error contour plot from the measured data is shown in figure 5.3, with the dish oriented at a 60° elevation angle. Two hundred and ninety-one (291) targets were recorded at the panel adjustment node positions.

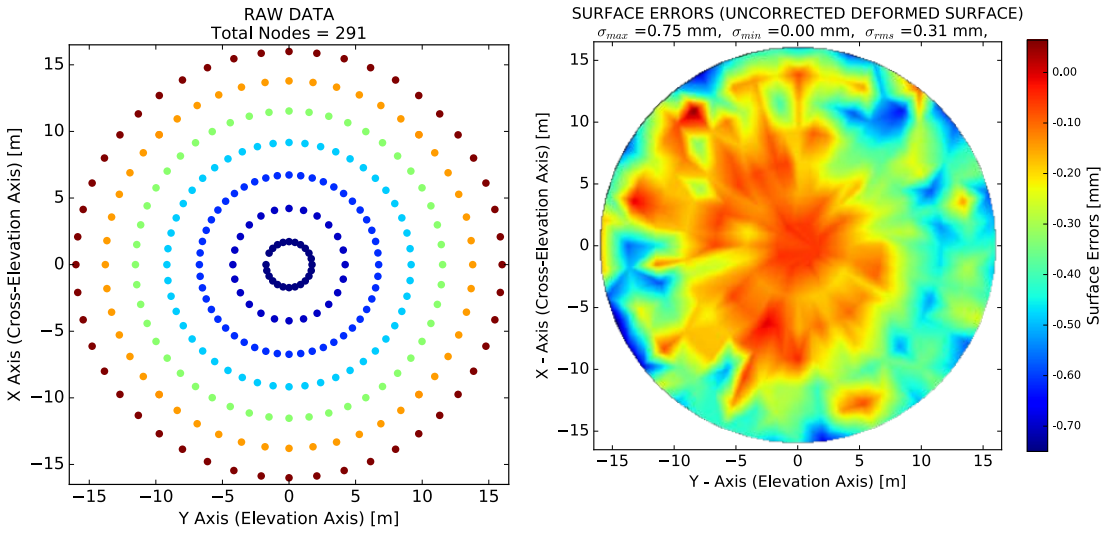

(a) Nodal Data at 60° Elevation Angle (b) Contour Plot of σ_{rms} at 60° Elevation Angle

Figure 5.3: Ghana 32 m Telescope Surface Error Plot after Installation

The panel's target nodes after readjustment reduced the RMS surface error of the dish from 0.31 mm to 0.12 mm as shown in figure 5.4.

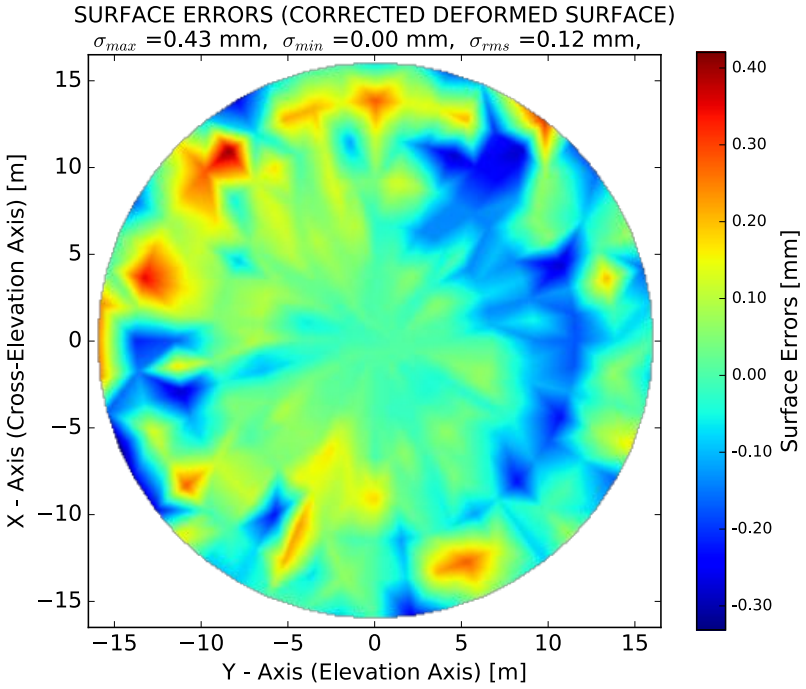

Figure 5.4: Surface Error Contour Plot after Correction

5.3 Measured and Simulated Results

A corresponding numerical model at 60° elevation angle with a vertical thermal gradient of 8 °C from an ambient temperature condition and an average wind load of 5.56 m/s wind speed at site median was created to compare with the measured surface error results. Figure 5.5 shows the RMS surface error value of 0.73 mm from the Ghana 32 m telescope's numerical model as compared to the 0.31 mm initial measurements.

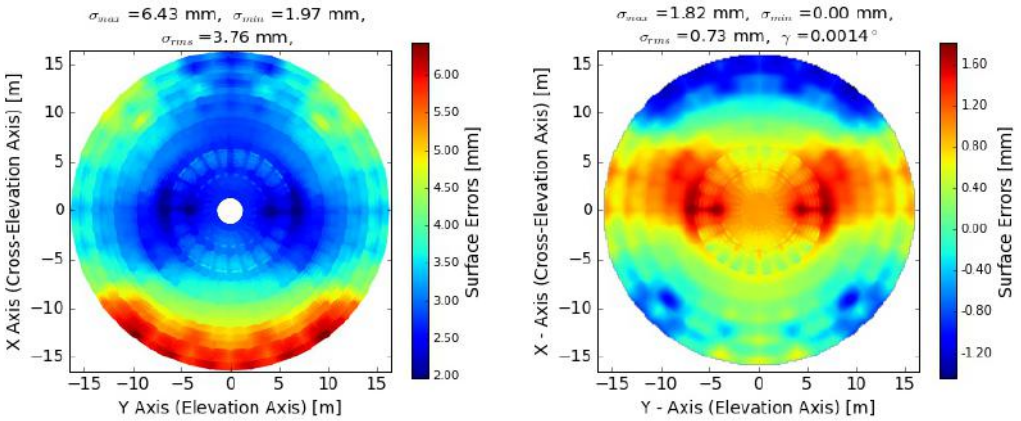

(a) Surface Deformation (Raw Data) (b) Surface Errors (RBM removed)

Figure 5.5: FE Model's Surface Error Contour Plot

The main difference between the simulated data and the uncorrected measured surface data can be attributed to:

1. Unknown thermal and wind site conditions under which the surface measurement was obtained. The installation document [38] did not provide this site condition information.
2. The theodolite and tape measurement technique is known to perform poorly compared to holography, laser scanning and photogrammetry as submitted by Usoff *et al.* [39].
3. Intrinsic panel deformation and installation misalignment of corner panel nodes.
4. Assumptions and simplifications in the numerical model.

Notwithstanding these discrepancies, the RMS surface errors fall within the required 2.8 mm surface accuracy for the first phase of science observation. Further surface error measurements will be required after the conversion works

on the Ghana 32 m radio telescope are completed to compare the other load cases under similar operational conditions.

Chapter 6

Optimizing the Telescope

The immediate goal of the AVN Ghana 32 m radio telescope is to renovate its hardware and software to either perform single dish science observation or in VLBI at 6.7 GHz [11]. The panel misalignment during installation, intrinsic panel deformation and the telescope elevation backup structure stiffness contributes to the parabolic surface roughness. The dish surface could be further tuned by measuring the surface roughness with either photogrammetry or holography. Numerical optimization also proves to be a useful tool in evaluating and improving the surface deformation of the reflector surface during the design phase of the telescope. Since the Ghana 32 m radio telescope is an old telecommunication antenna and is currently under conversion, only feasibly structural add-ons could be optimized to determine its influence on the RMS surface and pointing error of telescope.

This chapter studied the influence of some feasible add-on components on the surface deformation performance of the Ghana 32 m radio telescope.

6.1 Feasible Design Add-ons

The simulation of the telescope shows some movement of the counterweight structure in what is known as the "bat wing motion" described by the original designers of the structure. This has some influence on the deformation field of the dish surface and can be reduced by introducing some stiffened structures that reduce this effect. The proposed stiffened counterweight structure of the Ghana telescope is shown in figure 6.1. The pipe's internal diameter and thickness was manually adjusted to 6.5 mm thick and 75 mm internal diameter to evaluate its effect on the telescope's surface deformation.

The surface and pointing accuracy improved from 0.51 mm to 0.32 mm and 0.0016° to 0.0003° respectively with the telescope oriented at 0° elevation/azimuth angle (load case, LC1) as shown in figure 6.2 and figure 6.3.

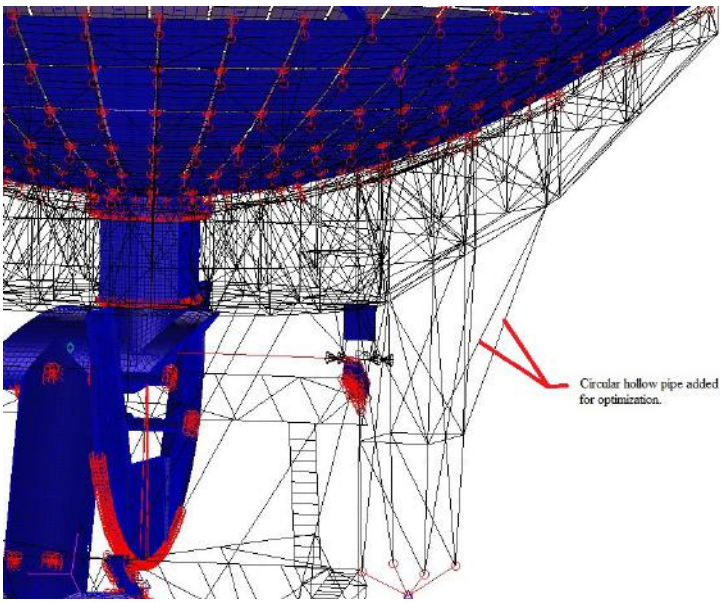

Figure 6.1: Ghana 32 m Telescope with Counterweight Stiffened Support

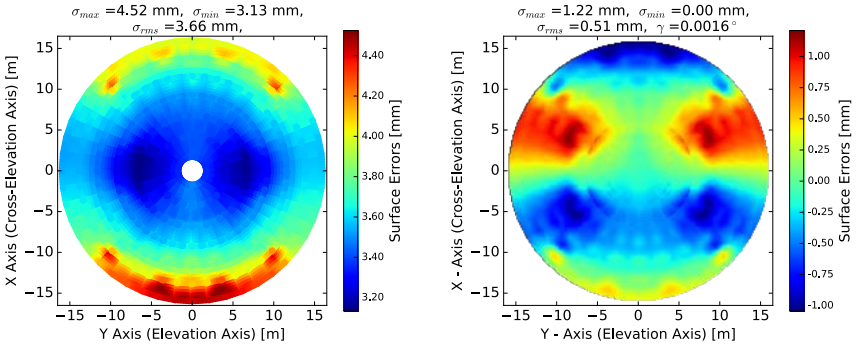

Figure 6.2: Dish Deformation without Stiffener

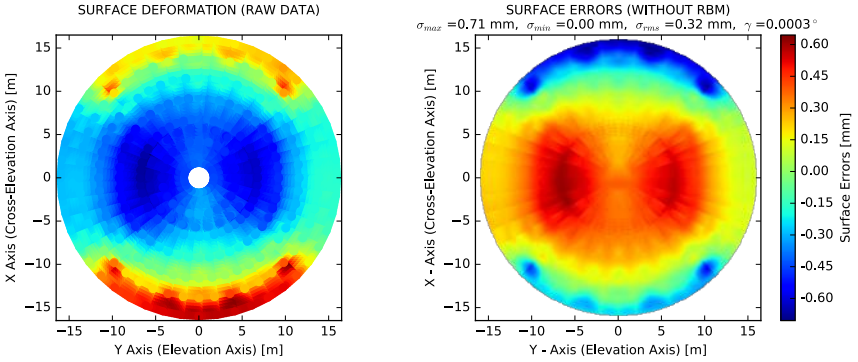

Figure 6.3: Dish Deformation with Stiffened Counterweight Support

The telescope with the stiffened counterweight support structure can be further improved by submitting it to a numerical optimization within the Genesis

structural analysis and optimization software [40] to find an optimal solution that will improve the RMS surface/pointing errors. The numerical optimization problem is posed in section 6.2.

6.2 Numerical Optimization

The FE model with the stiffened design add-on supports can be imported into Genesis to set up a sizing optimization problem. A routine that calculates the external responses (RMS surface and pointing errors) could be coupled to the Genesis software for the optimization.

The optimization problem statement [41] is as:

Minimize

$$F(\boldsymbol{x})$$

Subject to (constraints):

$$g_j(\boldsymbol{x}) \leq 0; j = 1, ..., m$$

$$x_i^L \leq x_i \leq x_i^U; i = 1, ..., n$$

where F is the objective function that minimizes the RMS surface and pointing error of the telescope, $\boldsymbol{x}$ is the design variable vector (pipe support's thickness and inner diameter), $g_j(\boldsymbol{x})$ are the constraints that provide bounds on response quantities such as the Von Mises stress, mass, RMS surface and pointing error of the telescope, and x_i^L and x_i^U are the lower and upper bound values for the design variables.

Some possible areas of the Ghana 32 m telescope structure that can deploy numerical optimization to improve its surface and pointing performance are discussed in section 7.1.2 as future recommendation works.

Chapter 7

Concluding Remarks

The FE and CAD models of the Ghana 32 m radio telescope were created. The preliminary results show that the telescope satisfies the surface accuracy requirement for the first phase of the AVN project's scientific goal at a 5 GHz to 6.7 GHz observing frequency. The predicted pointing error resulting from structural deformation is an essential component of the telescope's pointing model. The overall telescope's pointing error encompasses several other factors such as mechanical misalignment and servo drive train errors that are also evaluated and used by the control system in providing corrections to the pointing vector of the instrument during observations.

This research is a work-in-progress aimed at improving the surface and pointing performance of the Ghana 32 m radio telescope for high observing frequencies up to 18 GHz. This translates into further tuning of the reflector surface irregularities to be within the required surface accuracy during operations. The numerical model can be further developed to study the radio telescope's structural dynamics responses as a result of control system inputs. In this chapter, few areas for further studies are identified with some recommendations and conclusion.

7.1 Future Recommended Work

Future upgrades to the current conversion phase of the Ghana 32 m radio telescope poses a challenging task as the surface and pointing accuracy requirements become more stringent. There is the need for further studies and implementation of more efficient techniques and advanced telescope's metrology to meet these challenges. Some of the major recommendations requiring further investigations aimed at improving the numerical model and the overall pointing performance of the Ghana 32 m radio telescope are listed below.

7.1.1 Foundation Deformation and Track-Level Unevenness

The FE model assumed a rigid foundation and perfectly flat track rail plane due to the thesis scope of work. However, in reality, both these assumptions contribute to the telescope's pointing performance. These assumptions require further investigation to assess their impact on the overall pointing error. A numerical model that captures the building foundation's stiffness can be investigated and developed to accurately predicts its deformation. The unevenness of the azimuth track-level due to manufacturing tolerance and degradation over the years will results in the telescope's structure tilting as its wheels travel on the track rail. These tilting does influence the pointing vector of the telescope but represents a repeatable error contributor over the entire azimuth travel range. A look-up table detailing the track-level compensation as a function of the elevation and azimuth angle can be experimentally determined to compensate for the track rail's surface unevenness as implemented on most DSN antennas [42, 43].

7.1.2 Structural Optimization

The application of structural numerical optimization will be a useful tool to study the influence of stiffening the structure in areas experiencing large strains. The effect of redistributing the counterweight mass by moving some of it's mass to the elevation wheel structure (closer to the centre of mass of the elevation assembly) will be worth while to investigate. The "bat wing" motion of the counterweight structure could be further minimized by optimally introducing a connecting strut between the two counterweight frame structures. In addition, identifying and stiffening weak areas of the backup structure to minimize the dish surface deformation and checking the resulting influence on the telescope's surface and pointing error would form an interesting study.

7.1.3 General Further Studies

Other recommended studies aimed at improving the radio telescope's performance and numerical model include the following.

Wind Gust: It is worth while to investigate the possibility of developing a numerical model that captures wind gusts. This could be useful for compensation by the drive controls in moderating the telescope's jitters due to the gusty wind during operation.

Global Thermal Change The effect of the thermal gradient was investigated with the assumption that temperature varies across the entire structure.

Additional analysis on the global thermal change and its influence on the total error, therefore, requires further investigation.

Accrued Damage: The antenna passed the initial structural integrity survey for use as a radio telescope. Further on-site investigations and measurements of degraded structural members could be replicated on the numerical model to refine the FE model's response to better match that of the actual telescope.

Servo Drive-Train System's Errors: These errors are mostly non-repeatable errors influenced by factors such as the properties of the main drives, the azimuth wheel slips, encoder error, the backlash of drives and friction variation. Further studies will be required to quantify these errors since their total effect on the telescope's overall pointing performance cannot be overlooked.

FE Model's Refinement and Sensitivity Analysis: A more detail analysis such as zooming in on the thermal loading on the drive encoder systems and its impact on the overall telescope performance will be worth while to investigate. The FE model can be further improved by mesh refinement and sensitivity studies.

7.1.4 Pointing Error Model

A comprehensive study on evaluating the Ghana 32 m radio telescope overall pointing model is required to accurately predict the telescope's pointing tolerances during observations. The structural deformation due to gravity, the wind, and thermal loading is only part of the total mechanical pointing performance of the telescope. The other mechanical factors include alignment errors that result from the axis skew, and azimuth (hour angle) collimation, azimuth axis tilt, intrinsic panel manufacturing errors, installed panel misalignment errors and encoder offsets.

The fully populated telescope pointing error model accounts for all factors, including atmospheric refraction due to the bending of radio waves through the sky, receiver errors, and control system software errors.

7.1.5 Metrology at High Observing Frequencies

The instrumentation for radio telescope metrology involves the ability to perform high precision measurements of operational conditions and also provides a corrective response. Active surface control systems, tiltmeters, temperature sensors and steerable secondary reflector systems are some of the instruments utilised in modern telescopes to achieve higher performance.

The active surface control systems employ precision stepper motor actuators placed at the corners of each reflector panel to provide real time corrections in bringing the reflector panels closer to their ideal paraboloid shape as it deforms during pointing or tracking of celestial sources. The FE model together with other systems such as temperature sensors, weather station information, and tiltmeters can be used to predict the dish surface errors and provide feedback controls to the panel actuators.

An actuation mechanism can be integrated into the secondary reflector structure to compensate for its rotation, axial and lateral motions to concentrate the reflected electromagnetic waves onto the beam waveguide mirrors.

7.2 Conclusion

In conclusion, a numerical model of the Ghana 32 m radio telescope was created from available engineering data and on-site measurements in line with the first objective of this research. The numerical model captures most of the relevant structural members of the antenna as detailed in the CAD model, created to determine the non-structural mass distributions. The RMS surface error results of the numerical model owing to wind loading compare well with the JPL 26 m antenna published results discussed in section 4.5 with similar trends.

The model simulated thirty (30) different operating load cases including worst case scenarios that result in structural deformations of the radio telescope as required by the second research objective. The numerical simulations captured gravity, steady-state wind and thermal (gradient) load, representing different operational conditions.

The numerically simulated pointing errors will be integrated into the Ghana 32 m radio telescope's pointing model once further validated with photogrammetry or holography measurement of the dish surface by the SKA-AVN team. This research serves as a foundation for further investigation and analysis aimed at improving the overall performance of the Ghana 32 m radio telescope and the knowledge accrued can be extended to AVN projects in other African countries.

Appendices

Appendix A

Material Properties

Table A.1: Section and Material Properties of the Ghana 32 m Radio Astronomy Telescope

Back-to-Back Angle Iron Simplified as T-Section

Material Type	: ASTM A36
Youngs Modulus	: 200 GPa
Poison Ratio	: 0.26
Density	: 7850 kg/m^3
Reference	: http://www.efunda.com

Section Properties from Source Data

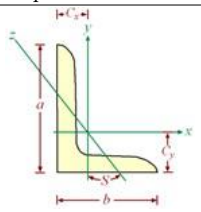

MSC Patran/Nastran Input Data

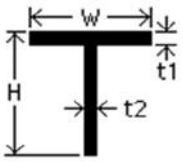

No.	Specs (TIW [9])	a [m]	b [m]	t [m]	W [m]	H [m]	t1 [m]	t2 [m]
1	2L6x4x1/2	0.1524	0.1016	0.0127000	0.2032	0.1524	0.0127000	0.025400
2	2L2.5x2x3/16	0.0635	0.0508	0.0047625	0.1016	0.0635	0.0047625	0.009525
3	2L3x2x1/4	0.0762	0.0508	0.0063500	0.1016	0.0762	0.0063500	0.012700
4	2L5x3.5x5/16	0.1270	0.0889	0.0079375	0.1778	0.1270	0.0079375	0.015875
5	2L3x2.5x3/16	0.0762	0.0635	0.0047625	0.1270	0.0762	0.0047625	0.009525
6	2L4x3x1/4	0.1016	0.0762	0.0063500	0.1524	0.1016	0.0063500	0.012700
7	2L5x3.5x1/4	0.1270	0.0889	0.0063500	0.1778	0.1270	0.0063500	0.012700
8	2L2.5x1.5x3/16	0.0635	0.0381	0.0047625	0.0762	0.0635	0.0047625	0.009525
9	2L3.5x2.5x1/4	0.0889	0.0635	0.0063500	0.1270	0.0889	0.0063500	0.012700
10	2L5x3.5x3/8	0.1270	0.0889	0.0095250	0.1778	0.1270	0.0095250	0.019050
11	2L4x4x3/8	0.1016	0.1016	0.0095250	0.2032	0.1016	0.0095250	0.019050
12	2L3x2.5x5/16	0.0762	0.0635	0.0079375	0.1270	0.0762	0.0079375	0.015875
13	2L5x5.5x1/4	0.1270	0.1397	0.0063500	0.2794	0.1270	0.0063500	0.012700
14	2L6x4x1/4	0.1524	0.1016	0.0063500	0.2032	0.1524	0.0063500	0.012700
15	2L5x3x3/8	0.1270	0.0762	0.0095250	0.1524	0.1270	0.0095250	0.019050
16	2L2x1.5x1/8	0.0508	0.0381	0.0031750	0.0762	0.0508	0.0031750	0.006350
17	2L2x1.5x3/16	0.0508	0.0381	0.0047625	0.0762	0.0508	0.0047625	0.009525
18	2L6x4x1/2	0.1524	0.1016	0.0127000	0.2032	0.1524	0.0127000	0.025400

Back-to-Edge Angle Iron simplified as Z-Section

Material Type : ASTM A36
Youngs Modulus : 200 GPa
Poison Ratio : 0.26
Density : 7850 kg/m^3
Reference : http://www.efunda.com

Section Properties from Source Data

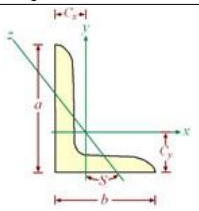

MSC Patran/Nastran Input Data

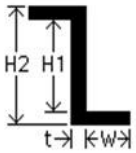

No.	Specs (TIW [9])	a [m]	b [m]	t [m]	W [m]	t [m]	H1 [m]	H2 [m]
19	2Z2x2x3/16	0.0508	0.0508	0.0047625	0.0460375	0.009525	0.041275	0.0508
20	2Z2x2x5/16	0.0508	0.0508	0.0079375	0.0428625	0.015875	0.034925	0.0508

Reflector Panel Z-Section Stiffener

Material Type : Al 6061-T6
Youngs Modulus : 68.9 GPa
Poison Ratio : 0.33
Density : 2700 kg/m^3

MSC Patran/Nastran Input Data

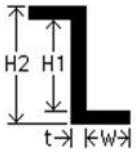

No.	Specs (TIW [9])	W [m]	t [m]	H1 [m]	H2 [m]
21	Z2x3 3/16x3/16	0.0460375	0.0047625	0.0666623	0.0793623
22	Z2x3x1/8	0.0476250	0.0031750	0.0698500	0.0762000

Angle Iron

Material Type : ASTM A36
Youngs Modulus : 200 GPa
Poison Ratio : 0.26
Density : 7850 kg/m^3
Reference : http://www.efunda.com

Section Properties from Source Data

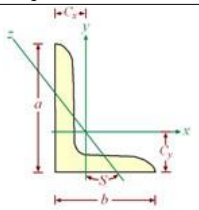

MSC Patran/Nastran Input Data

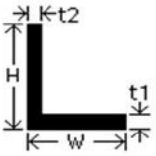

No.	Specs (TIW [9])	a [m]	b [m]	t [m]	W [m]	H [m]	t1=t2 [m]
23	L5x3.5x3/8	0.1270	0.0889	0.0095250	0.0889	0.1270	0.0095250
24	L4x4x3/8	0.1016	0.1016	0.0095250	0.1016	0.1016	0.0095250
25	L6x6x3/4	0.1524	0.1524	0.0190500	0.1524	0.1524	0.0190500
26	L6x6x3/8	0.1524	0.1524	0.0095250	0.1524	0.1524	0.0095250
27	L3x3x1/4	0.0762	0.0762	0.0063500	0.0762	0.0762	0.0063500
28	L3x3x3/16	0.0762	0.0762	0.0047625	0.0762	0.0762	0.0047625
29	L4x3.5x3/8	0.1016	0.0889	0.0095250	0.0889	0.1016	0.0095250

Channel

Material Type : ASTM A36
Youngs Modulus : 200 GPa
Poison Ratio : 0.26
Density : 7850 kg/m^3
Reference : http://www.efunda.com

Section Properties from Source Data

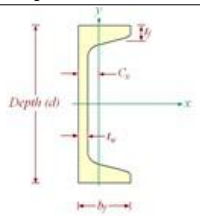

MSC Patran/Nastran Input Data

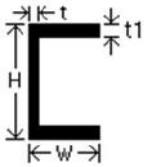

No.	Specs (TIW [9])	d [m]	bf [m]	tf [m]	tw [m]	W [m]	H [m]	t [m]	t1 [m]
30	C10x15.5 (C10x15.3 available)	0.2540	0.0660400	0.0110744	0.0060960	0.2540	0.0660400	0.0060960	0.0110744
31	C6x8.2	0.1524	0.0487680	0.0087122	0.0050800	0.1524	0.0487680	0.0050800	0.0087122
32	C7x9.8	0.1778	0.0530860	0.0092964	0.0053340	0.1778	0.0530860	0.0053340	0.0092964
33	C8x11.5	0.2032	0.0574040	0.0099060	0.0055880	0.2032	0.0574040	0.0055880	0.0099060
34	C12x20.7	0.3048	0.0747268	0.0127254	0.0071628	0.3048	0.0747268	0.0071628	0.0127254

I-Beam

Material Type : ASTM A36
Youngs Modulus : 200 GPa
Poison Ratio : 0.26
Density : 7850 kg/m^3
Reference : Melton Steel Ltd. Catalogue
Aisc Manual 7th Edition
Super Steel PTY Ltd. Catalogue

Section Properties from Source Data

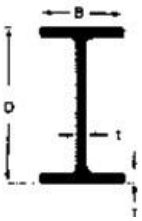

MSC Patran/Nastran Input Data

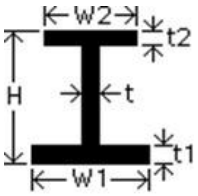

No.	Specs (TIW [9])	D [m]	B [m]	t [m]	T [m]	W1=W2[m]	H [m]	t [m]	t1=t2[m]
35	W12x50	0.309600	0.20520	0.0094000	0.0162000	0.20520	0.309600	0.0094000	0.0162000

36	W12x79	0.314500	0.30680	0.0119400	0.0186700	0.30680	0.314500	0.0119400	0.0186700
37	W6x15.5	0.152400	0.15240	0.0060960	0.0068326	0.15240	0.152400	0.0060960	0.0068326
38	W8x17	0.203200	0.13340	0.0058000	0.0078000	0.13340	0.203200	0.0058000	0.0078000
39	W10x21	0.251500	0.14610	0.0061000	0.0086000	0.14610	0.251500	0.0061000	0.0086000
40	W10x60	0.259600	0.25600	0.0106700	0.0172700	0.25600	0.259600	0.0106700	0.0172700
41	W12x31	0.307100	0.16570	0.0067000	0.0118000	0.16570	0.307100	0.0067000	0.0118000
42	W12x65	0.307800	0.30480	0.0099000	0.0153000	0.30480	0.307800	0.0099000	0.0153000
43	W14x87	0.355600	0.36830	0.0107000	0.0175000	0.36830	0.355600	0.0107000	0.0175000
44	W14x127	0.371475	0.37465	0.0158750	0.0254000	0.37465	0.371475	0.0158750	0.0254000
45	W18x70	0.457200	0.22225	0.0111252	0.0190754	0.22225	0.457200	0.0111252	0.0190754
46	W24x84	0.612100	0.22910	0.0119400	0.0195800	0.22910	0.612100	0.0119400	0.0195800
47	W24x130 (W24x131 Available)	0.621800	0.32650	0.0153700	0.0243800	0.32650	0.621800	0.0153700	0.0243800
48	W30x108	0.757700	0.26610	0.0138400	0.0193000	0.26610	0.757700	0.0138400	0.0193000
49	W25					W1=0.3048 W2=0.4572	0.635000	0.0190500	t1=0.0254 t2=0.0381

MT-Beam

Material Type : ASTM A36
Youngs Modulus : 200 GPa
Poison Ratio : 0.26
Density : 7850 kg/m^3
Reference : Melton Steel Ltd. Catalogue

Section Properties from Source Data

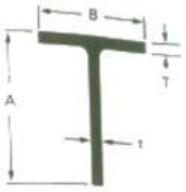

MSC Patran/Nastran Input Data

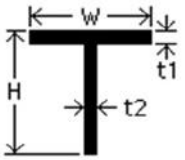

No.	Specs (TIW [9])	A [m]	B [m]	t [m]	T [m]	W [m]	H [m]	t1 [m]	t2 [m]
50	MT4X11.25 (MT4X11 Available)	0.1563	0.1024	0.0066	0.0108	0.1563	0.1024	0.0066	0.0108

Tube Section

Material Type : ASTM A36
Youngs Modulus : 200 GPa
Poison Ratio : 0.26
Density : 7850 kg/m^3
Reference : Melton Steel Ltd. Catalogue

MSC Patran/Nastran Input Data

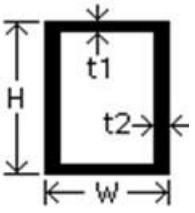

No.	Specs (TIW [9])				W [m]	H [m]	t1 [m]	t2 [m]
51	TS4x4x0.250	0.1016	0.1016	0.0063500	0.1016	0.1016	0.0063500	0.0063500
52	TS3x3x0.250	0.0762	0.0762	0.0063500	0.0762	0.0762	0.0063500	0.0063500
53	TS5x5x3/8	0.1270	0.1270	0.0152400	0.1270	0.1270	0.0152400	0.0152400
54	TS3x3x0.313	0.0762	0.0762	0.0079502	0.0762	0.0762	0.0079502	0.0079502
55	TS2.5x2.5x0.150	0.0635	0.0635	0.0038100	0.0635	0.0635	0.0038100	0.0038100
56	TS3x3x3/16	0.0762	0.0762	0.0047625	0.0762	0.0762	0.0047625	0.0047625
57	TS2x2x0.150	0.0508	0.0508	0.0038100	0.0508	0.0508	0.0038100	0.0038100

Pipe Section

Material Type : ASTM A36
Youngs Modulus : 200 GPa
Poison Ratio : 0.26
Density : 7850 kg/m^3
Reference : Melton Steel Ltd. Catalogue

MSC Patran/Nastran Input Data

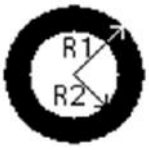

No.	Specs (TIW [9])	Mass per meter [kg/m]	Outer Diameter [m]	Thickness [m]	R1 [m]	R2 [m]
58	Pipe3xSTR	8.77	0.0761	0.0050	0.03805	0.03305
59	Pipe4xSTR	16.80	0.1143	0.0063	0.05715	0.05085

MSC Patran/Nastran Input Data

Elevation Axle Section

Material Type : AISI 1040
Youngs Modulus : 200 GPa
Poison Ratio : 0.29
Density : 7845 kg/m^3

No.	Specs (TIW [9])	R [m]
60	EAX0.1905	0.1905

Azimuth Axle Section

Material Type : AISI 1022
Youngs Modulus : 205 GPa
Poison Ratio : 0.29
Density : 7868 kg/m^3

No.	Specs (TIW [9])	R [m]
61	AAX0.0820	0.0820

Appendix B

Structural Deformation Load Cases

Table B.1: Ghana 32 m Radio Telescope's Load Cases

Load Case	Operational Condition	Description
LC1	A1,D1,E1	Telescope under gravity loading at 0° elevation/azimuth angle
LC2	A1,D2,E1	Telescope under gravity loading at 60° elevation and 0° azimuth angle
LC3	A1,D3,E1	Telescope under gravity loading at 90° elevation and 0° azimuth angle
LC4	A1,D2,E2	Telescope under gravity loading at 60° elevation and 180° azimuth angle
LC5	A1,D1,E2	Telescope under gravity loading at 0° elevation and 180° azimuth angle
LC6	B1,D1,E1	Telescope under thermal loading ($\frac{\delta T}{\delta Z}$ = 8 °C) only at 0° elevation/azimuth angle (see figure 3.23a)
LC7	B1,D2,E1	Telescope under thermal loading ($\frac{\delta T}{\delta Z}$ = 8 °C) only at 60° elevation and 0° azimuth angle (see figure 3.23b)
LC8	B1,D3,E1	Telescope under thermal loading only ($\frac{\delta T}{\delta Z}$ = 8 °C) at 90° elevation and 0° azimuth angle (see figure 3.23c)
LC9	B1,D2,E2	Telescope under thermal loading ($\frac{\delta T}{\delta Z}$ = 8 °C) only at 60° elevation and 180° azimuth angle (see figure 3.23d)
LC10	B1,D1,E2	Telescope under thermal loading ($\frac{\delta T}{\delta Z}$ = 8 °C) only at 0° elevation and 180° azimuth angle (see figure 3.23e)
LC11	B2,D1,E1	Telescope under thermal loading ($\frac{\delta T}{\delta X}$ = 8 °C) only at 0° elevation/azimuth angle from left to right (see figure 3.24b)
LC12	B3,D1,E1	Telescope under thermal loading ($\frac{\delta T}{\delta Y}$ = 8 °C) only at 0° elevation/azimuth angle from front to back (see figure 3.24c)

LC13	C2,D1,E1	Telescope operating at 5.56 m/s average wind speed only at 0° elevation/azimuth angle
LC14	C2,D2,E1	Telescope operating at 5.56 m/s average wind speed only at 60° elevation and 0° azimuth angle
LC15	C2,D3,E1	Telescope operating at 5.56 m/s average wind speed only at 90° elevation and 0° azimuth angle
LC16	C2,D2,E2	Telescope operating at 5.56 m/s average wind speed only at 60° elevation and 180° azimuth angle
LC17	C2,D1,E2	Telescope operating at 5.56 m/s average wind speed only at 0° elevation and 180° azimuth angle
LC18	C3,D1,E1	Telescope operating at 8.96 m/s high wind speed only at 0° elevation/azimuth angle
LC19	C3,D2,E1	Telescope operating at 8.96 m/s high wind speed only at 60° elevation and 0° azimuth angle
LC20	C3,D3,E1	Telescope operating at 8.96 m/s high wind speed only at 90° elevation and 0° azimuth angle
LC21	C3,D2,E2	Telescope operating at 8.96 m/s high wind speed only at 60° elevation and 180° azimuth angle
LC22	C3,D1,E2	Telescope operating at 8.96 m/s high wind speed only at 0° elevation and 180° azimuth angle
LC23	C1,D2,E1	Telescope operating at 3 m/s low wind speed at 60° elevation and 0° azimuth angle
LC24	C4,D2,E1	Telescope operating at 13.41 m/s high wind speed at 60° elevation and 0° azimuth angle
LC25	A1,B1,C2,D1,E1	Typical day with average operation condition at 0° elevation/azimuth angle
LC26	A1,B1,C2,D2,E1	Typical day with average operation condition at 60° elevation and 0° azimuth angle
LC27	A1,B1,C2,D3,E1	Typical day with average operation condition at 90° elevation and 0° azimuth angle
LC28	A1,B1,C2,D2,E2	Typical day with average operation condition at 60° elevation and 180° azimuth angle
LC29	A1,B1,C2,D1,E2	Typical day with average operation condition at 0° elevation and 180° azimuth angle
LC30	D1,E1,F	Normal mode analysis at 0° elevation/azimuth angle

Appendix C

Contour Plots of RMS Surface and Pointing Errors

C.1 LC1 to LC5

Gravitational Loading on the Ghana 32 m Radio Telescope

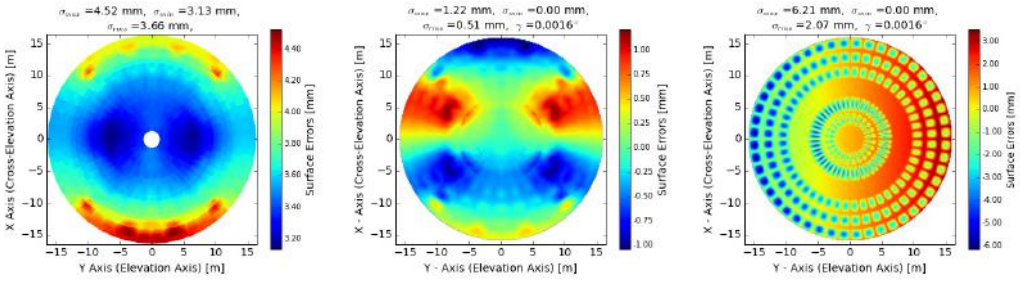

(a) Surface Deformation (Raw Data)

(b) Surface Errors (RBM removed)

(c) Best Fit Surface Errors (RBM removed)

Figure C.1: Dish at 0° Elevation/Azimuth Angle

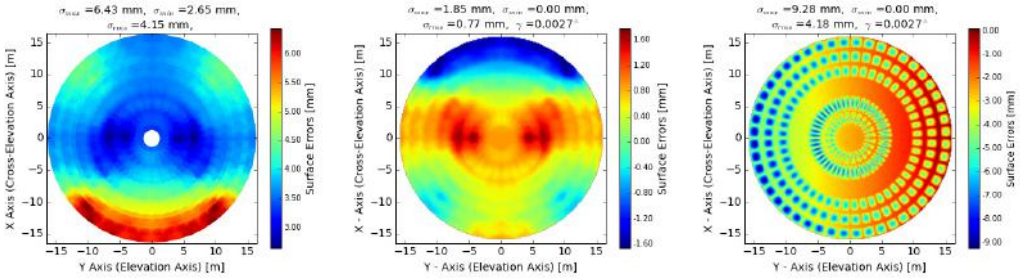

(a) Surface Deformation (Raw Data)

(b) Surface Errors (RBM removed)

(c) Best Fit Surface Errors (RBM removed)

Figure C.2: Dish at 60° Elevation and 0° Azimuth angle

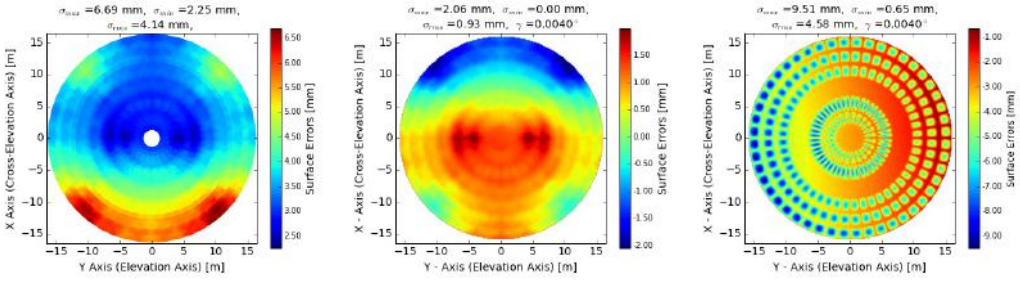

(a) Surface Deformation (Raw Data) (b) Surface Errors (RBM removed) (c) Best Fit Surface Errors (RBM removed)

Figure C.3: Dish at 90° Elevation and 0° Azimuth Angle

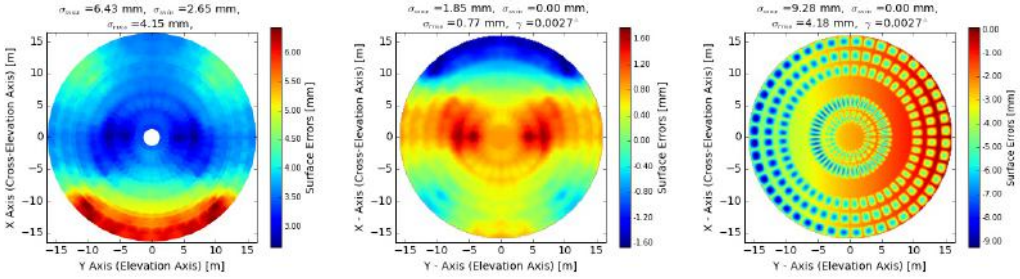

(a) Surface Deformation (Raw Data) (b) Surface Errors (RBM removed) (c) Best Fit Surface Errors (RBM removed)

Figure C.4: Dish at 60° Elevation and 180° Azimuth Angle

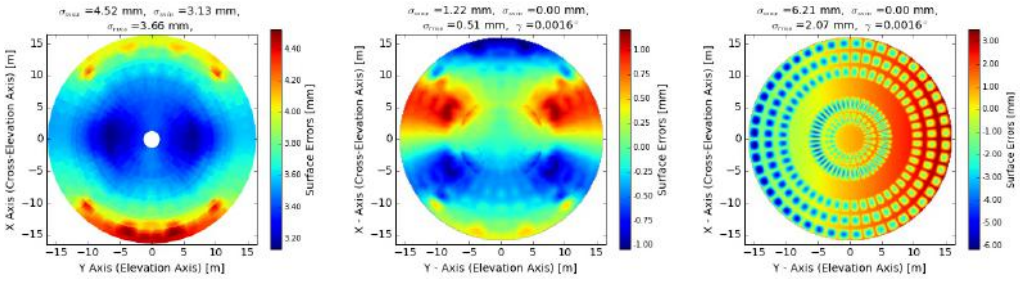

(a) Surface Deformation (Raw Data) (b) Surface Errors (RBM removed) (c) Best Fit Surface Errors (RBM removed)

Figure C.5: Dish at 0° Elevation and 180° Azimuth Angle

C.2 LC6 to LC10

Vertical Thermal Loading on the Ghana 32 m Radio Telescope

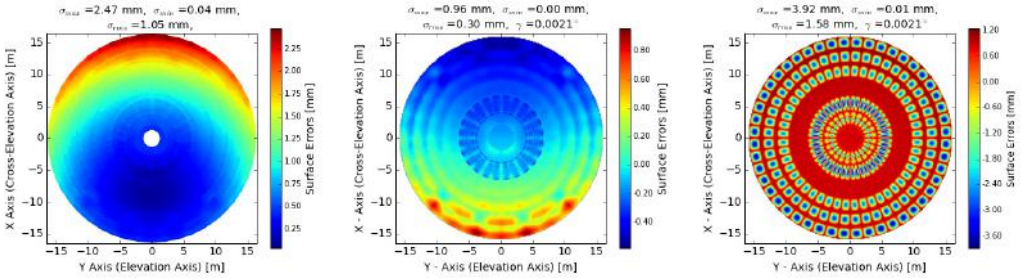

(a) Surface Deformation (Raw Data)

(b) Surface Errors (RBM removed)

(c) Best Fit Surface Errors (RBM removed)

Figure C.6: Dish at 0° Elevation/Azimuth Angle

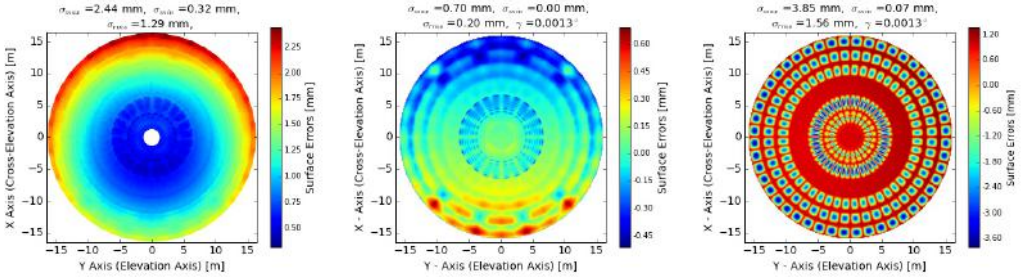

(a) Surface Deformation (Raw Data)

(b) Surface Errors (RBM removed)

(c) Best Fit Surface Errors (RBM removed)

Figure C.7: Dish at 60° Elevation and 0° Azimuth angle

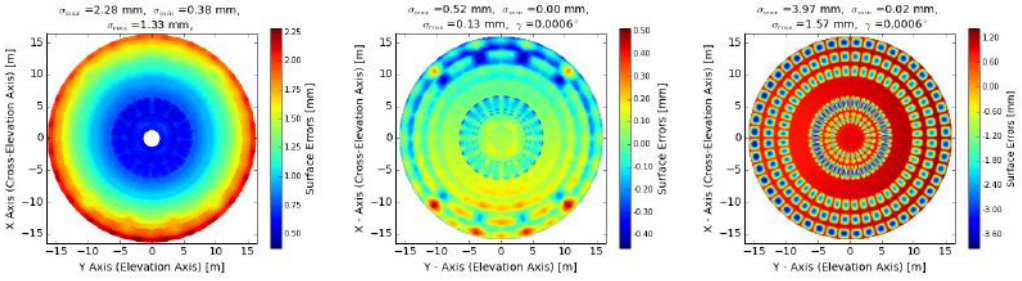

(a) Surface Deformation (Raw Data)

(b) Surface Errors (RBM removed)

(c) Best Fit Surface Errors (RBM removed)

Figure C.8: Dish at 90° Elevation and 0° Azimuth Angle

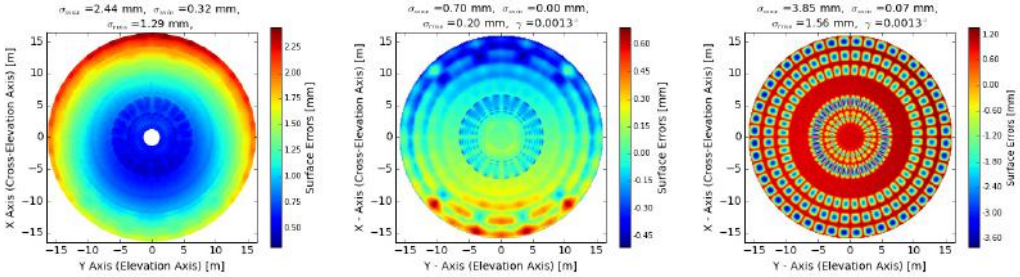

(a) Surface Deformation (Raw Data)

(b) Surface Errors (RBM removed)

(c) Best Fit Surface Errors (RBM removed)

Figure C.9: Dish at 60° Elevation and 180° Azimuth Angle

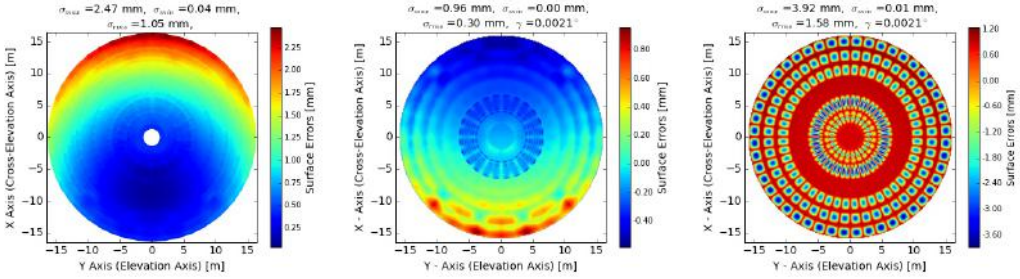

(a) Surface Deformation (Raw Data)

(b) Surface Errors (RBM removed)

(c) Best Fit Surface Errors (RBM removed)

Figure C.10: Dish at 0° Elevation and 180° Azimuth Angle

C.3 LC11 to LC12

Thermal Loading from Different Direction

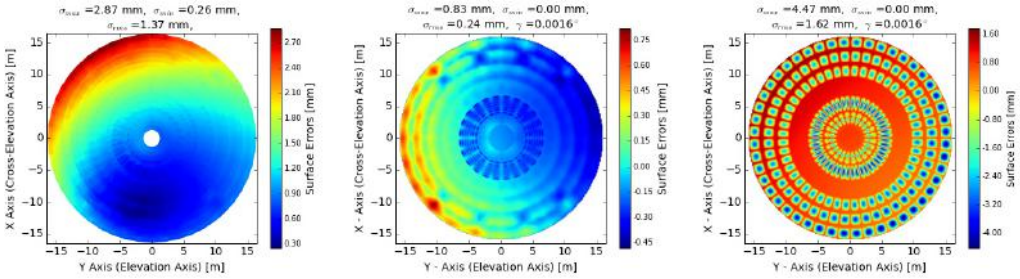

(a) Surface Deformation (Raw Data)

(b) Surface Errors (RBM removed)

(c) Best Fit Surface Errors (RBM removed)

Figure C.11: Thermal Gradient Applied from Left to Right Horizontally across entire Telescope at 0° Elevation/Azimuth Angle

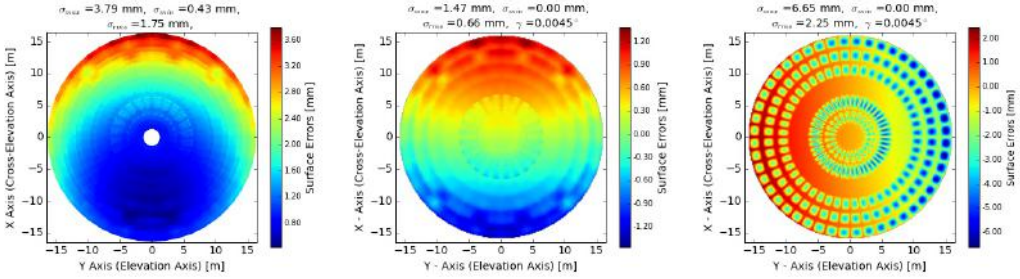

(a) Surface Deformation (Raw Data)

(b) Surface Errors (RBM removed)

(c) Best Fit Surface Errors (RBM removed)

Figure C.12: Thermal Gradient Applied from front to back Horizontally across entire Telescope at 0° Elevation/Azimuth Angle

C.4 LC13 to LC17

Wind Loading at 5.56 m/s on the Ghana 32 m Radio Telescope

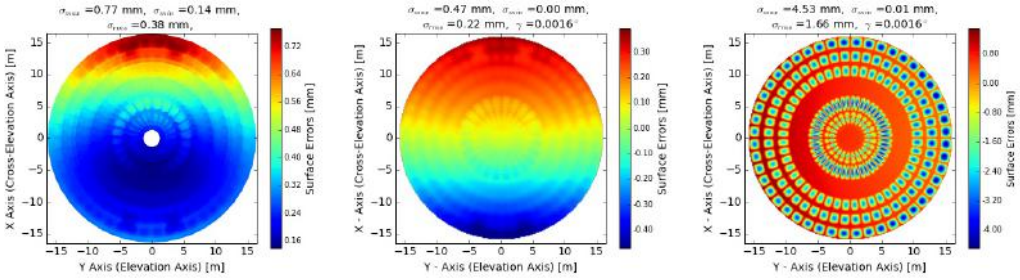

(a) Surface Deformation (Raw Data)

(b) Surface Errors (RBM removed)

(c) Best Fit Surface Errors (RBM removed)

Figure C.13: Dish at 0° Elevation/Azimuth Angle

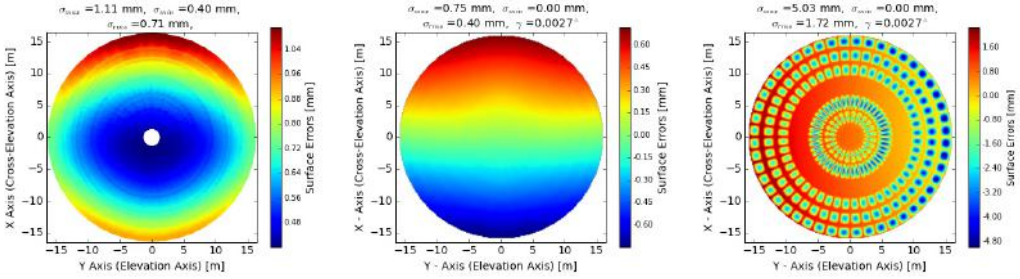

(a) Surface Deformation (Raw Data)

(b) Surface Errors (RBM removed)

(c) Best Fit Surface Errors (RBM removed)

Figure C.14: Dish at 60° Elevation and 0° Azimuth angle

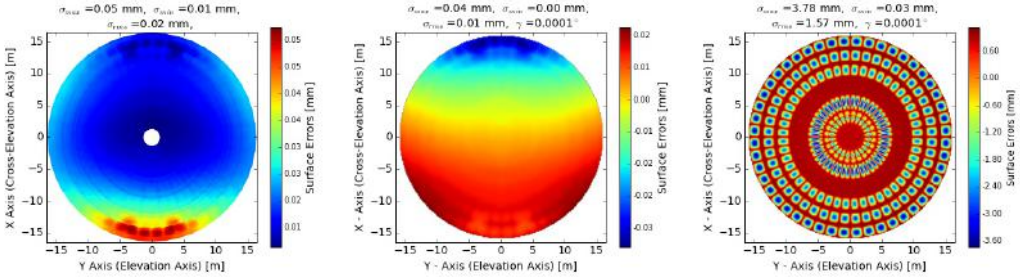

(a) Surface Deformation (Raw Data)

(b) Surface Errors (RBM removed)

(c) Best Fit Surface Errors (RBM removed)

Figure C.15: Dish at 90° Elevation and 0° Azimuth Angle

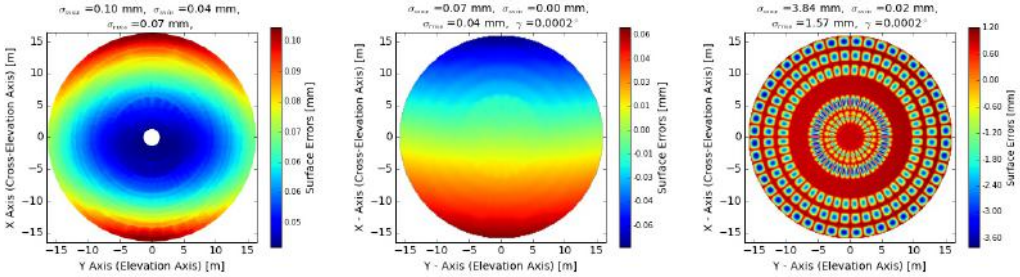

(a) Surface Deformation (Raw Data)

(b) Surface Errors (RBM removed)

(c) Best Fit Surface Errors (RBM removed)

Figure C.16: Dish at 60° Elevation and 180° Azimuth Angle

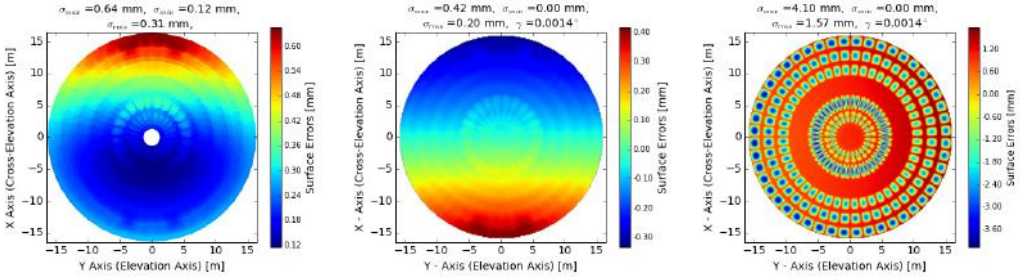

(a) Surface Deformation (Raw Data)

(b) Surface Errors (RBM removed)

(c) Best Fit Surface Errors (RBM removed)

Figure C.17: Dish at 0° Elevation and 180° Azimuth Angle

C.5 LC18 to LC22

Wind Loading at 8.96 m/s on the Ghana 32 m Radio Telescope

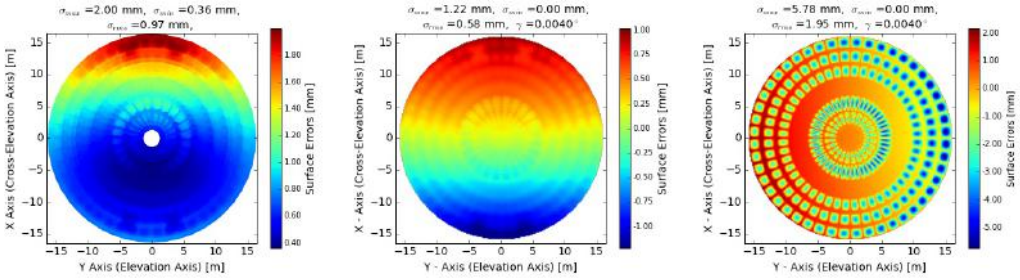

(a) Surface Deformation (Raw Data)

(b) Surface Errors (RBM removed)

(c) Best Fit Surface Errors (RBM removed)

Figure C.18: Dish at 0° Elevation/Azimuth Angle

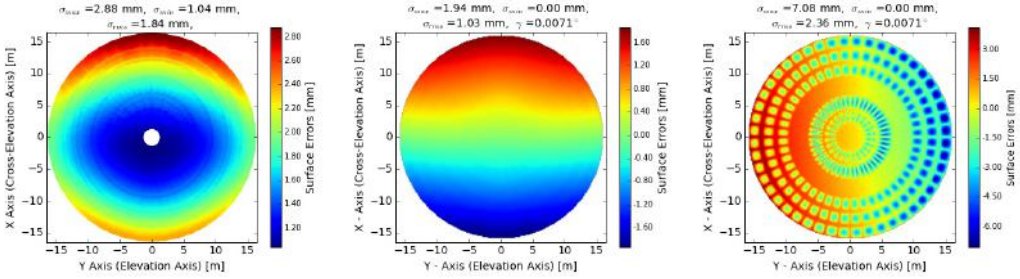

(a) Surface Deformation (Raw Data)

(b) Surface Errors (RBM removed)

(c) Best Fit Surface Errors (RBM removed)

Figure C.19: Dish at 60° Elevation and 0° Azimuth angle

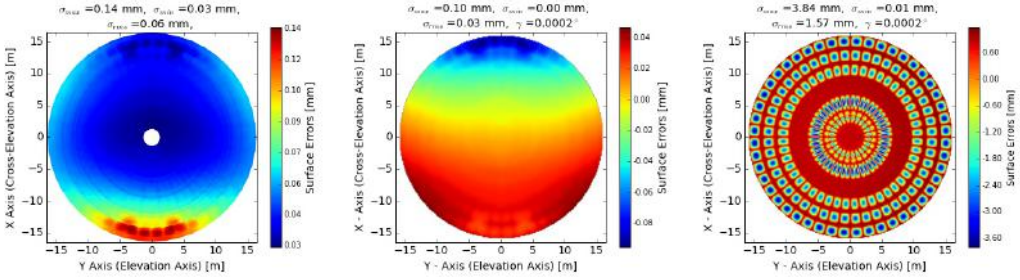

(a) Surface Deformation (Raw Data)

(b) Surface Errors (RBM removed)

(c) Best Fit Surface Errors (RBM removed)

Figure C.20: Dish at 90° Elevation and 0° Azimuth Angle

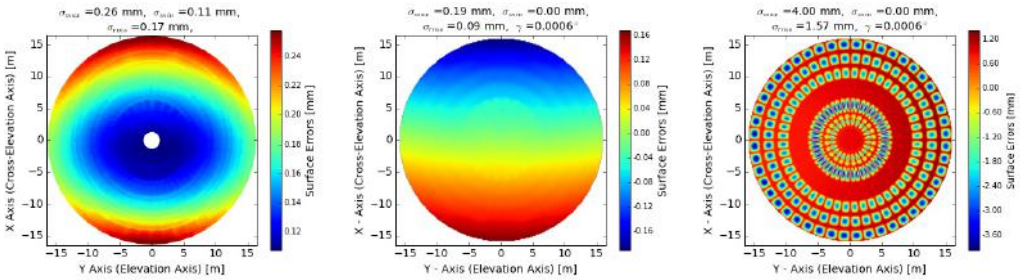

(a) Surface Deformation (Raw Data)

(b) Surface Errors (RBM removed)

(c) Best Fit Surface Errors (RBM removed)

Figure C.21: Dish at 60° Elevation and 180° Azimuth Angle

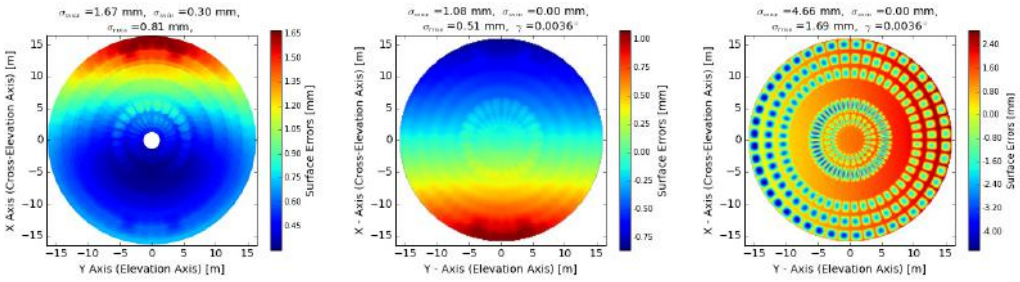

(a) Surface Deformation (Raw Data)

(b) Surface Errors (RBM removed)

(c) Best Fit Surface Errors (RBM removed)

Figure C.22: Dish at 0° Elevation and 180° Azimuth Angle

C.6 LC23 to LC24

Varying Wind Loading on the Ghana 32 m Radio Telescope at 60° Elevation and 0° Azimuth angle

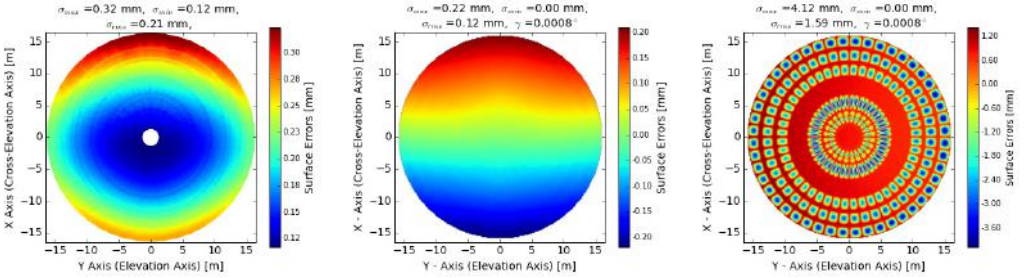

(a) Surface Deformation (Raw Data)

(b) Surface Errors (RBM removed)

(c) Best Fit Surface Errors (RBM removed)

Figure C.23: Dish with wind speed at 3 m/s

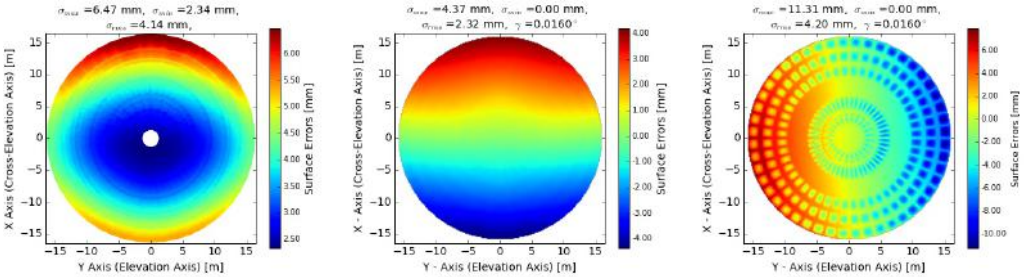

(a) Surface Deformation (Raw Data)

(b) Surface Errors (RBM removed)

(c) Best Fit Surface Errors (RBM removed)

Figure C.24: Dish with wind speed at 13.41 m/s

C.7 LC25 to LC29

Gravitation, Wind and Thermal Loading on the Ghana 32 m Radio Telescope

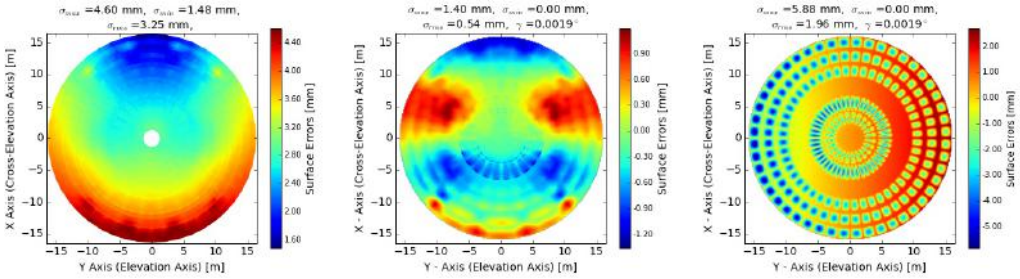

(a) Surface Deformation (Raw Data)

(b) Surface Errors (RBM removed)

(c) Best Fit Surface Errors (RBM removed)

Figure C.25: Dish at 0° Elevation/Azimuth Angle

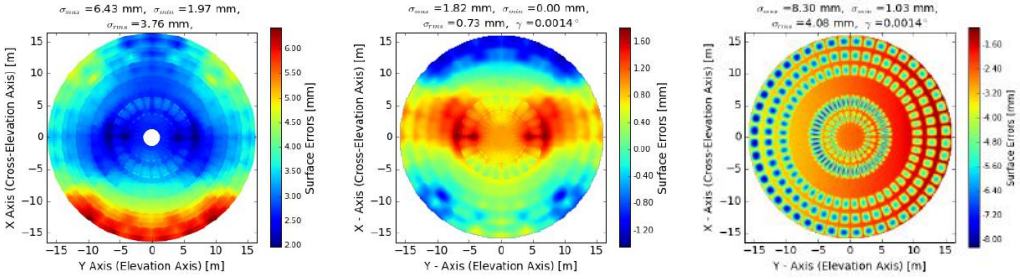

(a) Surface Deformation (Raw Data)

(b) Surface Errors (RBM removed)

(c) Best Fit Surface Errors (RBM removed)

Figure C.26: Dish at 60° Elevation and 0° Azimuth angle

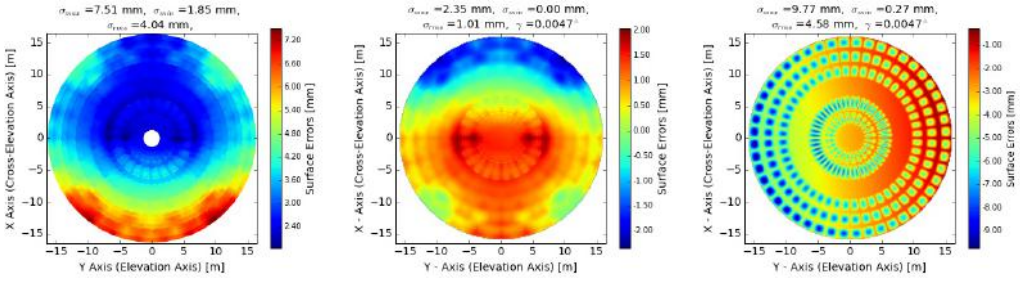

(a) Surface Deformation (Raw Data)

(b) Surface Errors (RBM removed)

(c) Best Fit Surface Errors (RBM removed)

Figure C.27: Dish at 90° Elevation and 0° Azimuth Angle

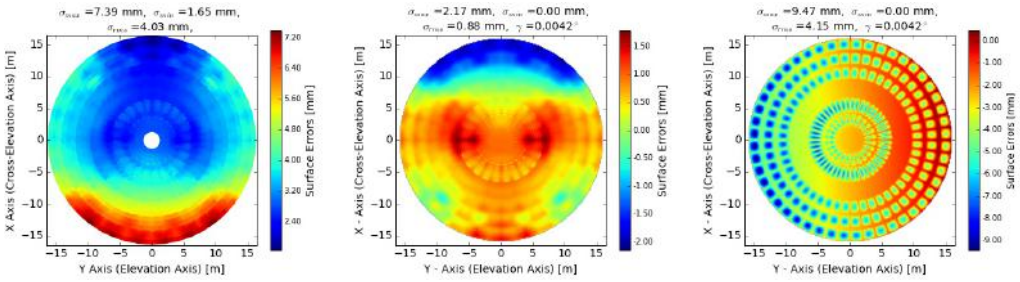

(a) Surface Deformation (Raw Data)

(b) Surface Errors (RBM removed)

(c) Best Fit Surface Errors (RBM removed)

Figure C.28: Dish at 60° Elevation and 180° Azimuth Angle

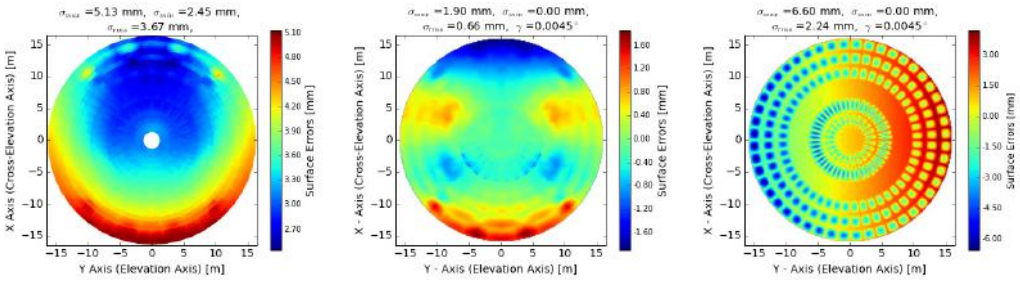

(a) Surface Deformation (Raw Data)

(b) Surface Errors (RBM removed)

(c) Best Fit Surface Errors (RBM removed)

Figure C.29: Dish at 0° Elevation and 180° Azimuth Angle

List of References

[1] Schlüter, W. and Behrend, D.: The International VLBI Service for Geodesy and Astrometry (IVS): current capabilities and future prospects. *Journal of Geodesy*, vol. 81, no. 6–8, pp. 379–387, 2007.

[2] Li, J., Zhang, J. and Guo, L.: On the monitoring model of reference point of VLBI antenna. *Science China Physics, Mechanics and Astronomy*, vol. 56, no. 10, pp. 1987–1994, 2013.

[3] Mayer, D., Böhm, J., Combrinck, L., Botai, J. and Böhm, S.: Importance of the Hartebeesthoek Radio Astronomy Observatory for the VLBI network. *Acta Geodaetica et Geophysica*, vol. 49, no. 3, pp. 313–325, 2014.

[4] Gaylard, M.J., Bietenholz, M.F., Combrinck, L., Booth, R.S., Buchner, S.J., Fanaroff, B.L., MacLeod, G.C., Nicolson, G.D., Quick, J.F.H., Stronkhorst, P. and Venkatasubramani, T.L.: An African VLBI Network of radio telescopes. In: *Proceedings of SAIP2011, the 56th Annual Conference of the South African Institute of Physics,Edited by I. Basson and A.E. Botha*, pp. 473–478. 2011.

[5] Joubert, M.: SKA Newsletter. Quarterly newsletter for South Africa's Square Kilometre Array Project, March 2014.

[6] Asabere, B.D., Gaylard, M.J., Horellou, C., Winkler, H. and Jarrett, T.: Radio astronomy in Africa: the case of Ghana. In: Engelbrecht, C. and Karataglidis, S. (eds.), *Proceedings of SAIP2014, the 59th Annual Conference of the South African Institute of Physics ISBN: 978-0-620-65391-6*, pp. 296–301. University of Johannesburg, 2014.

[7] Ludick, J.: Ghana 32 m Antenna Structure Pointing Error Budget. Report Document number:A0210-0000-005, Rev.A, Square Kilometer Array - Africa, AVN Project, 2014 (SKA Internal Document).

[8] Garett, M.: Lecture notes on radio telescopes (2015), ASTRON & Leiden. Available at: `https://www.astron.nl/~mag/dokuwiki/lib/exe/fetch.php?media=radio_astronomy_lec_2_ma_garrett_2015.comp.pdf`, [2 November, 2016], 2015.

[9] TIW: *Ghana Kuntunse 32 m Antenna Assembly Drawing.* TIW SYSTEMS INC., 2460 Embarcadero Way, Palo Alto, CA 94303, rev. 1 edn, 1978.

[10] Gaylard, M.J.: Expanding radio astronomy in africa. *IOP Conference Series: Materials Science and Engineering*, vol. 44, no. 1, p. 012020, 2013. Available at: `http://stacks.iop.org/1757-899X/44/i=1/a=012020`

[11] Schietekat, S.: Kuntunse VLBI Station Conversion Project: User Requirements Specification(URS). Report Document number:A0200-0001-000, Rev.1, Square Kilometer Array - Africa, 2014 (SKA Internal Document).

[12] Ruze, J.: Antenna tolerance theory, no.8212;a review. *Proceedings of the IEEE*, vol. 54, no. 4, pp. 633–640, April 1966. ISSN 0018-9219.

[13] Kraus, J. and Marhefka, R.: *Antennas for all applications*. McGraw-Hill series in electrical engineering. McGraw-Hill, 2002. ISBN 9780072321036.

[14] de Witt, A., Gaylard, M., Quick, J. and Combrinck, L.: An Overview of Geodetic and Astrometric VLBI at the Hartebeesthoek Radio Astronomy Observatory. In: *Proceedings of the 21st Meeting of the European VLBI Group for Geodesy and Astronomy, Edited by N. Zubko and M. Poutanen*, pp. 45–48. 2013. ISBN 978-951-711-296-3.

[15] McCulloch, P.M., Ellingsen, S.P., Jauncey, D.L., Carter, S.J.B., Cimo, G., Lovell, J.E.J. and Dodson, R.G.: Cosmic: Microarcsecond resolution with a 30 metre radio telescope. *Submitted to: Astron. J.*, 2004. `astro-ph/0412396`.

[16] Woodburn, L., Natusch, T., Weston, S., Thomasson, P., Godwin, M., Granet, C. and Gulyaev, S.: Conversion of a new zealand 30-metre telecommunications antenna into a radio telescope. *Publications of the Astronomical Society of Australia*, vol. 32, p. e017, may 2015.

[17] Fujisawa, K., Mashiyama, H., Shimoikura, T. and Kawaguchi, N.: The yamaguchi 32-m radio telescope. In: Ikeuchi, S., Hearnshaw, J. and Hanawa, T. (eds.), *8th Asian-Pacific Regional Meeting, Volume II*, pp. 3–4. 2002.

[18] South Africa's MeerKAT Radio Telescope. Technical Fact Sheet, SKA SA, 3rd Floor, The Park, Park Street, Pinelands, 7405, 2016.

[19] Cenacchi, E., Orfei, A., Mack, K.-H. and Maccaferri, G.: *32 m Antenna*. Istituto Nazionale di AstroFisica, Bologna, Italy, version 1 edn, 2006.

[20] Orfei, A., Morsiani, M., Zacchiroli, G., Maccaferri, G., Roda, J. and Fiocchi, F.: The Active Surface System on the Noto Radio Telescope. In: Ros, E., Porcas, R.W., Lobanov, A.P. and Zensus, J.A. (eds.), *Proceedings of the 6th EVN Symposium, Bonn, Germany*, pp. 13–16. June 25th-28th 2002.

[21] Montaguti, S., Vittuari, L., Sarti, P. and Negusini, M.: Medicina and Noto VLBI Radiotelescopes: gravitational deformations evaluated with terrestrial laser scanning. In: Böhm, J., Pany, A. and Schuh, H. (eds.), *Proceedings of the 18th European VLBI for Geodesy and Astrometry Work Meeting, Geowissenschaftliche Mitteilungen, Heft Nr. 79, Schriftreihe der Studienrichtung Vermessung und Geoinformation, Technische Universität Wien*, pp. 4–9. July 2007. ISSN 1811-8380.

[22] Prestage, R.M., Constantikes, K.T., Balser, D.S. and Condon, J.J.: The GBT precision telescope control system. In: *SPIE Astronomical Telescopes and Instrumentation*, pp. 1029–1040. International Society for Optics and Photonics, 2004.

[23] PATRAN: *2016 Reference Manual*. MSC Software Corporation, 4675 MacArthur Court, Suite 900, Newport Beach, CA 92660, 2016.

[24] NASTRAN: *2016 Reference Manual*. MSC Software Corporation, 4675 MacArthur Court, Suite 900, Newport Beach, CA 92660, 2016.

[25] Gawronski, W., Bienkiewicz, B. and Hill, R.: Wind-induced dynamics of a deep space network antenna. *Journal of sound and vibration*, vol. 178, no. 1, pp. 67–77, 1994.

[26] Gawronski, W.: Wind gust models derived from field data. *Telecommunications and Data Acquisition Progress Report*, vol. 123, pp. 30–36, 1995.

[27] Fox, N.L.: Load Distribution on the Surface of Paraboloidal Reflector Antennas. Report CP-4, NASA JPL, 1962 (JPL Internal Document).

[28] Kron, M.: Load distribution on the surface of paraboloidal reflector antennas. *moment*, vol. 10, p. 2, 1971.

[29] Levy, R. and Kurtz, D.W.: Compilation of Wind Tunnel Coefficients for Parabolic Reflectors. Technical Report JPL-PUB-78-16, Jet Propulsion Lab., California Inst. of Tech.; Pasadena, CA, United States, April 1978.

[30] Mutzberg, U.: Technical Note on Structural Analyses - MeerKAT Dual Offset Antenna. Report TN-1012033-21300-01-01, R3.0, Square Kilometer Array South Africa/Vertex Antennentechnik GmbH, 2014.

[31] Genberg, V.L.: Optical surface evaluation. In: Cohen, L.M. (ed.), *Proceedings of the SPIE Symposium on Structural Mechanics of Optical Systems*, vol. 0450, pp. 81–87. 1984.

[32] Joubert, N.J.D.: *Numerical design optimisation for the Karoo Array Telescope*. MEng, Mechanical Engineering, University of Stellenbosch, Stellenbosch, South Africa, 2009.

[33] Baars, J.W.M., Lucas, R., Mangum, J.G. and Lopez-Perez, J.A.: Near-Field Radio Holography of Large Reflector Antennas. *IEEE Trans. Anten. Propag.*, 2007. [IEEE Anten. Propag. Mag.49,24(2007)], 0710.4244.

[34] Hunter, T.R., Schwab, F.R., White, S.D., Ford, J.M., Ghigo, F.D., Maddalena, R.J., Mason, B.S., Nelson, J.D., Prestage, R.M., Ray, J., Ries, P., Simon, R., Srikanth, S. and Whiteis, P.: Holographic Measurement and Improvement of the Green Bank Telescope Surface. *Publications of the Astronomical Society of Pacific*, vol. 123, pp. 1087–1099, September 2011. 1107.2081.

[35] Sarti, P., Vittuari, L. and Abbondanza, C.: Laser scanner and terrestrial surveying applied to gravitational deformation monitoring of large vlbi telescopes' primary reflector. *Journal of Surveying Engineering*, vol. 135, no. 4, pp. 136–148, 2009.

[36] Copley, C.J., Azankpo, S. and Allotey, J.A.: Characterisation of the Primary Reflectors of the AVN. Report Draft, SKA-SA, 2016 (SKA-SA Internal Document).

[37] Altan, M.O., Celikoyan, T.M., Kemper, G. and Toz, G.: Balloon photogrammetry for cultural heritage. 2002.
Available at: `http://www.isprs.org/proceedings/XXXV/congress/comm5/papers/688.pdf`

[38] TIW: On Site Acceptance Testing of the Ghana 32 m Antenna Structure. Report Vol I, TIW Systems Inc, 2460 Embarcadero Way, Palo Alto, CA 94303, 415/856-9300, 1978 (SKA-SA Internal Document).

[39] Usoff, J.M., Clarke, M.T., Liu, C. and Silver, M.J.: Optimizing the husir antenna surface. *Lincoln Laboratory Journal*, vol. 21, no. 1, 2014.

[40] GENESIS: *Genesis Design Manual*. Vanderplaats Research & Development Inc., 1767 South 8th Street, Suite 200, Colorado Springs, C0 80905, version 15.0 edn, January 2016.

[41] Vanderplaats, G.N.: Structural optimization for statics, dynamics and beyond. *Journal of the Brazilian Society of Mechanical Sciences and Engineering*, vol. 28, no. 3, pp. 316–322, 2006.

[42] Gawronski, W., Baher, F. and Gama, E.: Track level compensation look-up table improves antenna pointing precision. vol. 6273, pp. 627316–627316–9. 2006.

[43] Gawronski, W.: *Modeling and control of antennas and telescopes*. Mechanical engineering series. Springer, Boston, MA, 2008.